UNIVERSITÀ DEGLI STUDI DI BOLOGNA

FACOLTÀ DI SCIENZE MATEMATICHE FISICHE E NATURALI
DOTTORATO DI RICERCA IN FISICA, XIX CICLO
SETTORE SCIENTIFICO FIS/04

PhD Thesis

Assembly and space qualification of the scintillator detector LTOF for the AMS-02 spectrometer

LUCIO QUADRANI

Advisor:	PhD Coordinator:
Chiar.mo Prof.	Chiar.mo Prof.
FEDERICO PALMONARI	**FABIO ORTOLANI**

Bologna, Italy, Mar 15, 2007

UNIVERSITÀ DEGLI STUDI DI BOLOGNA

FACOLTÀ DI SCIENZE MATEMATICHE FISICHE E NATURALI
DOTTORATO DI RICERCA IN FISICA, XIX CICLO
SETTORE SCIENTIFICO FIS/04

PhD Thesis

Assembly and space qualification of the scintillator detector LTOF for the AMS-02 spectrometer

LUCIO QUADRANI

Advisor:
Chiar.mo Prof.
FEDERICO PALMONARI

PhD Coordinator:
Chiar.mo Prof.
FABIO ORTOLANI

Key words: Cosmic rays, Scintillation counters, Thermal Vacuum test, Vibration test, Silicon PhotoMultipliers

Bologna, Italy, Mar 15, 2007

Contents

Introduction

The Alpha Magnetic Spectrometer (AMS-02) is a high energy particle detector devoloped by an international collaboration with the purpose to measure the cosmic ray fluxes outside the Earth atmosphere. It will operate on the International Space Station (ISS) for at least three years. The goals of AMS-02 are the antimatter and dark matter search, and the precise measurement of primary cosmic ray fluxes with energy up to 1 TeV.

The INFN and the University of Bologna have developed the Time Of Flight (TOF) system of the AMS-02 experiment. The TOF is composed by 4 layers of plastic scintillator counters, two above (UTOF) and two below (LTOF) the superconducting magnet. It is an important detector with the following tasks: it gives the fast trigger to the experiment; it measures the time of flight of the cosmic rays in order to obtain the velocity β and to distinguish between upward and downward going particles; it measures the energy loss in order to provide a cosmic ray charge measurement.

This thesis presents the results of my PhD studies. During the first two years I collaborated with the Bologna TOF group to characterize and to test all the counters of the Lower TOF. During the last year, I coordinated the assembly of the Lower TOF and attended the space qualification tests required by NASA, performing all the functional tests.

In the first chapter I describe the AMS-02 experiment, with an explanation of all the subdetectors, with their tasks and their performances during the beam tests at CERN.

The second chapter presents the characterization of the Lower TOF scintillation counters, effectuated in the Bologna INFN laboratories. I describe the characteristics measured with the cosmic ray telescope and the vacuum test of all the LTOF counters. In this chapter is explained also the method I used to optimize the PMTs disposition on the TOF counters.

In the third chapter are described all the phases of the Lower TOF assembly:

in the first part I explain the counter assembly and in the second part the assembly and preparation of the flight model of the Lower TOF.

The fourth chapter describes the space qualification tests executed on the Lower TOF and required by NASA to assure the safety conditions for payloads using the Space Shuttle and the International Space Station. I describe the Thermal Vacuum Test performed in order to verify the performance of the detector in the extreme conditions in which it will operate on the ISS and the Vibration Test executed in order to verify that the detector performances are not degraded by the Maximum Expected Flight level vibration environment.

Because in the last two years I become a member of the DASiPM (Development and Application of Silicon Photomultipliers) project, which study the use of the SiPM photodetector for Medical and Space applications I added a Fifth chapter. In this chapter I present the study of the silicon photomultiplier, a new photodetector which could be a substitute for the usual photomultiplier for space experiment. In particular I explain the characterization of the detector and the MonteCarlo simulation software that I developed in order to understand the response of the SiPM at various light intensities.

Chapter 1

The AMS-02 experiment

The Alpha Magnetic Spectrometer (AMS) is an experiment designed to measure with high accuracy the composition of cosmic rays near Earth, and it will operate for a minimum of three years on the International Space Station. The main scientific goals of the AMS experiment are: the antimatter search as required by the Big Bang theory[1], the dark matter search as predicted by the SUSY theories[2][3] and the study of the primary cosmic ray spectrum, with high statistics ($\sim 10^9$ nuclei and isotopes) and energy up to 1 TeV.

The main components of the AMS-02 detector are (see fig. 1.1):

- Superconducting Magnet, which provides a bending power of $BL^2 = 0.86Tm^2$;
- Time Of Flight (TOF), which measures the cosmic rays time of flight also giving the fast trigger to the experiment.
- Anti Coincidence Counters (ACC), which ensures that only particles passing through the magnet aperture will be accepted;
- Silicon Tracker, which provides a proton rigidity resolution of 20% at 500 GeV and a good charge resolution of nuclei up to Z = 26;
- Transition Radiation Detector (TRD), which identifies electrons and positrons from hadron with 10^{-2} to 10^{-3} accuracy in the energy range between 1 GeV to 300 GeV;
- Ring Imaging Cherenkov (RICH), which measures the velocity and charge $|Z|$ of the particles and nuclei;

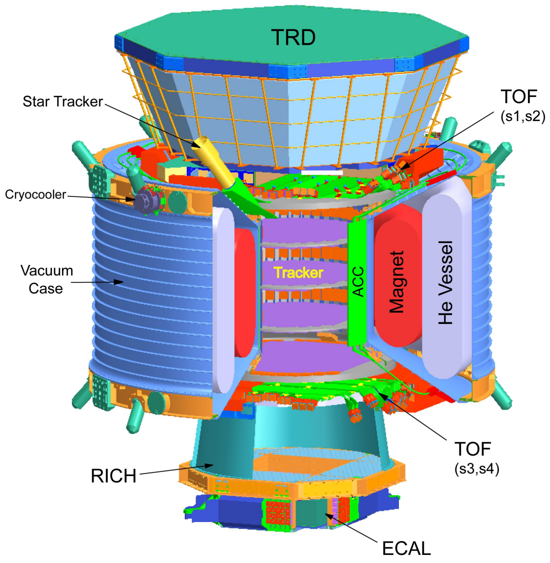

Figure 1.1: The AMS-02 detector.

- Electromagnetic Calorimeter (ECAL), which measures the energy of gamma rays, electrons and positrons and distinguishes electrons and positrons from hadrons, in the energy range between 1.5 GeV to 1 TeV;

In addition, a system of two start trackers (AMICA), allows the precise reconstruction of the origin of high energy gamma rays detected in the ECAL.

To ensure that the AMS detector could withstand the mechanical stress of the launch, the temperature changes and the intense radiation background, a prototype (AMS-01) performed in June 1998 an engineering flight on the Space Shuttle[4].

1.1 The Superconducting Magnet

In order to extend the energy range of the particles and nuclei measurements to the multi-TeV region, AMS-02 has provided of a superconducting magnet[5].

As shown in fig. 1.2, the magnet system consists of superconducting coils, a superfluid helium vessel and a cryogenic system, all enclosed in a vacuum tank. The magnet operates at a temperature of 1.8 K, cooled by 2500 litres of superfluid

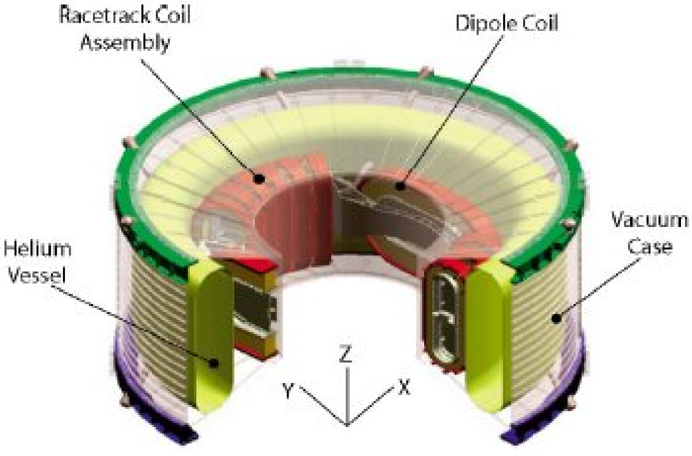

Figure 1.2: The AMS-02 superconducting magnet layout.

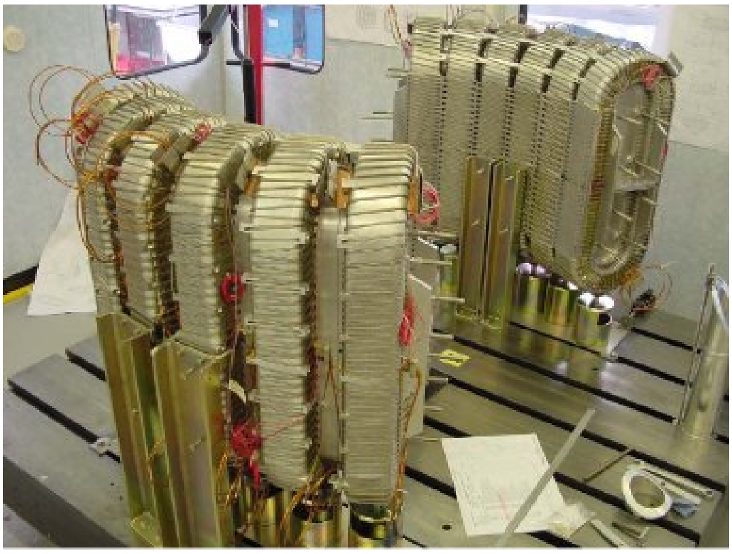

Figure 1.3: Magnet coils assembly.

helium, stored in the vessel. The coil system consists of a set of 14 superconducting coils arranged, as shown in fig. 1.3, around the inner cylinder of the vacuum tank. The single pair of coils generates the magnetic field perpendicular to the experiment axis, and the flux density of the B field at the center of the system is 0.86 T. The current is carried by tiny filaments of niobium titanium (NbTi) which carries the current without resistance (superconducting regime) providing the temperature is kept below 4.0 K.

During the lifetime of the experiment, the helium will gradually boil away and, as it will be used up, the magnet will warm up and will be no longer operable. To increase the duration of the experiment, the He vapours are extracted from the vessel by a special zero-gravity passive phase separator[6] and reused to refrigerate the thermal shield. This allows to achieve a design operating time of 3 to 5 years for the magnet system.

The magnet will be launched at the operating temperature, with the vessel full of superfluid helium, but with no current in the coils. It will be charged only after the installation of the experiment on the International Space Station.

1.2 The Time Of Flight (TOF)

The Time Of Flight system[7] consists of four plastic scintillator planes (two above and two below the magnet), with 8, 8, 10, 8 counters, as shown in figure 1.4. The counters of adjacent planes are orthogonal in order to provide a certain granularity at the trigger level, and in each plane they are overlapped by 5 mm. However, the outermost counters have a trapezoidal shape in order to reduce the weight.

All the 1 cm thick scintillators are read at both ends by photomultiplier tubes, connected with transparent light guides. Due to the strong residual magnetic field in the PMTs regions, the counters adopt the Hamamatsu R5946 phototubes, and have curved light guides. The total number of PMTs is 144 and the optical contact with the light guides has been realized using soft transparent pads, that also provide the mechanical coupling.

The TOF system has the following essential tasks: first, its signals are used to form the fast trigger; second, the particles time of flight is used to measure the velocity $\beta = v/c$ and to distinguish between upward and downward going particles, which is fundamental in order to separate particles from antiparticles. Third, the energy loss measurement is used by the TOF system to send to the

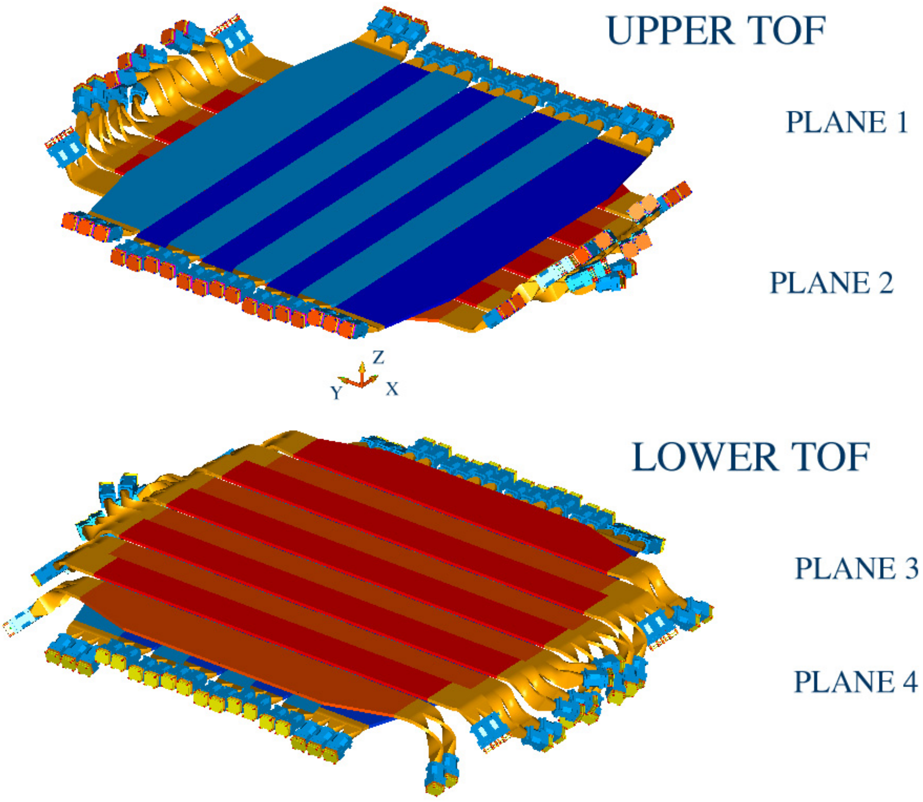

Figure 1.4: The AMS-02 Time Of Flight layout.

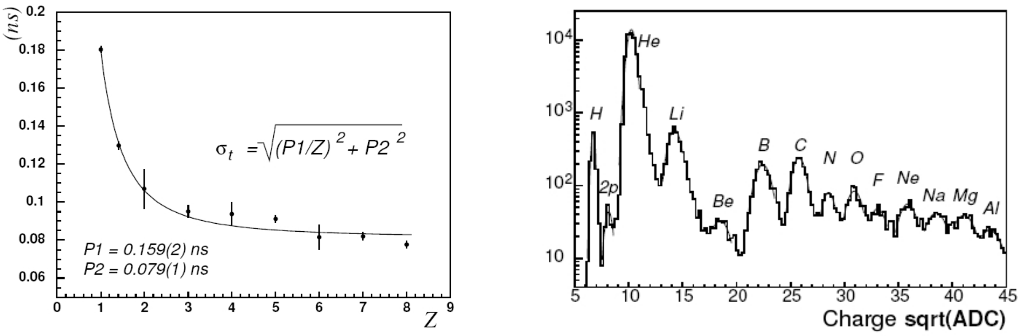

Figure 1.5: Time of flight resolution during the CERN beam test (left). Charge peaks observed with the scintillator counters (right).

trigger box a special flag for ions events, and to provide an indipendent particle charge measurement.

Prototypes of TOF polyvinyltoluene scintillator counters were tested at CERN in 2002 and 2003 at SPS ion beam facility[8]. Runs with A/Z = 1, 2, 9/4, 7/3 were used to get large statistic of all important cosmic rays species. During the 2003 test, 4 TOF counters were equipped with different light guides, 3 with scintillators type Eljen EJ-200 (used for the AMS-02 TOF) and 1 with type Bicron BC-408 (used in AMS-01). The time of flight between different counters was measured: the resolution obtained, in the worst case, for counters with curved and twisted light guides, is shown in figure 1.5 (left), and it is 180 ps for protons and about 100 ps for light ions. The charge of a particle crossing the counter can be measured from its energy loss into the scintillator. In figure 1.5 (right) are shown the charge peaks observed.

1.3 The Anticoincicence Counters (ACC)

The Anticoincidence Counters[9] consists of 16 plastic scintillation paddles (BICRON BC414) that forms a barrel around the tracker of AMS-02. Its purpose is to flag events produced by particles crossing the detector from the side, by δ rays or showers produced by triggered particles, and by back scattering of the electromagnetic calorimeter. The ACC signals are included as veto into the AMS trigger logic.

The ACC paddles have height of 83.2 cm, 220 mm wide and 8 mm thickness,

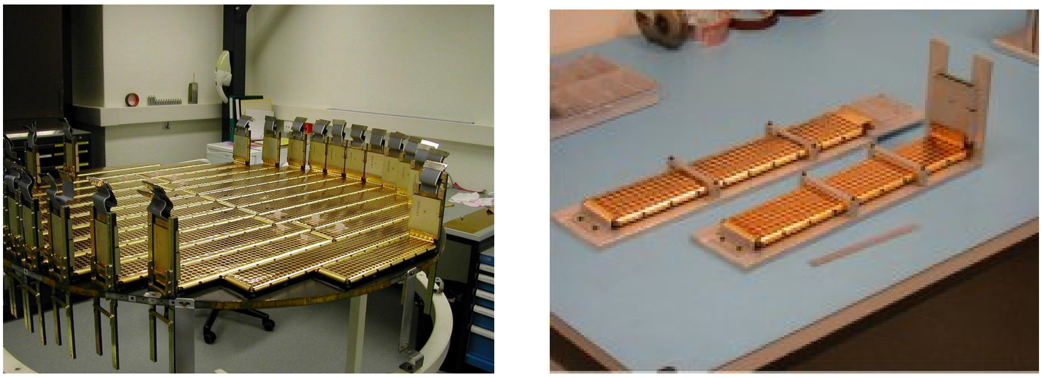

Figure 1.6: One of the inner plane of the AMS Silicon Tracker (left) and the silicon ladders (right).

and form a cylinder with an inner diameter of 109.1 cm. The signal produced by the scintillators are read by 16 PMTs at both ends. Since the ACC will be located inside the magnetic field, the readout PMTs can not be placed in direct contact with the paddles: a wavelength-shifting fibers system is used to route the signals out of the tracking volume, where the PMTs are oriented along the residual stray field lines.

The performance of the ACC system as been tested under a 10 GeV proton beam at CERN in 2003, showing no inefficiencies in a sample of 350,000 events.

1.4 The Silicon Tracker

The Silicon Tracker[10] of AMS is in the center of the detector, inside the superconducting magnet. It is build out of 2264 double-silicon microstrips sensors, with a total surface of $6.7m^2$. The sensors are combined into 192 ladders (fig. 1.6 right) organized in eight layers of $\sim 1m^2$. The three inner planes (fig. 1.6 left) have silicon ladders on both sides, the outher planes only on one side.

The tracker layers are made out of high resistivity n-doped silicon wafers covered with longitudinal heavily p^+-doped silicon strips on one side and with n^+ strips orthogonal to the p^+ strips on the other side. The p^+ implantation strips have pitch of 27.5 μm with a read out pitch of 110 μm. These strips run parallel to the ladder length and will be used to measure the bending coordinate corresponding the y axis in the AMS reference frame. The n^+ implantation strips have a pitch of 104 μm with a 208 μm pitch for the read out. These strips measure the

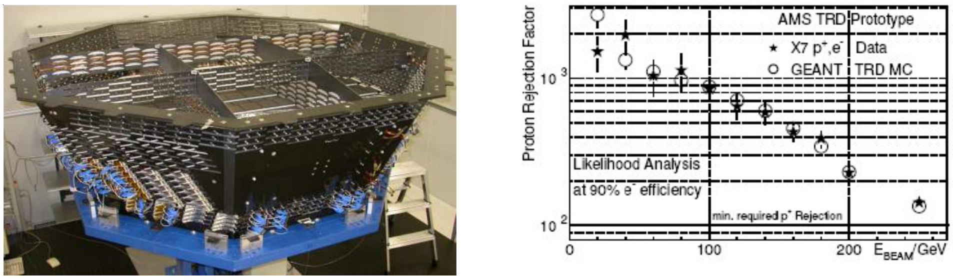

Figure 1.7: The Transition Radiation Detector (left) and the proton rejection factor during the CERN beam test (right).

x coordinate.

Temperature variations along the orbit can reflect on the intrinsic noise of the sensors, changing the efficiency in the minimum ionising particle signal detection. Moreover, since the Tracker is embedded in the magnet system, a thermal control is needed to exaust the heat produced by the read out electronics of the detector. An active cooling system (with CO_2 liquid at about 80 bar pressure), based on a two-phase mechanically pumped loop is beeing developed.

To evaluate the performance of the AMS tracker, 6 flight laders have been exposed to proton and ions beam in the T9 PS experimental hall at CERN[11]. The ions have been magnetically selected to obtain A/Z=2 and A/Z=2.25. The average momentum per nucleon was $\sim$ 10 Gev/n.

The analysis of this test data shown that a single point resolution better than 5(20) μm can be obtained in the measurement of the bending(not bending) coordinate for He ions, and better then 12(24) μm for a wide range of the particles charge. The combined charge measurement of the six ladders under beam test has shown a charge discrimination capability up to Z=24. In the full AMS-02 tracker, where a combined measurement from eight ladders will be available, ion identification up to Fe will be reached.

1.5 The Transition Radiation Detector (TRD)

Transition Radiation consists of soft X rays and it is emitted when charged particles traverse the boundary between two materials with different dielectric constants. Since the emission of this radiation has a threshold of $\gamma \approx 500$ (Lorentz factor), light particles have a higher probability of emitting X rays than the heavy ones. This allows a discrimination between positrons and protons.

The AMS Transition Radiation Detector[12] (see fig. 1.7 left) is on top of the magnet vacuum case and it consists of 20 layers of fiber fleece material (radiator) and straw modules filled with high Z gas mixture. The constituent modules (328 in total) are supported by a conical octagonal structure of aluminuim honeycomb with carbon fiber walls.

The AMS TRD will provide a proton rejection greater then 10^2 in the energy range between 1 and 300 GeV, and above 1000 for energy below 100 GeV. The latter energy range is the one of interest for indirect dark matter detection. In conjunction with the electromagnetic calorimeter (ECAL) it will allow to distinguish positrons over protons with a rejection factor greater then 10^6 at 90% of efficiency.

A full 20 layer prototype equipped with 40 modules was tested at the CERN X7 beam line and in fig. 1.7 (right) it is shown the proton rejection factor for the energy range from 15 GeV to 250 GeV, in comparison with the Monte Carlo simulation.

1.6 The Ring Imaging Cherenkov (RICH)

The AMS RICH detector[13] (see fig. 1.8) has a truncated conical shape and it covers 80% of the AMS magnet acceptance. It is a proximity focusing device with a dual solid radiator configuration on the top, an expansion height of 46.9 cm and, at the bottom, a matrix of 680 multipixeled photon readout cells. A high reflectivity mirror with a conical shape surrounds the whole set in order to increase the device acceptance. The radiator is made of 80 Aerogel 27 mm thick tiles with a refractive index 1.05, and sodium fluoride (NaF) tiles with a thickness of 5 mm in the center, covering an area of 34 x 34 cm^2. The NaF placement prevents the loss of photons in the hole existing at the center of the readout plane.

To prevent a large fraction of RICH radiated photons ($\sim 33\%$) to escape through the lateral surface of the expansion volume, a conical reflector was designed. It consists of a carbon fiber reinforced composite substrate with a multilayer coating made of alluminium and SiO_2 deposited on the inner surface. This ensures a reflectivity higher than 85% for 420 nm wavelength photons.

The photon detection is made with an array of multianode photomultipliers Hamamatsu R7600-00-M16 with a spectral response maximum at $\lambda \sim 420$ nm. The strength of the residual magnetic field imposes the need to shield the PMTs with Permalloy. To increase the photon collection efficiency, a light guide con-

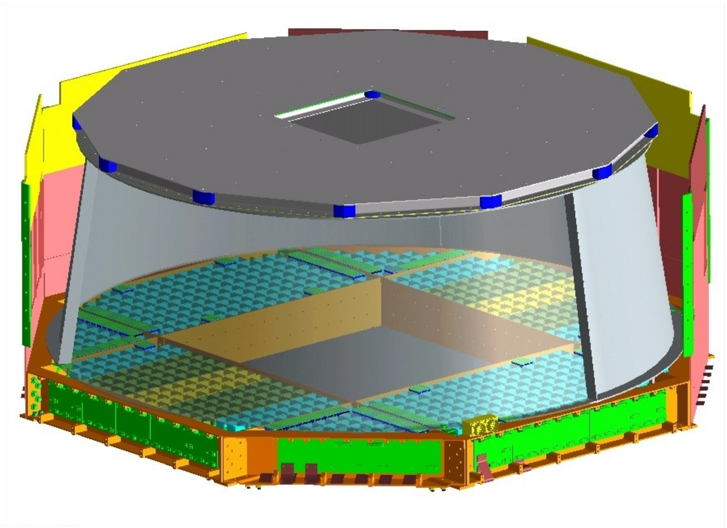

Figure 1.8: The AMS-02 RICH layout.

sisting of 16 solid acrylic pipes glued to a thin top layer was produced. This light guide is mechanically attached through nylon wires to the photomultiplier polycorbinate housing.

A prototype of the RICH detector consisting of an array of 9 x 11 cells filled with 96 photomultiplier readout units was tested with cosmic muons and fragmented ions from CERN SPS beams in 2002 and 2003[14]. The evaluation of the aerogel samples in order to make a final radiator choice was one of the key issues of these tests. The required criteria for a good candidate were a high photon yield, in order to ensure a good ring reconstruction efficiency, and an accurate β and charge measurements.

A charge resolution around 0.15 is observed for low Z ions together with a systematic uncertainty, scaling with the charge, of 1.2% due to non-uniformities. Charge peaks up to iron were indentified as shown in figure 1.9 (left).

The resolution for the β measurement was estimated using a Gaussian fit to the reconstructed β spectrum. The charge dependence of the velocity resolution is shown in figure 1.9 (right). The observed distribution varies like 1/Z as it could be expected from the charge dependence of the photon yield in Cherenkov emission, up to a saturation limit set by the pixel size of the detector.

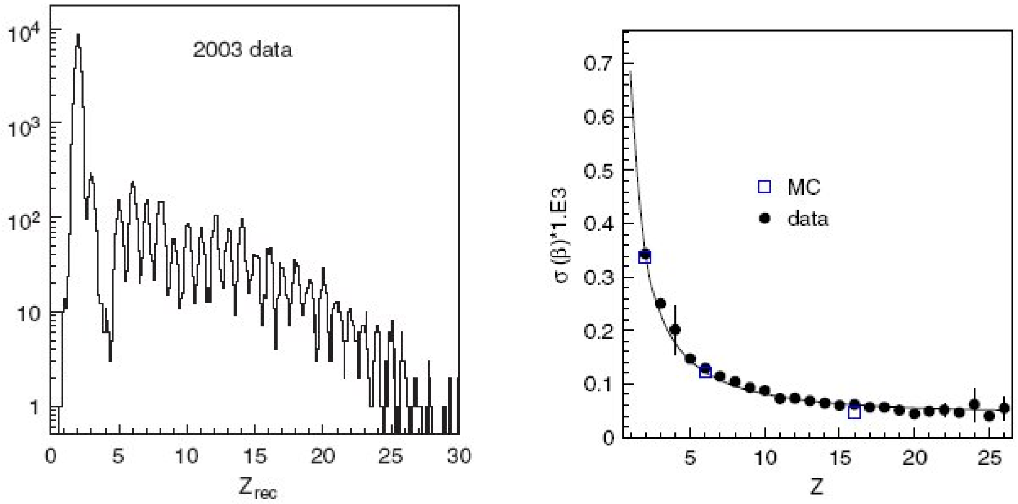

Figure 1.9: RICH SPS beam test results. Reconstructed charge spectrum from the measured data (left). Charge dependence of the velocity resolution obtained from data and Monte Carlo simulation. (right).

1.7 The Electromagnetic Calorimeter (ECAL)

The Electromagnetic Calorimeter of AMS-02 (see fig. 1.10 left) is a fine grained lead-scintillating fiber sampling calorimeter [15][16] that allows precise, 3 dimensional imaging of the longitudinal and lateral shower development, providing high ($> 10^6$) electron/hadron discrimination in combination with the other AMS detectors and good energy resolution. The calorimeter also provides a standalone photon trigger capability to AMS.

The ECAL has an active area of 648 x 648 mm^2 and a thickness of 166.5 mm. It is composed by superlayers, each 18.5 mm thick and made of 11 grooved, 1 mm thick lead foils interleaved with layers of 1 mm diameter scintillating fibers and glued together with epoxy. The detector imaging capability is obtained by stacking superlayers with fibers alternatively parallel to the x-axis (4 layers) and y-axis (5 layers). The calorimeter has a total weight of 496 kg and a thickness corresponding to about 17 radiation lengths.

Fibers are read out, only at one end, by four anode Hamamatsu R7600-00-M4 photomultipliers; each anode covers an active area of 9 x 9 mm^2, corresponding to 35 fibers, defined as a cell. In total the ECAL is subdivided into 1296 cells (324 PMTs) and this allows a sampling of the longitudinal shower profile by 18

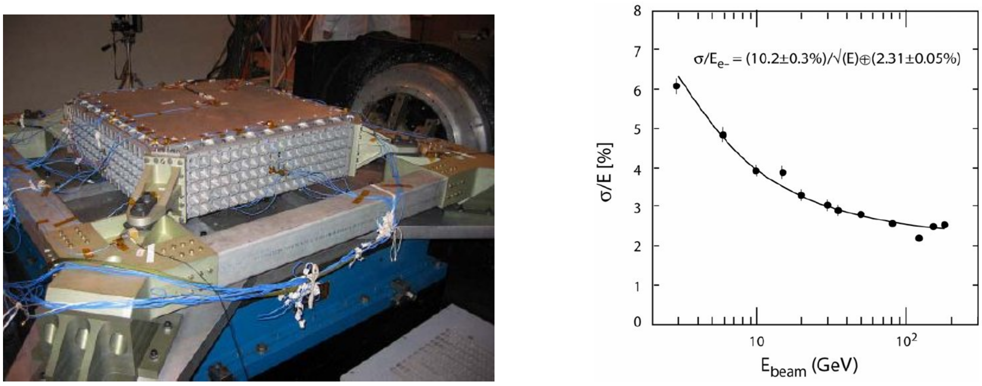

Figure 1.10: The AMS-02 Electromagnetic Calorimeter (left) and its energy resolution (right).

indipendent measurements.

In 2002 the ECAL qualification model was exposed to the CERN SPS beam line H6A with muons, 120 GeV protons and antiprotons and 3 to 180 GeV $e^{\pm}$. From the fits to the ECAL response at different energies good linearity was found up to 40 GeV, while deviations of the order of 5% at 80 GeV and 13% at 180 GeV were observed. A leakage correction, based on the energy deposit in the last ECAL superlayer, was applied in order to estimate the total energy. The calorimeter energy resolution is shown in figure 1.10 (right): this result was obtained for electrons entering the ECAL at the center of the equipped region and it is in good agreement with the Monte Carlo simulation. The ECAL discrimination power is about 1/250 with an efficiency of 90%.

Chapter 2

Characterization of the TOF scintillation counters

The Time of Flight of the AMS experiment is composed by 4 layers of scintillation counters, two above (UTOF) and two below (LTOF) the superconducting magnet. The Lower TOF is made up of 10 counters (plane 3) and 8 counters (plane 4), while the Upper TOF is made up of 8 counters for both planes 1 and 2. The counters of adjacent planes are orthogonal in order to provide a certain granularity at the trigger level and in each plane they are overlapped by 0.5 cm to avoid geometrical inefficiencies. The outermost counters have trapezoidal shape in order to reduce the weight of the detector. The geometrical acceptance has been fixed at 0.4 m^2sr to maximize the sensitivity of the spectrometer for antimatter search. The high absolute value of the magnetic field $(1.5 \div 2kG)$ forced the adoption of the fine mesh photomultipliers. Even though this type of PMTs can operate inside magnetic field, their response depends strongly on the angle between the field and the PMT longitudinal axis. Thus tilted light guides where designed in order to minimize this angle for each photomultiplier. All the counters of the Lower TOF were characterized with the cosmic ray telescope and tested in vacuum with the space simulator of the Bologna laboratories.

2.1 The cosmic ray telescope

The cosmic ray telescope of the Bologna laboratory (see fig. 2.1) is composed by a reference scintillation counter, two layers of Limited Streamer Tubes (LST) [17], a black box were the TOF counters are inserted for the charachterization, the

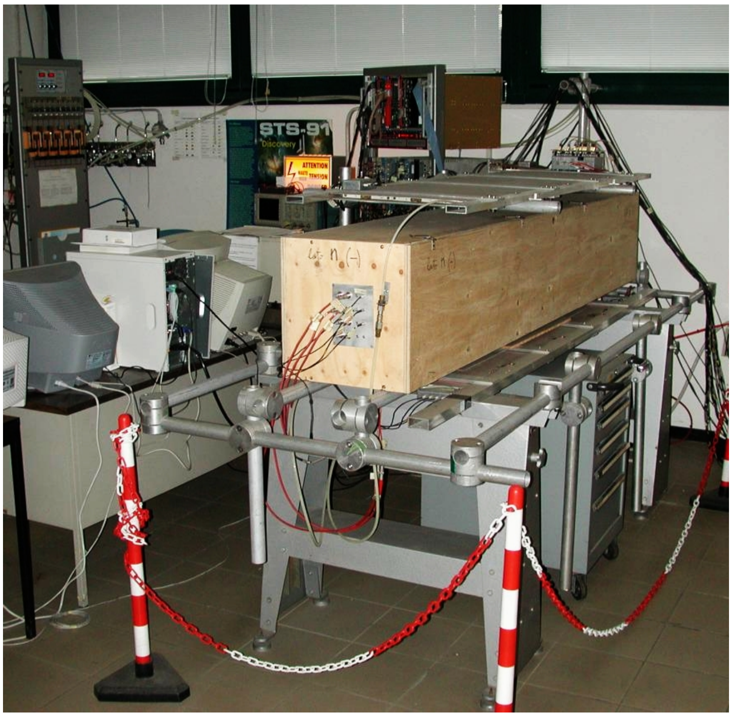

Figure 2.1: The cosmic ray telescope used for the AMS counters characterization. In the picture are shown the black wooden box, the two layers of LST above and below the box, electronics and computers for DAQ and analysis. The reference scintillation counter is under the lower LST layer.

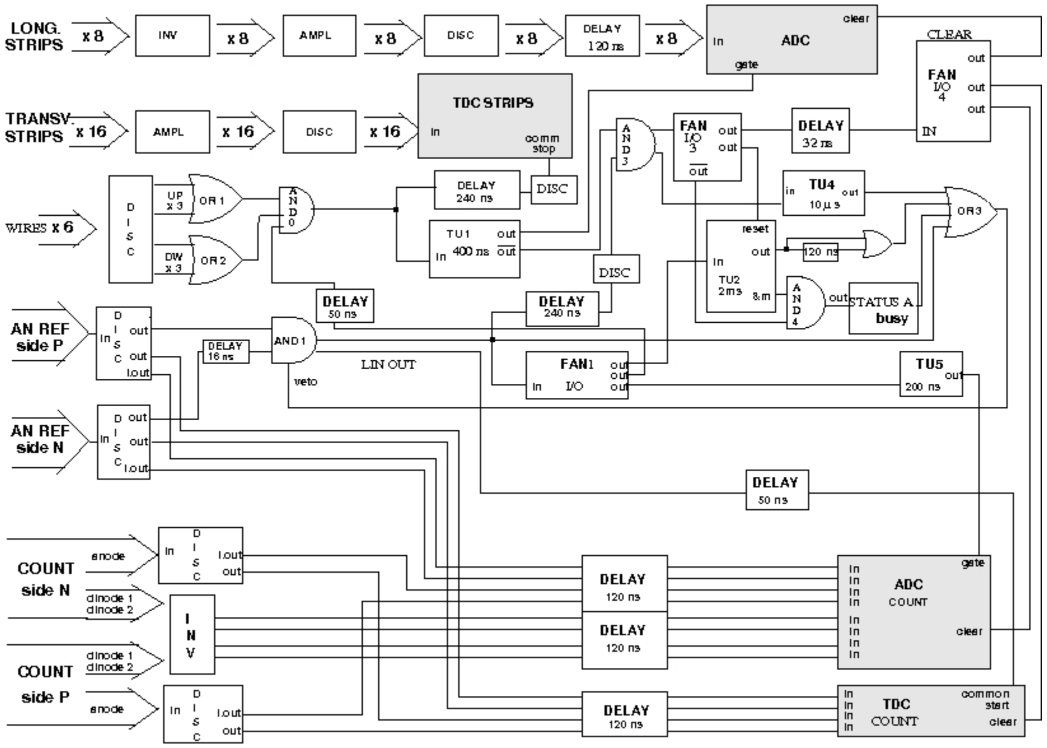

Figure 2.2: The DAQ system of the cosmic ray telescope.

front end electronics (NIM, CAMAC and VME modules) and a data acquisition system. The reference counter is made up of Bicron BC-404 plastic scintillator with rectangular shape (140 cm x 10 cm x 1 cm), straight light guides and 4 fine mesh Hamamatsu R5946 PMTs. It is used to give the fast trigger to the DAQ system and to measure the time of flight resolution with the TOF counter under test. The two LST layers are below and above the black box, at a distance of 55 cm from each other. Each layer has 5 tubes (9 cm wide and 140 cm long), filled with a mixture of isobutane (10%), CO_2 (80%) and argon (10%). They are covered by strips that allow to measure the position of the cosmic rays passing through the telescope: 72 transversal strips, arranged orthogonally to the tubes length, for the X coordinate (with 1.5 cm resolution) and 4 longitudinal strips, arranged along the tubes length, for the Y coordinate.

The reference counter is under the lower LST layer: the coincidence of the anode signals from both sides (P and N) of the counter gives the first level trigger

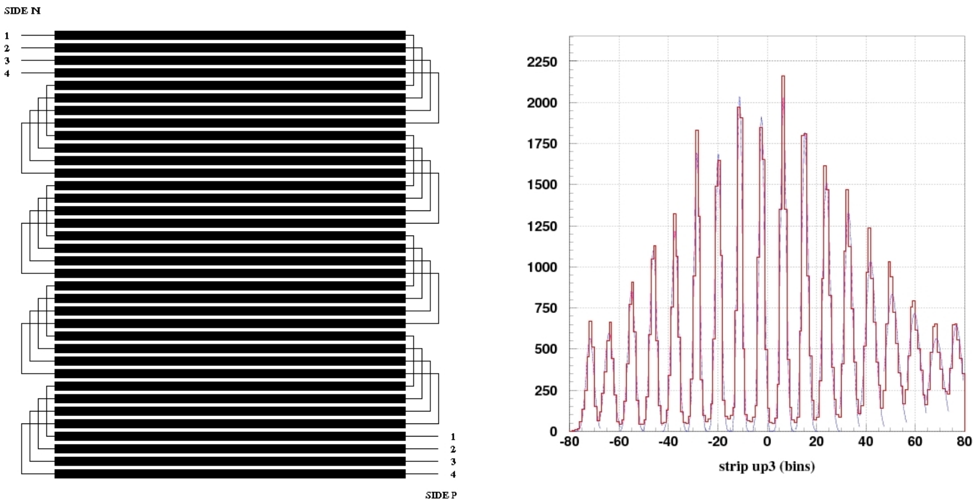

Figure 2.3: The strips of the two LST layers are linked in four chains and allow to reconstruct the trace of the cosmic ray passing thorugh the telescope (left). The time difference between the signals from the two sides of a chain gives 18 peaks, each one corresponding to a strip of the chain (right).

(fast trigger) to the data acquisition (see fig. 2.2). The wires of the two LST layers provide the second level trigger: if a cosmic ray crosses both the LST layers the acquisition proceed, otherwise the acquisition is blocked and the modules cleared, up to the next fast trigger.

When a cosmic ray crosses the telescope it produces a signal in the strips of the LST layers (up and down). The measure of the time difference of the signals from the two strips sides gives the position of the cosmic ray passing through the LST layers, and with geometrical considerations, its position along the counters.

Each of the two LST layers has 72 transversal strips linked in 4 chains (see fig. 2.3 left). The time difference between the two sides of each chain gives a spectrum like in fig. 2.3 (right). Each one of the 18 peaks corresponds to a strip of the chain hitted by the cosmic ray. The X coordinate on the LST layer is given by the formula[1]:

$$X = [72(N_{strip} - 1) + 18(N_{chain} - 1) - 639]cm \tag{2.1}$$

where N_{strip} is the strip hitted by the cosmic ray and N_{chain} the corresponding

---

[1] The origin of the X coordinate is at the center of the LST layer.

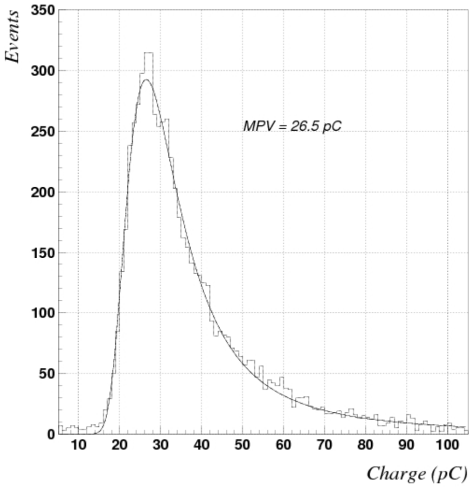

Figure 2.4: The spectrum of the integrated charge of PMT anode signals, selecting a central slice of the counter. The PMT gain is equalized when the Landau peak (MPV) is at 25 pC.

chain.

The Y coordinate is given by the longitudinal strip hitted by the cosmic ray.

The AMS-02 counters are made up of plastic scintillator from Eljen-Technology[2] type EJ-200. The scintillators are equipped with transparent plexiglass light guides to match the PMT chatode. The guides are curved and tilted for the counters of the planes 2 and 3 (to minimize the angle between the magnetic field and the PMT longitudinal axis) and straight for the counters of the planes 1 and 4. All the counters have 2 or 3 PMTs (for redundancy) in each side. The photomultipliers are Hamamatsu[3] fine-mesh type R5946. The sum of the PMT anode signals and the dynode signals are read from each counter.

The gain of each PMT of the TOF counter must to be equalized before the characterization. The PMT anode signals, integrated by the ADC CAMAC module[4], give a charge spectrum with a Landau shape as in figure 2.4. The PMT voltage is adjusted up to obtain a carge peak equal to 25 pC (at the counter center,

---

[2] http://www.eljentechnology.com/

[3] http://www.hamamatsu.com/

[4] ADC LeCroy 2249W.

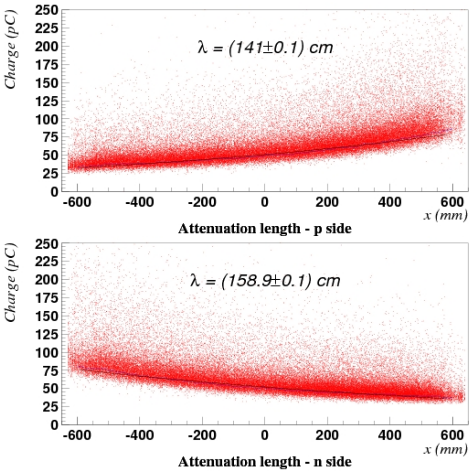

Figure 2.5: Attenuation length measured from both sides of a LTOF counter.

corresponding to X=0).

To characterize the TOF counters, the following measurements are executed:

- *attenuation length*;
- *photostatistics*;
- *light velocity*;
- *intrinsic time resolution*;
- *time of flight resolution*.

I have characterized all the Lower TOF counters. The characteristics of the counters are stored in the AMS-02 TOF database[5] (see fig. 2.13).

2.1.1 Attenuation length

The light intensity I, produced by a cosmic ray inside the scintillator is attenuated according to the law $I = I_0 e^{-x/\lambda}$, where x is the position along the counter and λ

---

[5] http://ams.bo.infn.it/database/.

is the attenuation length of the scintillator. Assuming that the charge of the integrated anode signal is proportional to the light intensity I, it is possible to measure the counter attenuation length. In fig. 2.5 is shown the charge as a function of the X position, from both sides of a counter: the exponential fits give the attenuation length values.

2.1.2 Photostatistics

The measurement of the charge of the PMT anode signals, allows to estimate the number of photoelectrons produced by the cosmic rays into the scintillator. Let N_{phe} be the number of photoelectrons detected by all the PMTs of the scintillation counter, Q the charge measured by the ADC from the anode signals of each side, g the photomultiplier gain and ε its efficiency. Assuming for each PMT that $Q = g\varepsilon N_{phe}$, the gain is equalized and the light guide collection efficiency is the same, then:

$$R = \frac{Q^n - Q^p}{Q^n + Q^p} = \frac{N^n_{phe} - N^p_{phe}}{N^n_{phe} + N^p_{phe}} \tag{2.2}$$

where n and p are the two sides of the counter.
But $N_{phe} = N^n_{phe} + N^p_{phe}$, then:

$$R = \frac{N^n_{phe} - N^p_{phe}}{N_{phe}} = \frac{2N^n_{phe}}{N_{phe}} - 1. \tag{2.3}$$

Supposing that N^n_{phe} follows a binomial distribution, the standard deviation on R is given by:

$$\sigma_R = \frac{2}{N_{phe}}\sqrt{N_{phe}p(1-p)} = \frac{1}{\sqrt{N_{phe}}} \qquad\qquad p = \frac{1}{2}. \tag{2.4}$$

and,

$$N_{phe} = \frac{1}{\sqrt{\sigma^2_R}}. \tag{2.5}$$

Although the above estimation is very approximative, and based on not realistic assumptions, one can show that it is in any case a lower limit on the total number of photoelectrons collected. Furthermore it is a simple criterion applicable to all the counters to get a figure of merit.

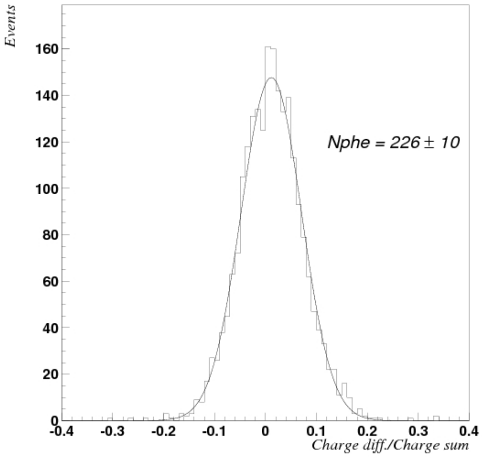

Figure 2.6: The measurement of the charge from the PMT anode signals allows to estimate the number of photoelectron produced by a cosmic ray at the counter center.

In figure 2.6 it is shown a spectrum of the ratio R.

2.1.3 Slewing corrections

All the times measured by the TDC[6] from the anode signals of the counters, have to be corrected by the *slewing* effect. The falling edge of the anode signal is fast, but when it is discriminated, it is delayed depending to the threshold. In fig. 2.7 is shown the slewing effect. It is possible to correct the measured times, taking into account that, empirically, the delay is given by:

$$\Delta T \propto \frac{1}{Log(Q)} \tag{2.6}$$

where Q is the charge measured by the ADC, and T the time measured by the TDC.

---

[6] TDC CAMAC LeCroy 2228A.

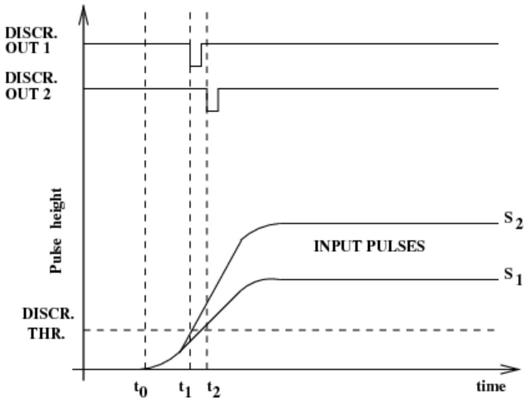

Figure 2.7: The slewing effect: when two pulses of different heights are discriminated, they cross the TDC threshold at different times.

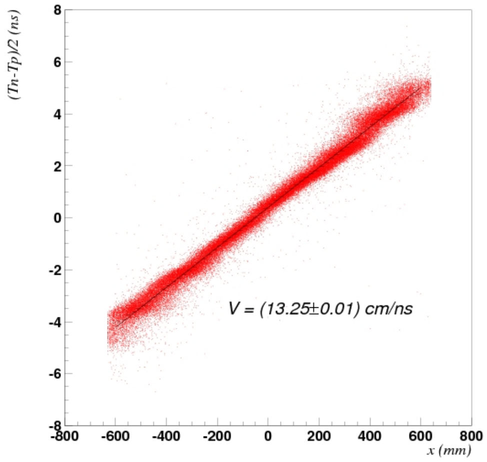

Figure 2.8: Semidifference of the times from both sides of a LTOF counter in function of the position. The light velocity is the inverse of the slope of the linear fit.

2.1.4 Light velocity

The times measured by the TDC (from the anode signals) and the position in which the cosmic ray crosses the counter (reconstructed by the strips signal), allow to measure the effective velocity of the light into the scintillator. It depends both on the refractive index of the scintillator (1.58) and on the mean angle of the collected light with respect to the counter axis. The semidifference of the times (from both sides of the counter) as a function of the position along the counter (see fig. 2.8) can be fitted with a linear function. The inverse of the slope represents the effective velocity of propagation of the light produced by the cosmic ray inside the scintillator. The light velocity V can be found from the relation:

$$T_n = T_0 + (L/2 + x)/v \qquad\qquad T_p = T_0 + (L/2 - x)/v \tag{2.7}$$

and

$$V = \frac{2x}{T_n - T_p} \tag{2.8}$$

where T_n and T_p are the times measured by both sides of the counter (and corrected from the *slewing* effect), T_0 is the common start of the TDC, L is the counter length and x the position along the counter. The mean effective velocity measured for a TOF counter is about $13cm/ns$.

2.1.5 Intrinsic time resolution

One of the goal of the TOF system is the measure of the time of flight of the cosmic rays with high precision. It is important to measure the intrinsic time resolution of each counter. To do this one can measure the resolution of the time difference between the anode signals from both sides of the counter. The times measured by the TDC (see electronic scheme in fig. 2.2) are:

$$T_n = \frac{L/2 + x}{V} + \Delta T + \frac{A_n}{Log(Q_n)} - T_0 \tag{2.9}$$

$$T_p = \frac{L/2 - x}{V} + \Delta T + \frac{A_p}{Log(Q_p)} - T_0 \tag{2.10}$$

where ΔT is the delay introduced by the cables of the setup, $\frac{A_i}{Log(Q_i)}$ is the slewing correction for the times of side i and T_0 is the common start of the TDC.

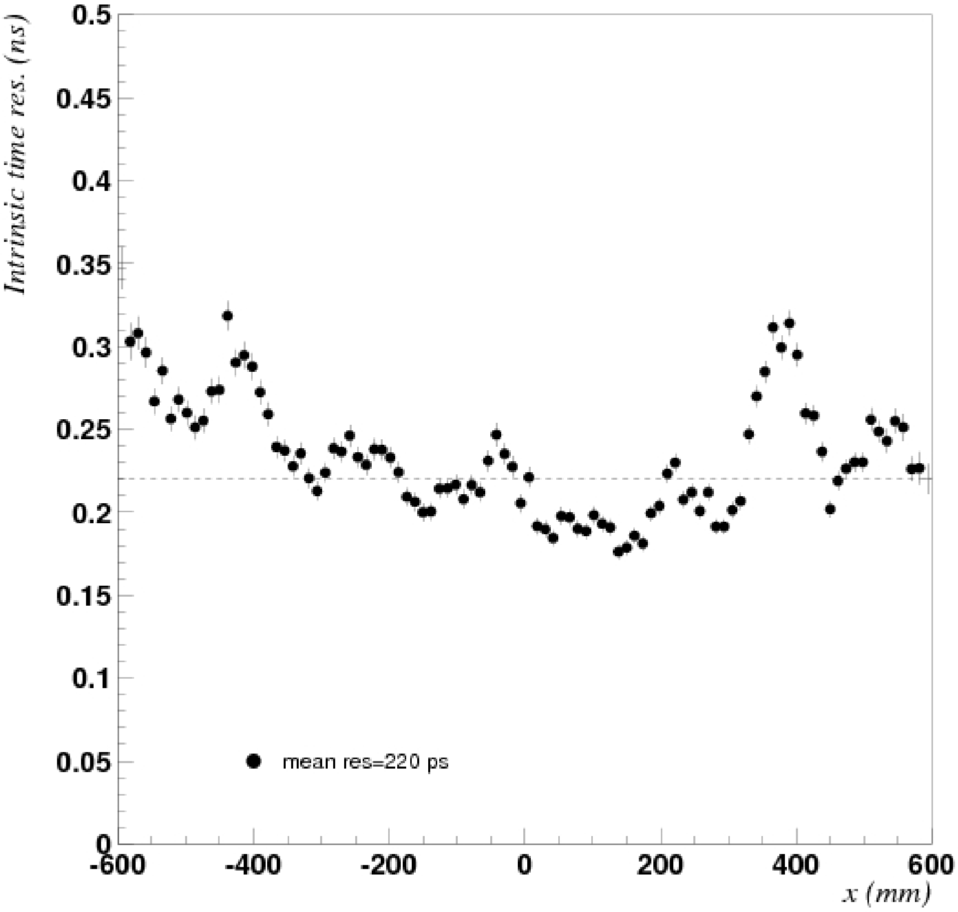

Figure 2.9: Intrinsic time resolution of a LTOF counter as a function of the position. The mean resolution is calculated on the 10 central slices of the counter.

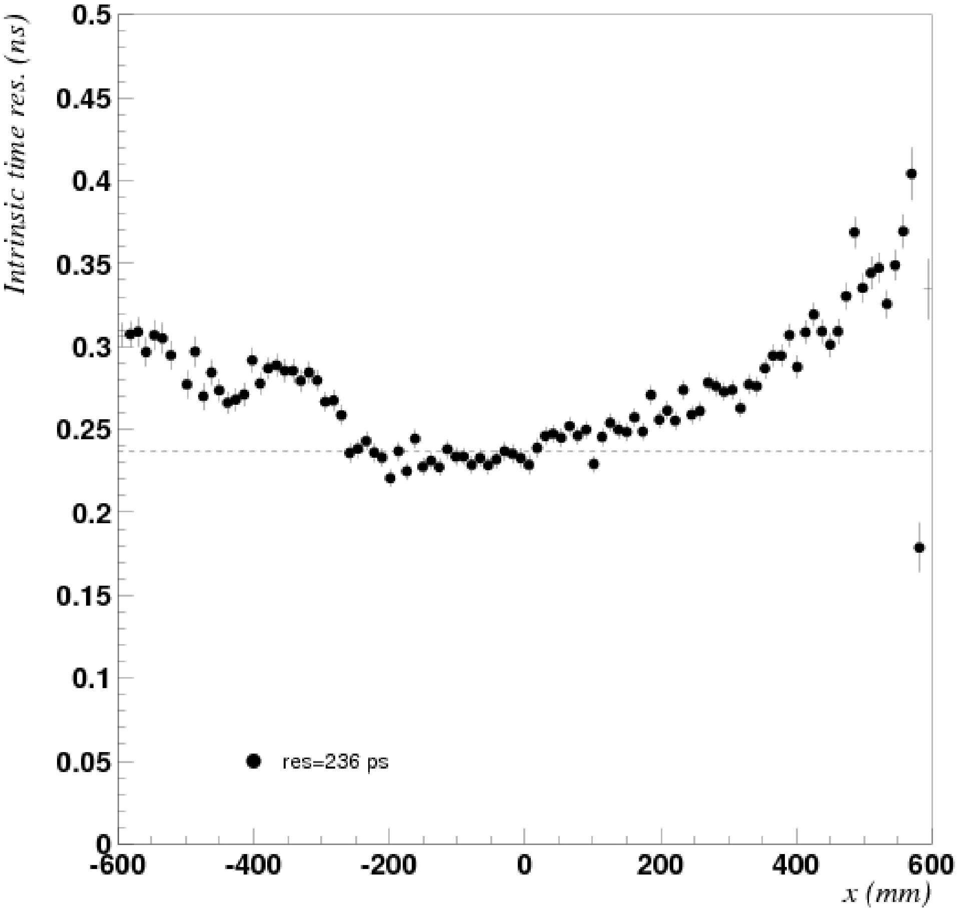

Figure 2.10: Intrinsic time resolution of the reference counter as a function of the position. The mean resolution is calculated on the 10 central slices of the counter.

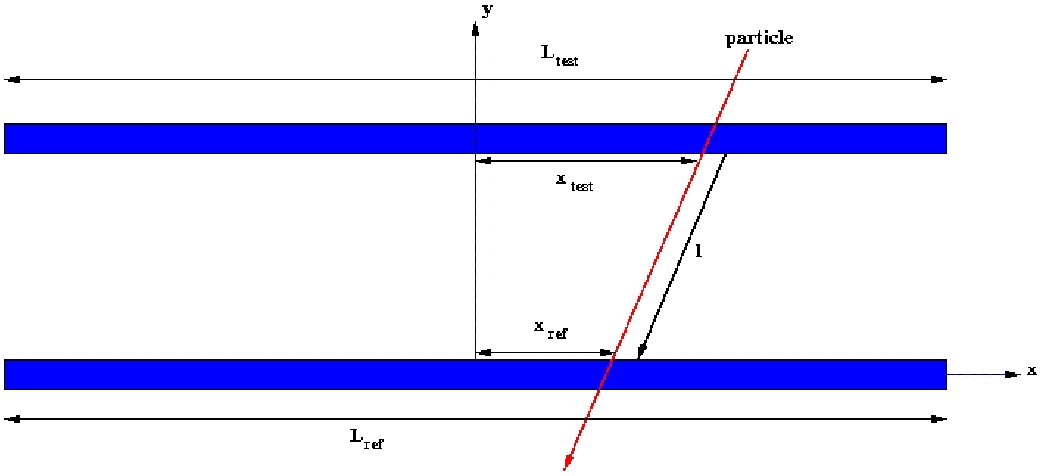

Figure 2.11: Scheme of a particle which crosses the telescope.

The resolution of the time difference can be found by the relation:

$$\frac{T_n - T_p}{2} = \frac{x}{V} + \frac{A_n}{Log(Q_n)} - \frac{A_p}{Log(Q_p)} \tag{2.11}$$

The intrinsic time resolution is measured in slices along the counter. In fig. 2.9 and fig. 2.10 are shown the measured intrinsic time resolutions for a TOF counter and for the reference counter. To characterize each counter, the mean resolution calculated on the 10 central slices is taken.

2.1.6 Time of flight resolution

To measure the time of flight resolution one considers the times measured by the test counter and by the reference counter. A cosmic ray which crosses the telescope (see fig. 2.11) and passes the test counter at the time t_0, will pass the reference counter at the time $t_0 + l/(\beta c)$, and the times measured by the TDC from both counters sides, will be:

$$T_n^{test} = \frac{L^{test}/2 + x^{test}}{V^{test}} + \Delta T + \frac{A_n^{test}}{Log(Q_n^{test})} - T_0 \tag{2.12}$$

$$T_p^{test} = \frac{L^{test}/2 - x^{test}}{V^{test}} + \Delta T + \frac{A_p^{test}}{Log(Q_p^{test})} - T_0 \tag{2.13}$$

$$T_n^{ref} = \frac{l}{\beta c} + \frac{L^{ref}/2 + x^{ref}}{V^{ref}} + \Delta T + \frac{A_n^{ref}}{Log(Q_n^{test})} - T_0 \tag{2.14}$$

$$T_p^{ref} = \frac{l}{\beta c} + \frac{L^{ref}/2 - x^{ref}}{V^{ref}} + \Delta T + \frac{A_p^{ref}}{Log(Q_p^{test})} - T_0 \tag{2.15}$$

The time of flight is given by the difference of the mean times of the two counters (test and reference):

$$\frac{T_n^{test} + T_p^{test}}{2} - \frac{T_n^{ref} + T_p^{ref}}{2} = \frac{1}{2}\Big(\frac{L^{test}}{V^{test}} - \frac{L^{ref}}{V^{ref}}\Big) + \frac{1}{2}\Big(\frac{A_n^{test}}{Log(Q_n^{test})} - \frac{A_p^{test}}{Log(Q_p^{test})}\Big) -$$

$$\frac{1}{2}\Big(\frac{A_n^{ref}}{Log(Q_n^{ref})} - \frac{A_p^{ref}}{Log(Q_p^{ref})}\Big) - \frac{l}{\beta c} \tag{2.16}$$

The resolution on the time of flight is measured on slices along the counter (see fig. 2.12); the mean resolution is calculated on the 10 central slices.

All the characteristics of the AMS TOF counters are stored in the AMS TOF database, that I contribuited to realize. In figure 2.13 it is shown a table with the characteristics of all the Lower TOF counters. We aspect that the time resolution measurements will be improved with the flight electronics.

2.2 The PMT disposition on the TOF counters

The PMTs of the AMS TOF counters should ideally have the same gain, the same equalized responses, the same voltage and similar transit time. Limits on the experiment total weigth and power budget imposed severe constraints on the number of channels of the power supplies, so most of the PMTs will be powered two by two with the same HV channel (see fig. 3.12, chap 3).

It was necessary to optimize the disposition of the 144 PMTs on the TOF, considering that the effect of the magnetic field changes with the position, that the PMTs have to work with a voltage below 2300 V, and that the PMTs are powered in pairs. These forced us to use meta-heuristic algorithms to resolve the problem, in particular it was used a combination of simulated annealing and genetic algorithms[18][19].

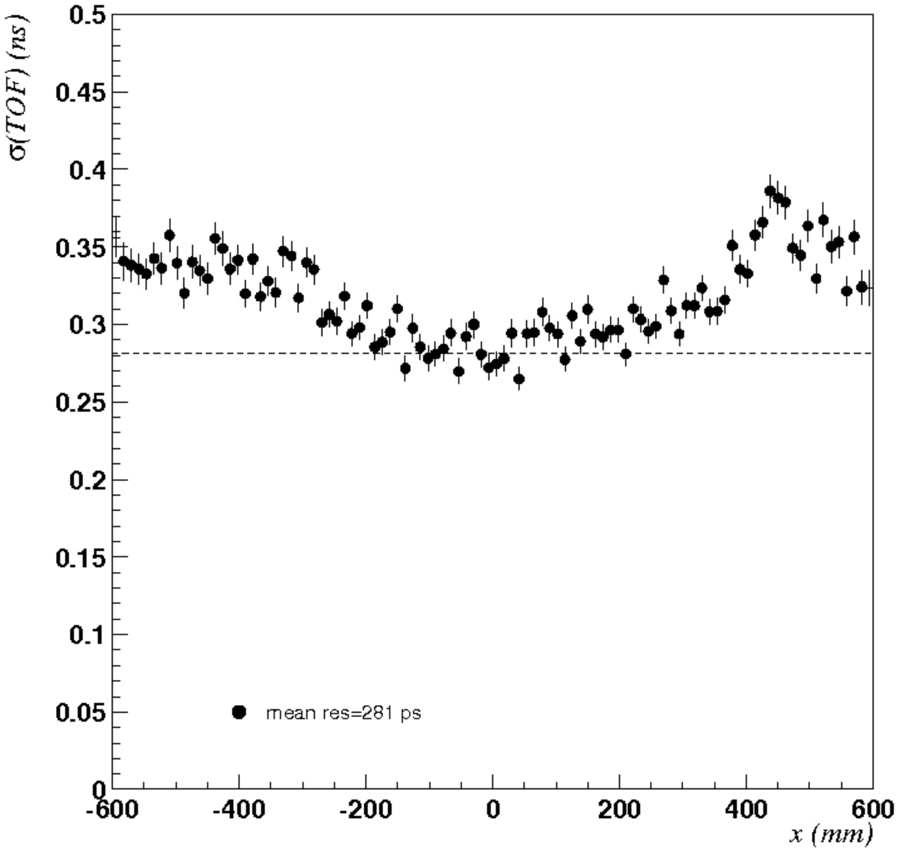

Figure 2.12: Time of flight resolution of a LTOF counter as a function of the position. The mean resolution is calculated on the 10 central slices of the counter.

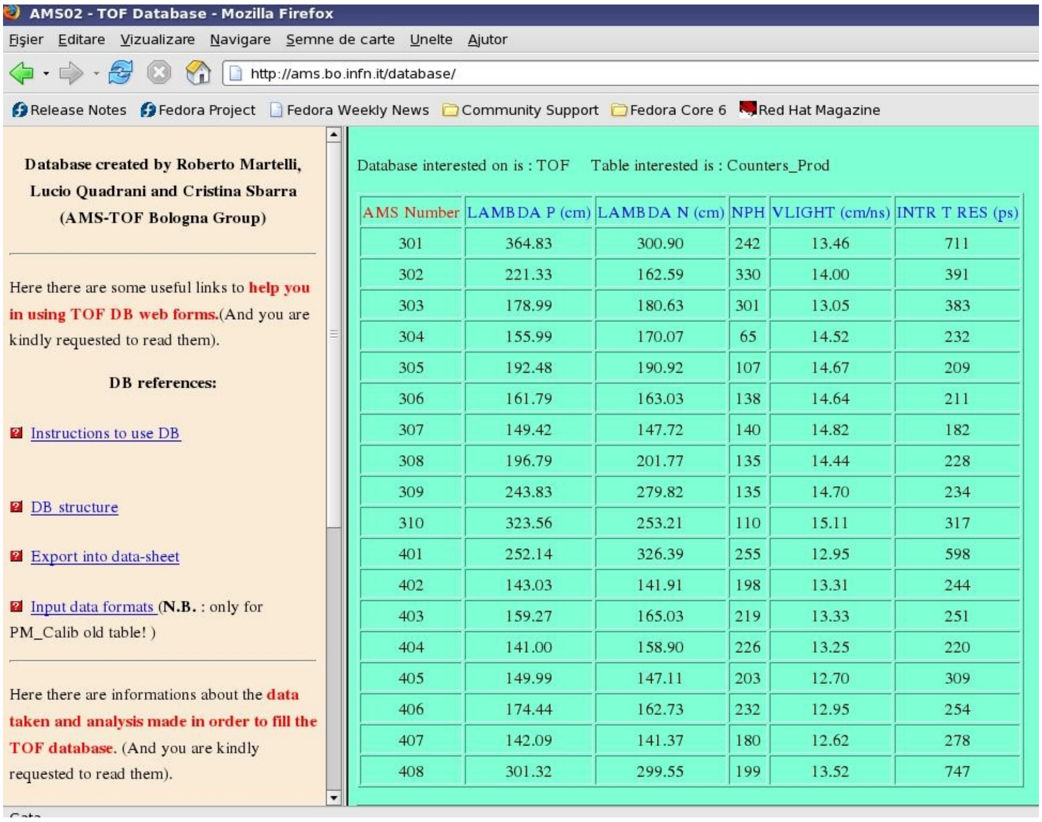

Database created by Roberto Martelli, Lucio Quadrani and Cristina Sbarra (AMS-TOF Bologna Group)

Here there are some useful links to **help you in using TOF DB web forms.**(And you are kindly requested to read them).

DB references:

- Instructions to use DB
- DB structure
- Export into data-sheet
- Input data formats (**N.B.** : only for PM_Calib old table!)

Here there are informations about the **data taken and analysis made in order to fill the TOF database**. (And you are kindly requested to read them).

Database interested on is : TOF   Table interested is : Counters_Prod

AMS Number	LAMBDA P (cm)	LAMBDA N (cm)	NPH	VLIGHT (cm/ns)	INTR T RES (ps)
301	364.83	300.90	242	13.46	711
302	221.33	162.59	330	14.00	391
303	178.99	180.63	301	13.05	383
304	155.99	170.07	65	14.52	232
305	192.48	190.92	107	14.67	209
306	161.79	163.03	138	14.64	211
307	149.42	147.72	140	14.82	182
308	196.79	201.77	135	14.44	228
309	243.83	279.82	135	14.70	234
310	323.56	253.21	110	15.11	317
401	252.14	326.39	255	12.95	598
402	143.03	141.91	198	13.31	244
403	159.27	165.03	219	13.33	251
404	141.00	158.90	226	13.25	220
405	149.99	147.11	203	12.70	309
406	174.44	162.73	232	12.95	254
407	142.09	141.37	180	12.62	278
408	301.32	299.55	199	13.52	747

Figure 2.13: A table extracted from the database with the characteristics of the LTOF counters.

2.2.1 The genetic algorithm

Genetic Algorithm (GA)[20][21] is a search algorithm which seeks for optimal solution by sampling the solutions space to create a population of candidate solutions. These candidates are recombined and mutated to evolve into a new generation of solutions which may or not be better, that is closer to the desired optimum.

Recombination is fundamental to the GA and provides a mechanism for genetic mixing within the population. Mutation is vital in introducing new genetic material thereby preventing the search from stagnating. The next population of solutions is chosen among the parent and offspring generations in accordance with a survival strategy that normally favours the best individuals but nevertheless does not preclude the survival of the worst. In this way, a diverse pool of genetic material is preserved for the purpose of breeding yet better individuals.

Chance plays an important role in GAs, though their success in locating an optimum strongly depends on a judicious choice of a proper fitness function. The fitness function must be designed carefully to reflect the nature of the optimum and to direct the search along promising pathways. GAs operate on a population of individuals each of which has an assigned fitness. The population size should be sufficiently great to allow a substantial pool of genetic material, but not so large to degenerate into a random search. Those individuals that either undergo recombination or survive are chosen with a probability which depends on the fitness in some way.

To find an optimized disposition of the 144 PMTs of the 34 counters of the TOF, it is necessary to find the global minimum of the fitness function. For the algorithm I have chosen a population of 1000 candidate solutions and a mutation probability $\mu = 5\%$. Particular care was put in the design of the recombining and fitness function, because the problem presented many local minima. For the GA, I have chosen a number of generations equal to $5 \cdot 10^5$, because as one can see in fig. 2.14, over this number of generations the fitness function slows down sligthly. The global fitness function $F_{fitness}^{TOF}$ for all the TOF, is sum of four local fitness functions $F_{fitness}^{i}$ (one for each plane), weighted with different coefficients w_i. Each local fitness function is a sum of functions, reflecting the TOF requests:

$$F_{fitness}^{TOF} = \sum_i w_i F_{fitness}^{i} \qquad (i = 1...4) \tag{2.17}$$

$$F_{fitness}^{i} = \sum_j w_j f_j \qquad (j = 1...3) \tag{2.18}$$

where:

- f_1 requires same voltage for PMTs linked to the same HV channel;
- f_2 requires same gain to voltage dependence for PMTs linked to the same HV channel;
- f_3 requires similar voltage for PMTs on the same side of the same counter;
- w_j are the weights chosen for the components of the local fitness functions.

The PMT voltages are calculated in order to have a gain G_{eq} fixed (equalization gain). The first and the second function are imposed by the HV channels constraint. The third function requires PMT with similar transit time and time resolution, at the same side of a counter.

Moreover it was imposed the constraint that the PMT voltage has to be less then 2150V, to be able to increase the PMT gain during the long duration of the AMS-02 mission.

2.2.2 The simulated annealing algorithm

The method of simulated annealing (SA) [22] is a technique that has attracted significant attention for optimization problems of large scale, especially when a desired global optimum is hidden among many local extrema. At the heart of this method there is an analogy with the thermodynamics: a system with high temperature has molecules moving freely, but by cooling the system we arrive to a crystalline system with ordered molecules in the state of minimum energy. For slowly cooled system, nature is able to find this minimum energy state. In our case with the SA we start from a random PMT distribution on the TOF counters and, after each step, we slow down the temperature. The better disposition is evaluated with a cost function (equivalent to the fitness function for the GA, see eq. 2.17). After several steps we arrive to a state of minimum energy of the system, which corresponds to an optimized distribution of the PMTs on the TOF counters.

2.2.3 Final disposition

The initial parameters for the SA and the GA were the same: PMTs voltage and HV channel links; also the cost/fitness function was equal, with the same coefficients. The two algorithms singularly had similar (but not very satisfying) performances. Then it was used the result of SA, which is more adapted to search

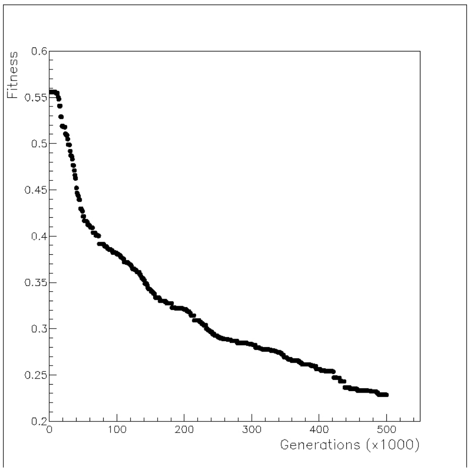

Figure 2.14: Fitness function for the genetic algorithm.

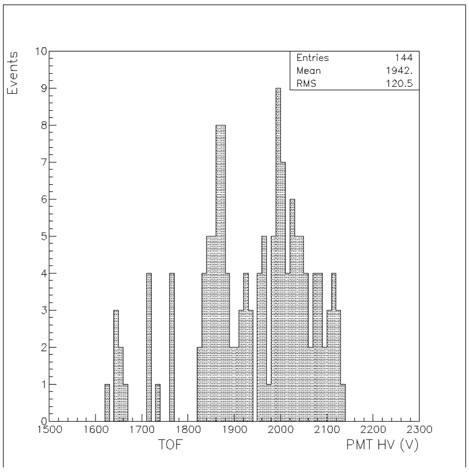

Figure 2.15: PMTs voltage distribution, for the final disposition.

solutions in a space with many local minima, as input to the GA, which is a greedy algorithm. So, the genetic algorithm searched a solution in the neighborhood of the simulated annealing one. The final solution was the acceptable disposition for the TOF.

In the final disposition, PMTs connected to the same HV channel, show a maximum voltage difference equal to 30V (fig. 2.16). For these PMTs it will be setted the mean of the voltage yield by the GA (HV_{mean}). As a consequence, the maximum relative gain difference[7] will be $\Delta G/G_{eq} = 12\%$ (fig. 2.17). For the TOF PMTs, the gain as a function of the voltage is:

$$Log(G) = P_1 + P_2 Log(V) \qquad \Rightarrow \qquad \frac{\Delta G}{G} = P_2 \frac{\Delta V}{V} \tag{2.19}$$

where P_1 and P_2 are constants found by PMTs calibration.

Fig. 2.18 shows the maximum variation of P_2 for PMTs with the same HV channel. PMTs on the same side of the same counter, have a mean voltage difference of about 7 V (fig. 2.19), with a maximum difference of 25 V. Finally the PMTs mean voltage is 1942 V (see fig. 2.15), much less then 2150 V, the limit imposed by the algorithm.

---

[7] The gain is relative to G_{eq}, the fixed value of the gain to have the PMTs responses equalized at the counter center.

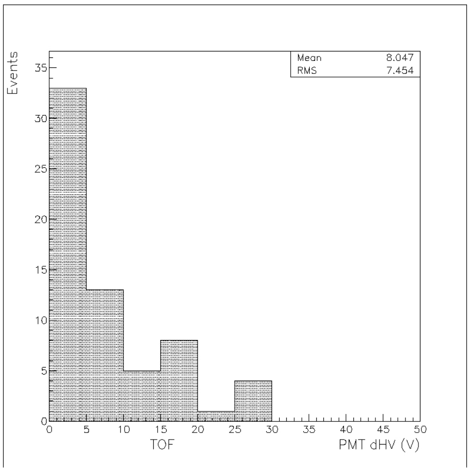

Figure 2.16: Differences of voltage calculated by the genetic algorithm for PMTs with the same HV channel (final disposition).

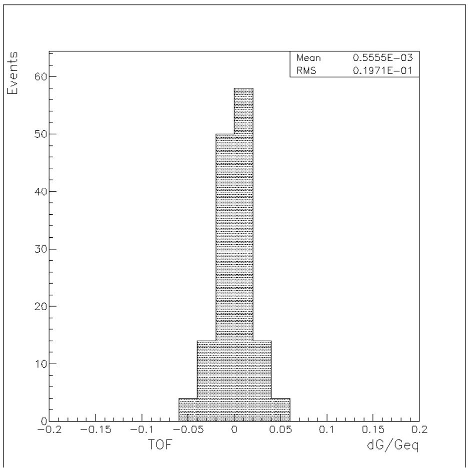

Figure 2.17: Relative gain difference for PMTs connected to the same HV channel (final disposition).

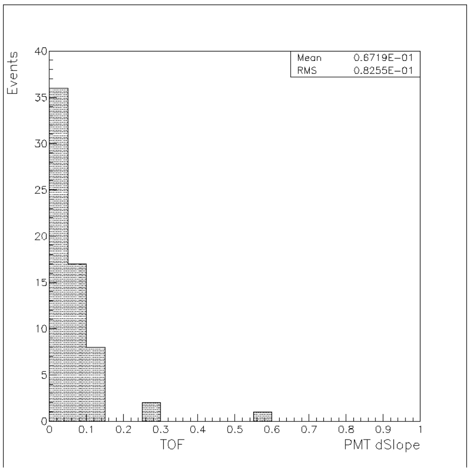

Figure 2.18: Difference on P_2 (see eq. 2.19) for PMTs connected to the same HV channel (final disposition).

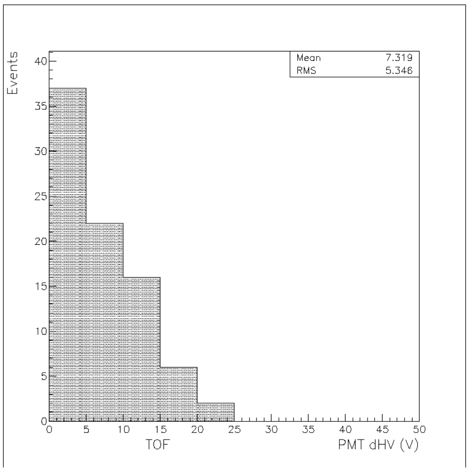

Figure 2.19: HV difference for PMTs on the same side of the same counter (final disposition).

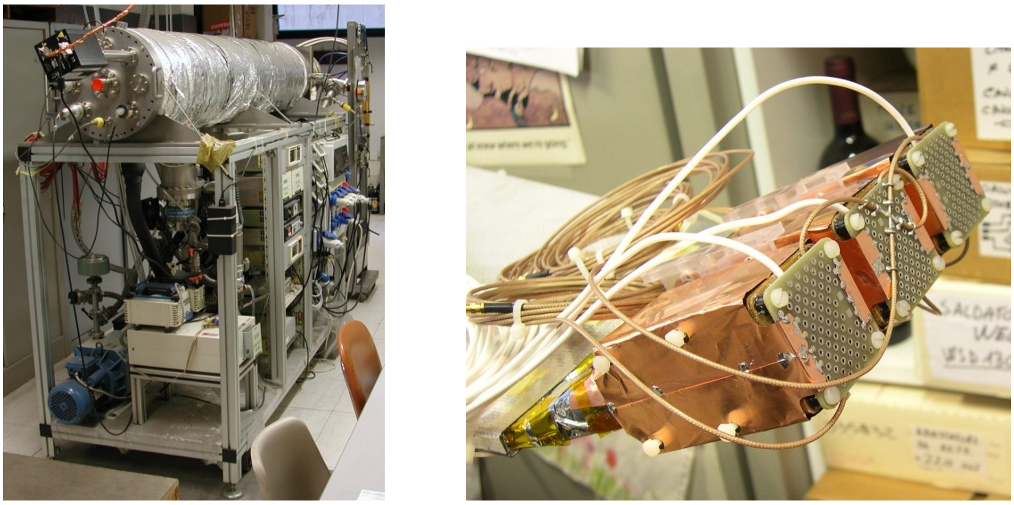

Figure 2.20: The space simulator used for the vacuum test of the TOF counters (left). The PMTs are wrapped with a copper shield to avoid discharge effects in vacuum (right).

2.3 The vacuum test of the LTOF counters

The photomultipliers of the AMS TOF have to be powered with high voltage up to 2300 V: in order to avoid discharge effects in space, the high voltage areas of the PMTs bases were coated with an insulating polymer, and the PMTs are wrapped with a copper electrostatic shield (see fig 2.20 right).

I tested all the Lower TOF counters in vacuum, in the pressure range from 10^{-4} to 10^{-1} mbar.

In order to test the functioning of the TOF counters in space, in the Bologna laboratories is present a space simulator[23] (see fig. 2.20 left) which is a thermal-vacuum chamber able to simulate the conditions (pressure and temperature) of the International Space Station. Thanks to two primary pumps, and three turbo-molecular pumps the system can produce a vacuum up to pressure of $P \simeq 10^{-9}$ mbar. A thermal system composed by a cryostat and a thermal heater allows to have a temperature range from $-90^{o}C$ to $70^{o}C$.

After the assembly (see chap. 3), each counter has been tested at atmospheric pressure powering the photomultipliers at 2200 V and monitoring their currents with a multimeter and their anode signals with an oschilloscope.

Normally, the current of a TOF PMT at 2200 V is about 22 μA (the voltage divider has a resistance R = 100 $M\Omega$), and to safe the photomultiplier, I limited the maximal current provided by the power supply at 50 μA (to avoid the PMT damage).

If the PMTs have a normal behaviour at atmospheric pressure, the counter can be tested in vacuum. The PMTs are switched off and the counter is led to a pressure of about 10^{-4} mbar. The PMTs are powered and their conditions are monitored. The pressure is led up to 10^{-1} mbar and, if no discharge effects are manifested, the test is passed. Otherwise the PMTs whose show discharge effects are replaced and the test repeated.

For all the 18 counters of the LTOF it was necessary to replace only one PMT which did not pass the vacuum test.

Chapter 3

The Lower TOF assembly

The Lower TOF of the AMS-02 experiment is composed by 2 layers of scintillator counters: plane 3 and plane 4. Plane 3 is made up of 10 counters with tilted light guides, and plane 4 is made up of 8 counters with straight light guides. The tilted light guides are used in order to minimize the angle between the magnetic field and the axes of the photomultipliers. In this case the effect of the magnetic field on the photomultiplier response is minimized. The counters have rectangular shapes with the exception of the edge counters which have trapezoidal shape, in order to reduce the TOF weight (see fig 3.1). The counters, all 10 mm thick, have a standard width of 120 mm, apart the trapezoidal ones (180÷269 mm) and variable length (1170÷1340 mm). Each counter has 2 photomultipliers by side for redundancy, except for the trapezoidal counters of the plane 4, that have 3 photomultipliers by side. In total, plane 3 has 40 PMTs and plane 4 has 36 PMTs. All the materials used for the AMS experiment have to be space qualified and approved by NASA.

3.1 Counter assembly

The counters of the AMS TOF consist of plastic scintillators, coupled to fine mesh photomultipliers through light guides. All the counters of the LTOF have been assembled, tested in vacuum and characterized with the cosmic ray telescope from 2005.

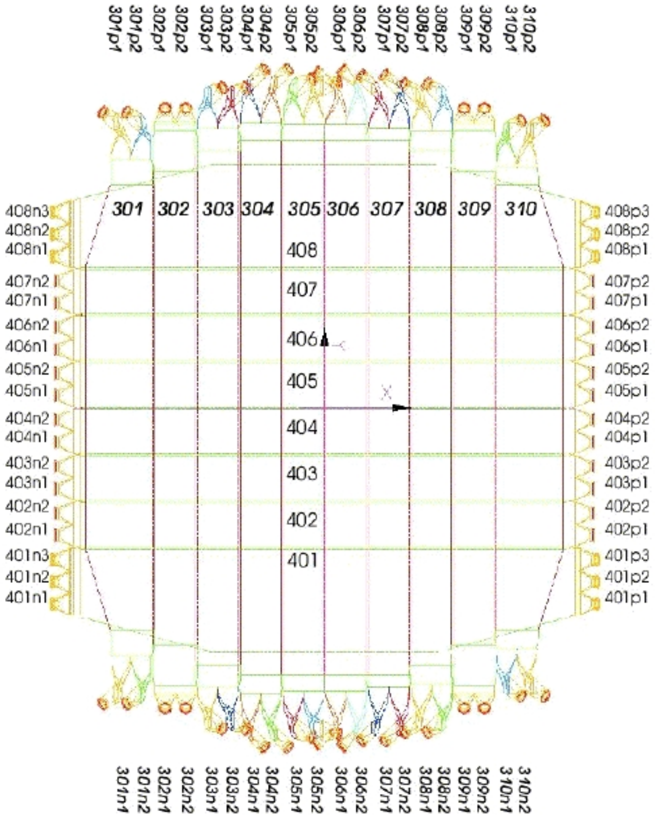

Figure 3.1: Lower TOF counters with rectangular and trapezoidal shape.

3.1.1 The plastic scintillator

The plastic scintillator used for the TOF counters is produced by Eljen-Technology (Texas USA), type EJ-200 with the characteristics[1] summarized in fig. 3.2.

The plastic scintillator combines the two important properties of long optical attenuation length and fast timing. It consists of polyvinyltoluene, an organic polymer which is luminescent when it is irradiated by ionizing radiation. The scintillator is wrapped with aluminized Mylar foils, leaving a thin layer of air between the two materials, in order to enhance the total internal reflection and to allow all light to be utilized. The Mylar acts also as a protection for the scintillator

---

[1] From the Eljen-Technology data sheet.

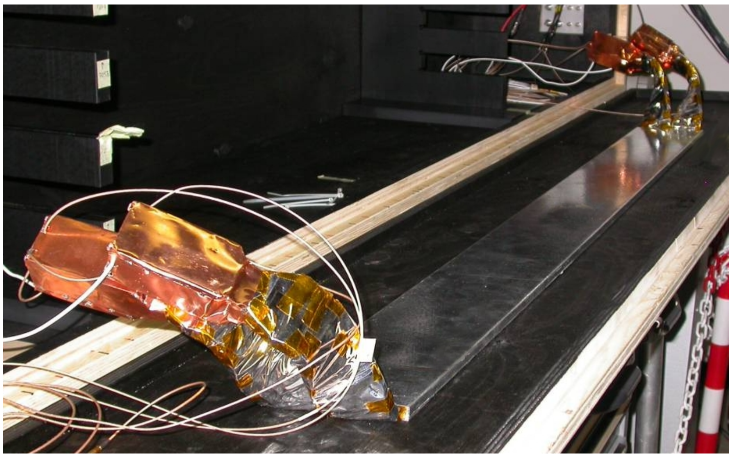

Physical and Scintillation Constants:

Light Output, % Anthracene	64
Scintillation Efficiency, photons/1 MeV e^-	10,000
Wavelength of Max. Emission, nm	425
Rise Time, ns	0.9
Decay Time, ns	2.1
Pulse Width, FWHM, ns	~2.5
No. of H Atoms per cm^3, x 10^{22}	5.17
No. of C Atoms per cm^3, x 10^{22}	4.69
No. of Electrons per cm^3, x 10^{23}	3.33
Density, g/cc:	1.023

Polymer Base: .... Polyvinyltoluene
Refractive Index: 1.58
Vapor Pressure: .... Is vacuum-compatible
Coefficient of Linear Expansion: .... 7.8 x 10^{-5} below +67°C

Light Output vs. Temperature:
At +60°C, L.O. = 95% of that at +20°C
No change from +20°C to -60°C

Chemical Compatibility: Is attacked by aromatic solvents, chlorinated solvents, ketones, solvent bonding cements, etc. It is stable in water, dilute acids and alkalis, lower alcohols and silicone greases. It is safe to use most epoxies and "super glues" with EJ-200.

EJ-200 EMISSION SPECTRUM

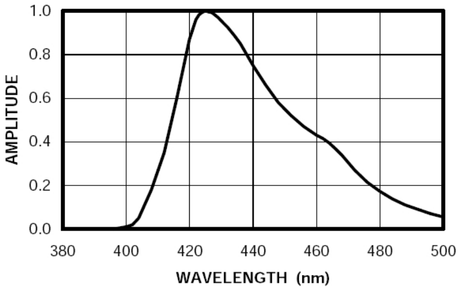

Figure 3.2: A counter assembled for the AMS Time of Flight (above). Characteristics of the plastic scintillators used in the TOF counters (below).

Figure 3.3: Light guides used for the TOF counters. They are tilted for the counters of plane 3 in order to minimize the influence of the magnetic field on the PMT response.

surface. It is externally aluminized in order to shield from external light and to reflect internal scintillation light. The detector is sealed from light and covered with 2 carbon fiber shells coated with alluminium. The carbon fiber gives the rigidity to the counters and protect it from mechanical stress. The two shells are cemented with araldite AV138M.

3.1.2 The light guides

The light guides (see fig. 3.3) consist of plexiglass material which has a similar refraction index as the scintillator. They are glued to the scintillator with the Three Bond 1743 adhesive cyanoacrylate, and they are wrapped with Mylar foil in order to enhance the internal reflection of the light.

The light guide are coupled to the photomultiplier through a round transparent pad (Dow Corning 93-500, a space-qualified silicone polymer) which has a similar refractive index as the light guide. This pad is used instead of the usual optical grease because it is an elastic material and it gives a soft coupling between the PMT photocathode and the light guide. The coupling is assured tightening diamagnetic screws (see fig. 3.7).

3.1.3 The photomultipliers

The photomultiplier tubes are Hamamatsu fine-mesh type R5946 (see fig. 3.4), with cylindrical shape (39 mm diameter and 50 mm length), chosen for their good

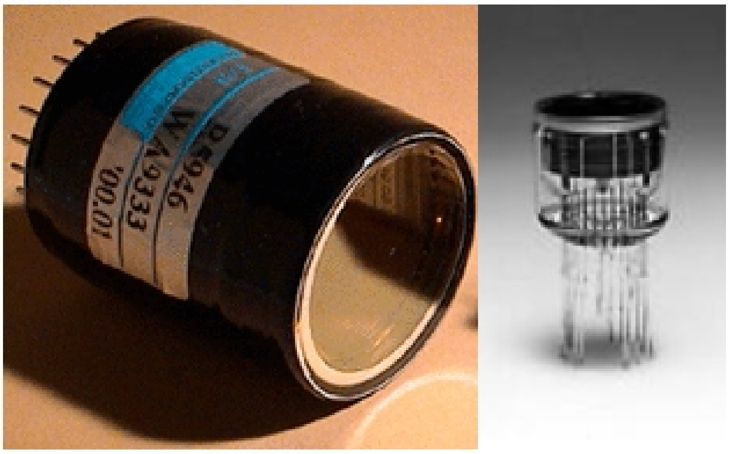

Tube Diameter	Type Number	Spectral Response Range(nm) & Curve Code	ⓐ Outline No.	ⓑ Socket	No. of Stages	Cathode Sensitivity			Anode Sensitivity							
						Luminous Typ. (μA/lm)	Blue Sens. Index (CS 5-58) Typ.	Q.E at Peak Typ. (%)	Luminous Typ. (A/Lm)	Nominal Gain ⓓ			Supply Voltage ⓓ for Nominal Gain at 0 T		Dark Current at ⓓ Nominal Gain at 0 T	
										(at 0 T)	(at 0.5 T)	(at 1 T)	Typ.(V)	Max.(V)	Typ. (nA)	Max. (nA)
38 mm (1.5")	R5946	300 to 650 400K	②	E678-19D	16	80	9.5 (7.0)	23	80	1.0×10^6	4.3×10^5	2.9×10^4	1800	2300	5	30

(at 25 °C)

Time Response (Typ) at 0 T ⓗ			Pulse Lineatiy (Typ) at 0 T ⓘ		Maximum Rating ⓔ						Notes	Type No.
Rise Time (ns)	Transit Time (ns)	T.T.S. (FWHM) (ns)	± 2% Deviation (mA)	± 5% Deviation (mA)	Anode Lumi-nous (A/Lm)	Anode ⓕ to Cathode Voltage (V) at 0 T	Anode to Cathode Voltage (V) over 1 T	Cathode to Dy1 Voltage (V)	Dynode to Dynode Voltage (V)	Average ⓖ Anode Current (mA)		
1.9	7.2	0.35	350	500	800	2300	2800	400	200	0.01	UV Type (R6148) Synthetic Silica Type (R6149)	R5946

Figure 3.4: Photomultiplier tube fine-mesh type R5946 and its characteristics (from Hamamatsu data sheet). This PMT is chosen for the AMS TOF counters, because it has good performance in high magnetic field.

performance in presence of high magnetic field. The PMT has bialkali photocathode, a borosilicate glass window and 16 bialkali dynodes. The characteristics from the Hamamatsu data sheet are shown in fig. 3.4. The spectral response has a range from 300 to 650 nm with a peak at 420 nm (corresponding to a quantum efficiency of about 20%). The gain is about 10^6 and the maximum supply voltage is 2300V (see fig 3.5 above) and the transit time about 7.2 ns.

The photomultipliers have been calibrated [24] in 2003 to determine their gain as a function of the voltage supply. They have been arranged to the TOF counters depending on their characteristics utilizing meta-heuristic algorithms (see chap. 2). The PMT response has been studied in presence of magnetic field with measures[25] (see fig. 3.5 below) and a Monte Carlo simulation[26]. The

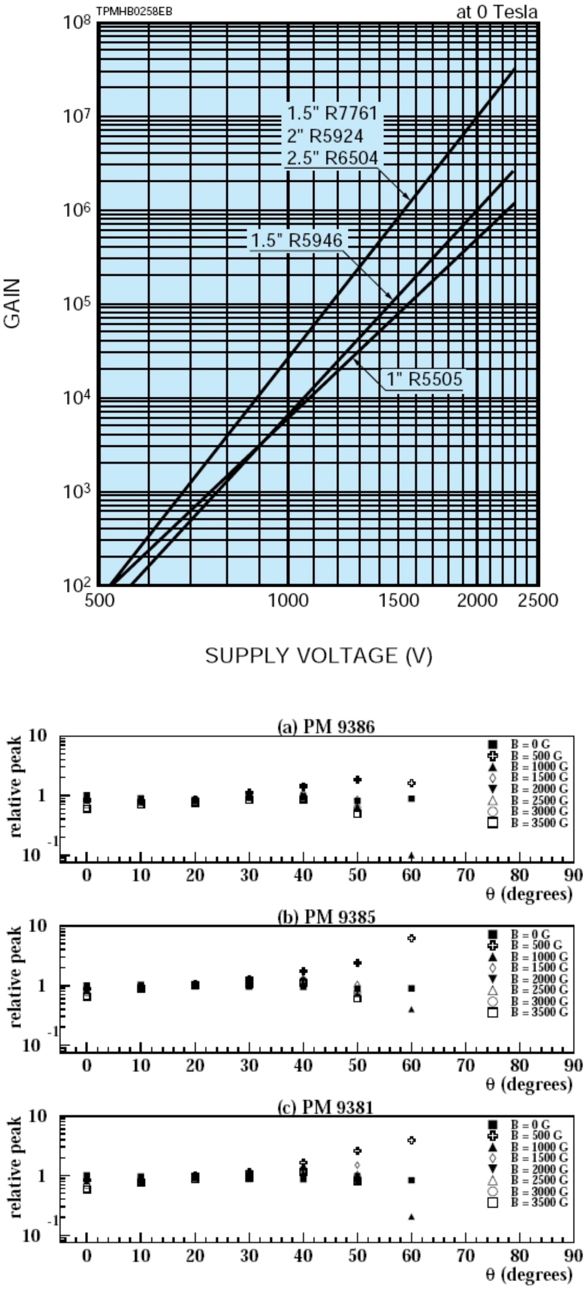

Figure 3.5: Above: Hamamatsu PMTs R5946 gain as a function of the voltage at B = 0 T (from Hamamatsu data sheet). Below: PMTs behaviour as a function of the θ angle between the tube axis and the field direction, for different values of the magnetic field B (normalized to B=0).

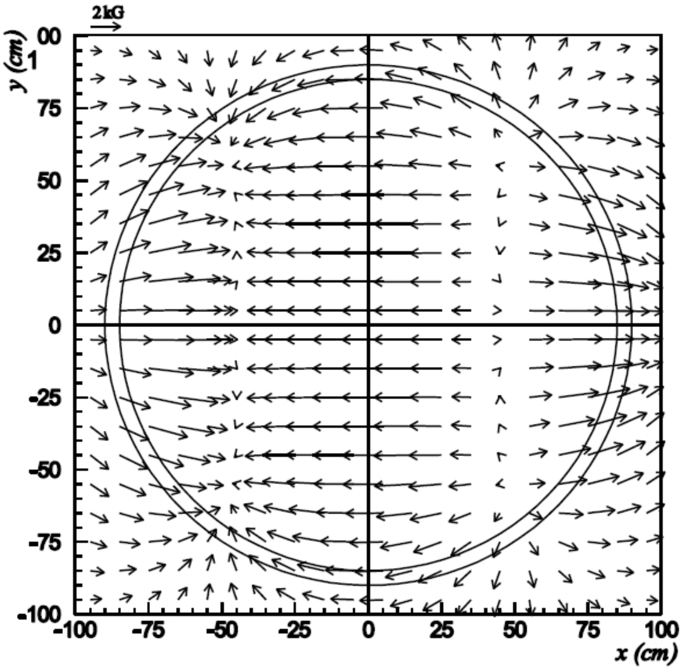

Figure 3.6: Magnetic field map in the TOF PMTs region. The ring shows where the PMTs are positioned.

magnetic field intensity in the region of the TOF photomultipliers reaches values of the order of 2.5 kG, with a complicate direction distribution (see fig. 3.6).

Black shells of plastic material include the PMT, the silicone pad and the edge of the light guide (see fig. 3.7). In addition, the printed circuit boards (PCB) hosting the PMT voltage divider, are fixed to the rear of the black housing through diamagnetic screws. In order to protect them against low pressure discharges, the PMT pins and the lower PCB are potted with Dow Corning silicone, the same material used for the optical pad. The rest of the electronics is coated with Nusil CV-1152, while the light tightness is obtained using the black CV-1146-2 Nusil product. The PMT housing has been wrapped with a thin copper foil, used as electrostatic shield.

Each counter has 2 or 3 PMTs by side. From the PMTs we read a dynode and the anode signals. The dynode signal is read individually for each PMT, while the anode signals are summed together (for PMTs of the same couter side) in order to

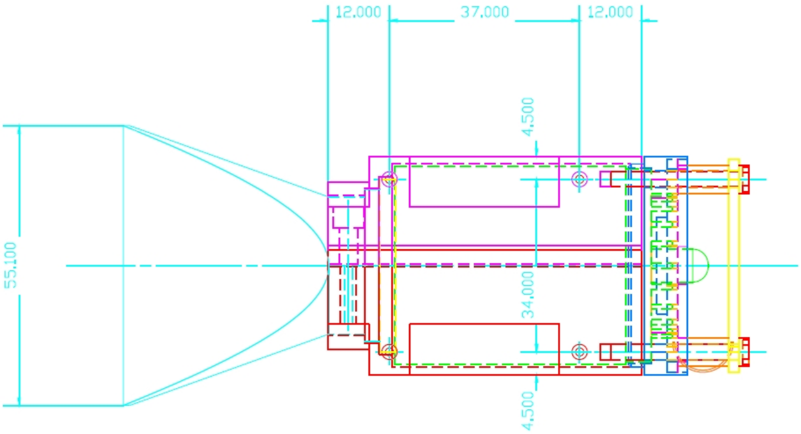

Figure 3.7: Mechanical fixation of the PMT to the light guide.

have a high signal for the trigger.

3.2 Lower TOF assembly

The Lower TOF was assembled from January up to April 2006, after that all the counters were tested in vacuum and characterized with the cosmic rays telescope.

For the assembly has been used a table, with a rotating plane, designed by INFN. This table allows also the transport of the LTOF.

The structural part of the Lower TOF is composed by a ring in heat-trated aluminium which allows the connection, through special rods, of the detector to the Unique Support Structure (USS) which is the backbone of the AMS experiment. A flat large alluminium honeycomb panel (see fig. 3.8) supports the LTOF, and it is the interface from the LTOF and the Aerogel container of the RICH detector.

3.2.1 The mechanical assembly

The housing of the LTOF is represented by two special covers: one for plane 3 and one for plane 4. These covers are in carbon fiber with an external film of alluminium. They are fixed together through structural screws provided by NASA and sealed by a gray adhesive epoxy. Inside the cover are the TOF counters, of

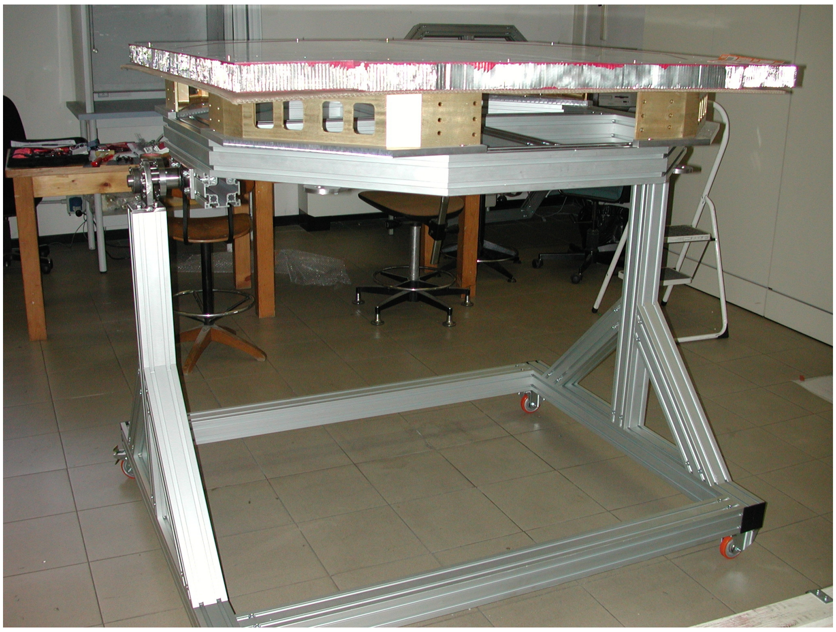

Figure 3.8: The support structure for the LTOF.

plane 4 below and plane 3 above. To have the maximum of the efficiency, the counters of each plane are overlapped by 5 mm, by mean of carbon fiber supports, that also fix the counters together. Over the counters are placed slices of poron, a cellular urethane foam material which absorb the vibrations. The counters of plane 4 and plane 3 are orthogonal in order to provide a certain granularity at the trigger level (see fig. 3.9).

The PMTs are fixed to the structure by means of pieces of Makrolon, a transparent polycarbonate, that withstands high and low temperatures. All the PMTs are labeled with strips of Kapton tape, in order to identify them during the cabling. To fix the LTOF parts internally are used heat treated alluminium 7075-T7351 screws.

The temperature of the PMTs is mantained over -30^{o}C by means of heaters, in order to assure their good functionality. The heaters are controlled by thermostats displaced near the photomultipliers (see fig. 3.10). The heaters are powered through cables in PTFE (teflon) and they have been tested during the Thermal Vacuum Test of the Lower TOF (see chap. 4).

In order to monitor the internal temperature of the Lower TOF, 32 Dallas sen-

Figure 3.9: Lower TOF: plane 3 and plane 4 assembled orthogonally.

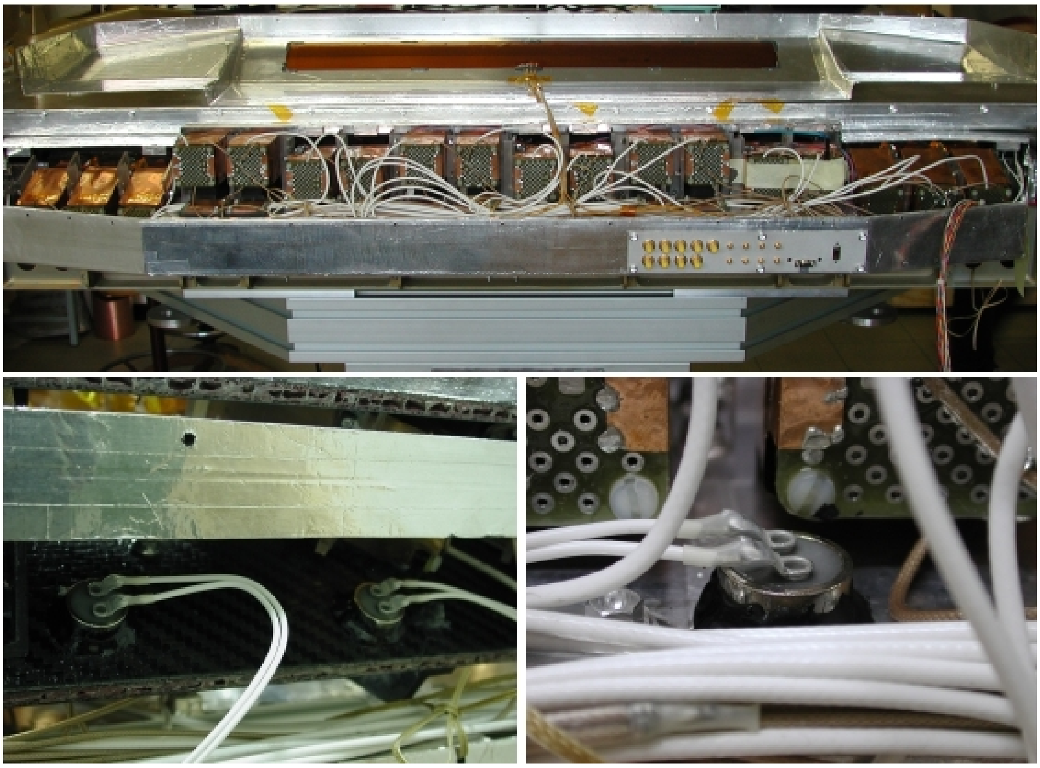

Figure 3.10: A heater (above) controlled by thermostats (below) keeps the temperature over -35^{o}C, the minimum operating temperature for the PMTs.

sors type DS18S20 are installed on PMTs and SFEC cards. For each plane there are two Dallas chains (A and B for redundancy) with 8 sensors each. They are glued on TOF with gray adhesive epoxy, the same used for the screws. The exact position of the Dallas is given in table 3.1. These sensors measure the temperature from -55^{o}C to 125^{o}C with an accuracy of $\pm$0.5^{o}C over the range of -10^{o}C to 85^{o}C.

Name	Sensor ID	Position
TOF-3-DS0A	9A000800AAD94C10	SFEC 3n
TOF-3-DS1A	97000800AA972B10	302n1
TOF-3-DS2A	99000800AAE08910	305n2
TOF-3-DS3A	D8000800AAC43110	309n2
TOF-3-DS4A	12000800AAB8A010	301p2
TOF-3-DS5A	73000800AAA8D710	305p2
TOF-3-DS6A	80000800AAF14810	309p2
TOF-3-DS7A	CB000800AAB78010	SFEC 3p
TOF-3-DS0B	37000800AAFF7310	SFEC 3n
TOF-3-DS1B	C7000800AB052E10	302n1
TOF-3-DS2B	3D000800AAF97A10	305n2
TOF-3-DS3B	D0000800AADC3C10	309n2
TOF-3-DS4B	A5000800AAA70B10	301p2
TOF-3-DS5B	7D000800AAB3C410	305p2
TOF-3-DS6B	EC000800AAAD6A10	309p2
TOF-3-DS7B	5F000800AAEAB010	SFEC 3p
TOF-4-DS0A	8B000800AADE1E10	SFEC 4n
TOF-4-DS1A	8E000800AAF67E10	402n2
TOF-4-DS2A	DA000800AB013D10	404n2
TOF-4-DS3A	6A000800AAFD6410	406n2
TOF-4-DS4A	D8000800AAD68A10	401p1
TOF-4-DS5A	F2000800AAF86910	404p1
TOF-4-DS6A	52000800AAE97410	406p1
TOF-4-DS7A	E5000800AAC8C310	SFEC 4p
TOF-4-DS0B	EC000800AAAF5810	SFEC 4n
TOF-4-DS1B	8C000800AAC96810	402n2
TOF-4-DS2B	F0000800AAB0A410	404n2
TOF-4-DS3B	C9000800AAF3E110	406n2
TOF-4-DS4B	21000800AA953910	401p1
TOF-4-DS5B	20000800AAAEDD10	404p1
TOF-4-DS6B	12000800AABFEF10	406p1
TOF-4-DS7B	43000800AA944810	SFEC 4p

Table 3.1: Position of the Dallas sensors in the Lower TOF.

3.2.2 The electronic cabling

All the cables from the detector to the external electronics are connected to four panels (one for each half a plane), through specific and space qualified connectors (see fig. 3.11 and fig. 3.13).

The PMTs are powered in pairs through coaxial HV cables, and high voltage dividers, following the scheme of fig. 3.12. The voltage dividers split the HV, in order to power two PMTs with the same HV channel. The HV cables are connected to the panels through Reynolds connectors (series 600), space qualified.

The PMTs anode signals are carried by cables with 50 Ω impedance, and connected to the TOF panels through Radiall connectors type SSMB.

The PMTs dynode signals are carried by the same cables used for the anode signals, to the SFEC cards installed internally to the LTOF covers. There are 4 SFEC (see chap. 4), each one reads out the dynode signals of the PMTs of half a plane. The SFEC cards are connected to the panels of the LTOF through PTFE cables (26AWG) and AirBorn μD connectors. All the weldings in the SFEC cards have been coated with Nusil CV-1152.

The flight model of Lower TOF totally assembled is shown in fig. 3.14.

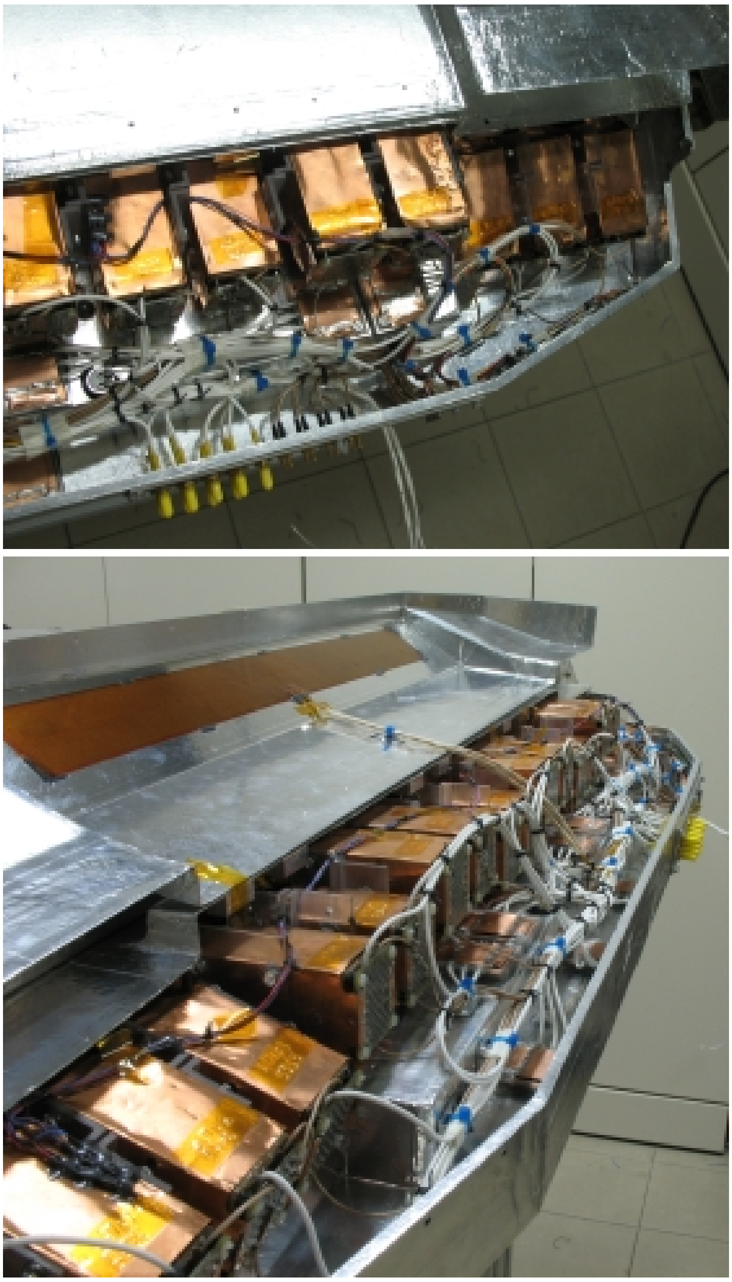

Figure 3.11: Lower TOF internal cabling. In the two pictures the Dallas sensors on the PMTs, the HV dividers, the heaters and all the cables that carry HV and signals from the detector to the panel, are shown.

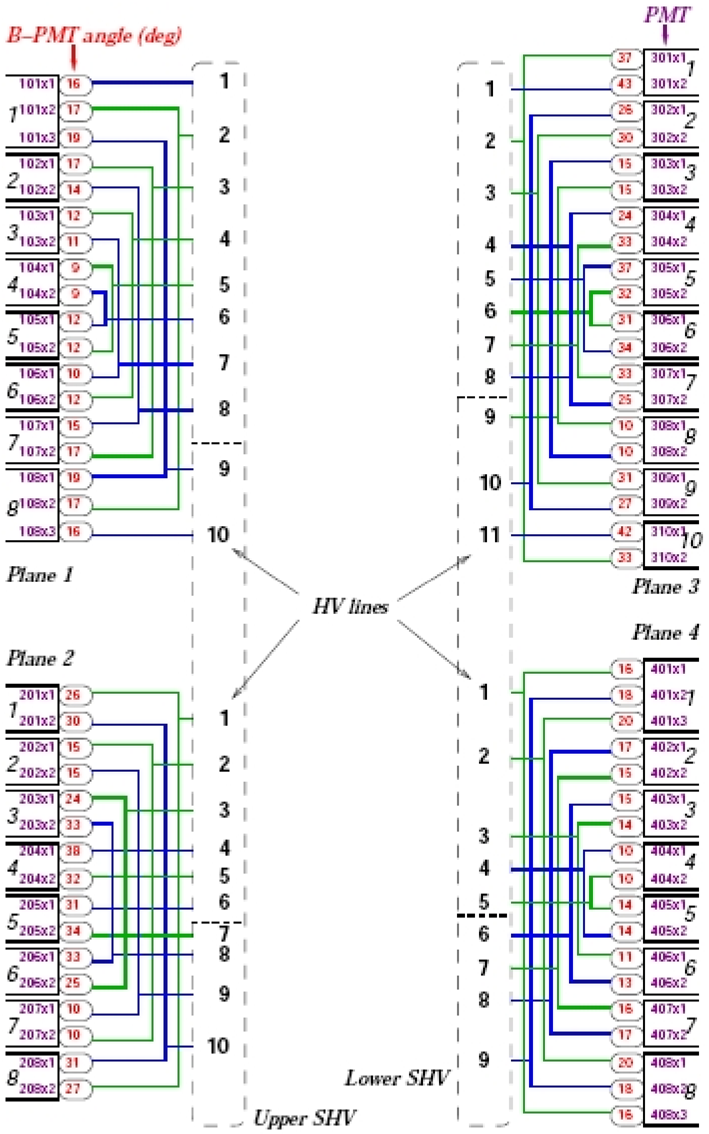

Figure 3.12: Scheme of the HV channel links used to power the PMTs of the TOF counters. The PMTs linked by the same line will be powered with the same voltage.

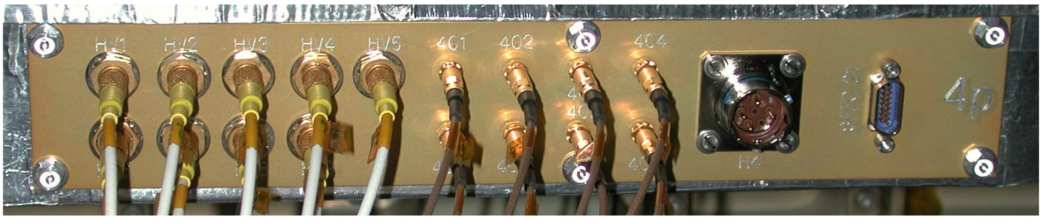

Figure 3.13: TOF panel with the specific and space qualified connectors.

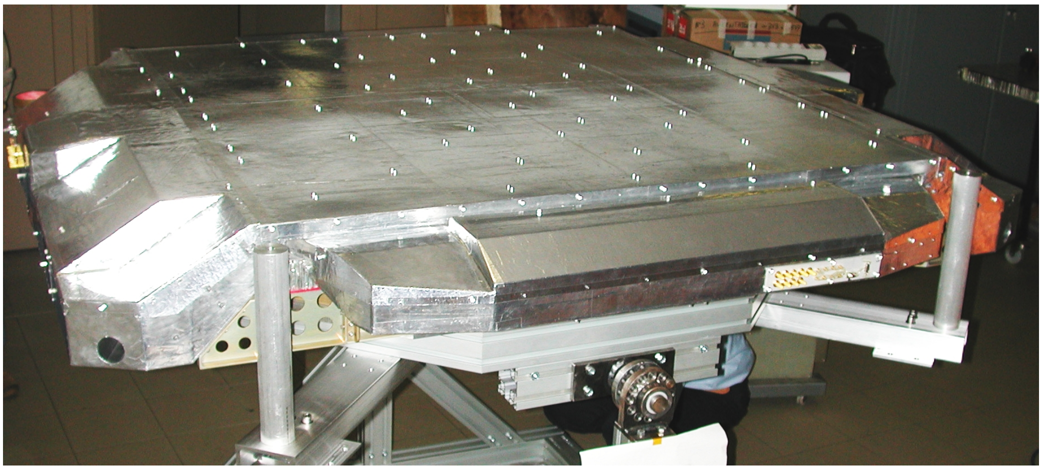

Figure 3.14: The Lower TOF totally assembled.

Chapter 4

Space qualification tests of the Lower TOF

The flight LTOF detector space qualification required by NASA consists of: a thermal cycling between extreme temperatures in vacuum (Thermal Vacuum Test) and a static and dynamic stress test on a vibrating table (Vibration Test). The Thermal Vacuum Test (TVT) was performed from the 2^{nd} of May until the 10^{th} of June 2006 at the SERMS Laboratories in Terni[1], with the supervision of the Carlo Gavazzi Space, in order to verify the performances of the Lower TOF in the extreme conditions in which it will operate on the International Space Station. Moreover in October 2006, at SERMS, a random vibration test has been performed, with the supervision of the INFN. Functional tests were executed in order to monitor the behaviour of the scintillation counters, PMT and detector electronics, and to read out the PMTs signals for a detailed off-line analysis. Space qualification tests were performed in order to assure the safety conditions required by NASA for payloads using the Space Shuttle and the International Space Station. Functional tests were performed in order to verify that the apparatus will guarantee the mission success.

I attended all the phases of the space qualification tests and I performed all the functional tests, taking care, in particular, of the trigger logic for the data acquisition.

---

[1] http://serms.unipg.it/

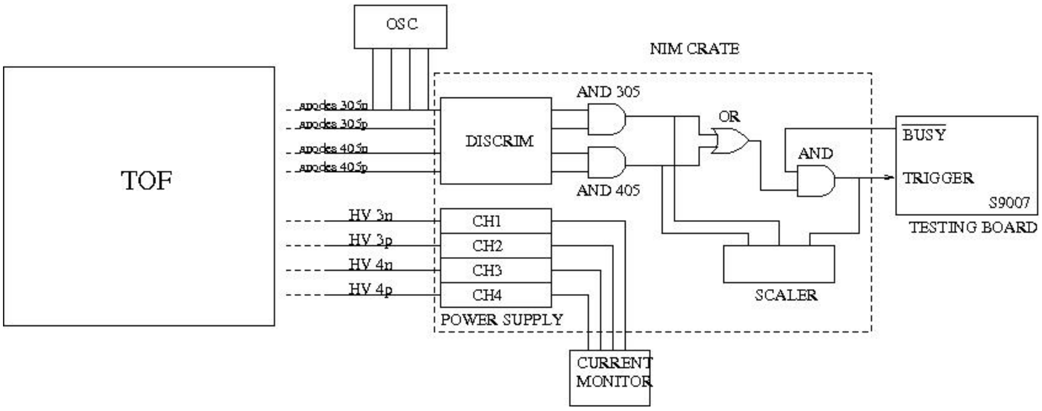

Figure 4.1: The scheme of the trigger logic used for all the functional tests.

4.1 Functional tests of the LTOF

The functional tests intend to check the status of the LTOF during the space qualification tests. They consist in the acquisition of the signals by all the PMTs of the LTOF counters, in order to monitor the charge spectra of cosmic rays crossing the scintillation counters. The setup used for the functional tests is composed by a trigger logic, a power supply, an electronic read out system for the acquisition of the signals by the PMTs, a temperature sensors read out system, and computers for the online monitor of the data.

During the functional tests the PMTs of the LTOF were powered with four channels of a CAEN N472 power supply, at fixed voltage (1950V, 2050V or 2150V). Each channel powered half a plane of the LTOF, so 2 channels powered the 40 PMTs of plane 3 and 2 channels the 36 PMTs of plane 4. The current provided by each channel of the power supply was monitored through a software which stored the four current values, in order to check the status of the PMTs, discharge effects or power failures. The current absorbed by each PMT is about 20 μA with a voltage of 2000 V. To protect the PMTs the maximum current provided by the power supply was limited at 10% more than the normal current value required by the PMTs.

For the trigger logic I used NIM modules (see fig. 4.1): the anode signals produced by the cosmic rays at both sides of the LTOF central counters (305 and 405, see fig. 4.2) were discriminated with thresholds between 50 mV (for HV=1950V) and 100mV (for HV=2150V). These discriminated signals were put in a coincidence module. The counter 305 triggered the acquisition for plane 4 and the counter 405 triggered the acquisition for plane 3, selecting the cosmic rays crossing the central slices of the counters. The OR signal of the two coincidences (from the two central counters) gave the detector trigger. This trigger in coincidence with the $\overline{BUSY}$ signal of the electronic data acquisition board (S9077), was the data acquisition trigger.

Moreover a scaler module was used to count the coincidences of the trigger counters (305 and 405) and of the data acquisition trigger signal. The coincidences rate of the trigger counters was about 50Hz and that of the acquisition was about 20 Hz.

The anode signals of each side of the two central counters were not acquired, but monitored and stored, through screenshots (see fig. 4.3), with a digital oscilloscope, triggered by the acquisition trigger.

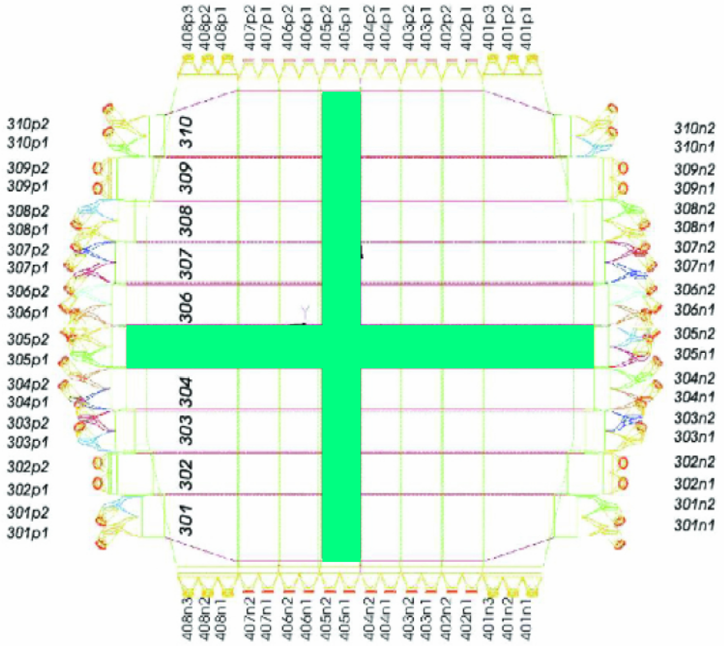

Figure 4.2: During all the functional tests the anodes signals from both sides of the central counters (305 and 405) of the LTOF were used to form the trigger signal for the data acquisition system.

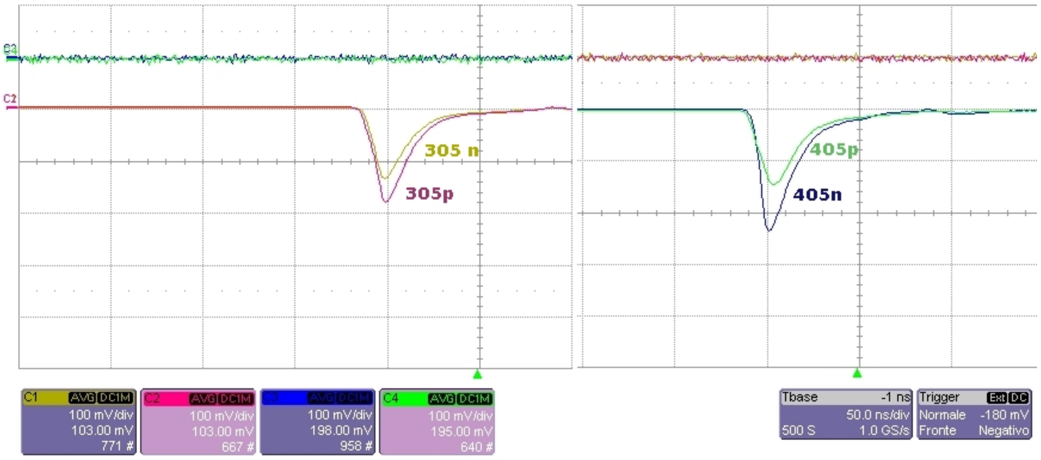

Figure 4.3: The anode signals of the counters 305 (left) and 405 (right) were monitored at the oscilloscope, triggered by the trigger signal of the data acquisition.

The PMTs dynode signals were read out by 4 flight model SFEC[2] cards located inside the LTOF. The anode signals were read out by 2 custom boards (SFEC like for negative signals), built for these tests and positioned externally to the LTOF. The anodes of the counters 305 and 405 were used to form the trigger signal, and for this reason they were not acquired. The SFEC cards[27] (see fig. 4.4) are composed of a charge measurement block, which measures the charge collected from the dynodes of the PMTs and make the time integral of the current pulse, and an ADC for the signal digitalization. The charge measurement block is composed by a custom chip (AICPPP) designed by the AMS collaboration, available for negative and positive signals. In the AMS-02 detector, the SFEC boards will be read by the SDR[3] board, while for these tests, it was used a testing board (CAEN S9007 module), which simulates the SDR, acquiring data and sending them to the PC through a serial port. The testing board was used also to generate the BUSY signal needed for the veto of the acquisition.

The read out (during the thermal vacuum test) of 32 temperature sensors (Dallas DS18S20)[4] installed in pairs in several points of the LTOF (PMTs and SFEC cards, see paragraph 3.2) was performed with a custom electronic board and the

---

[2] Scintillator Front End Charge.

[3] Scintillator Data Reduction.

[4] http://www.maxim-ic.com/

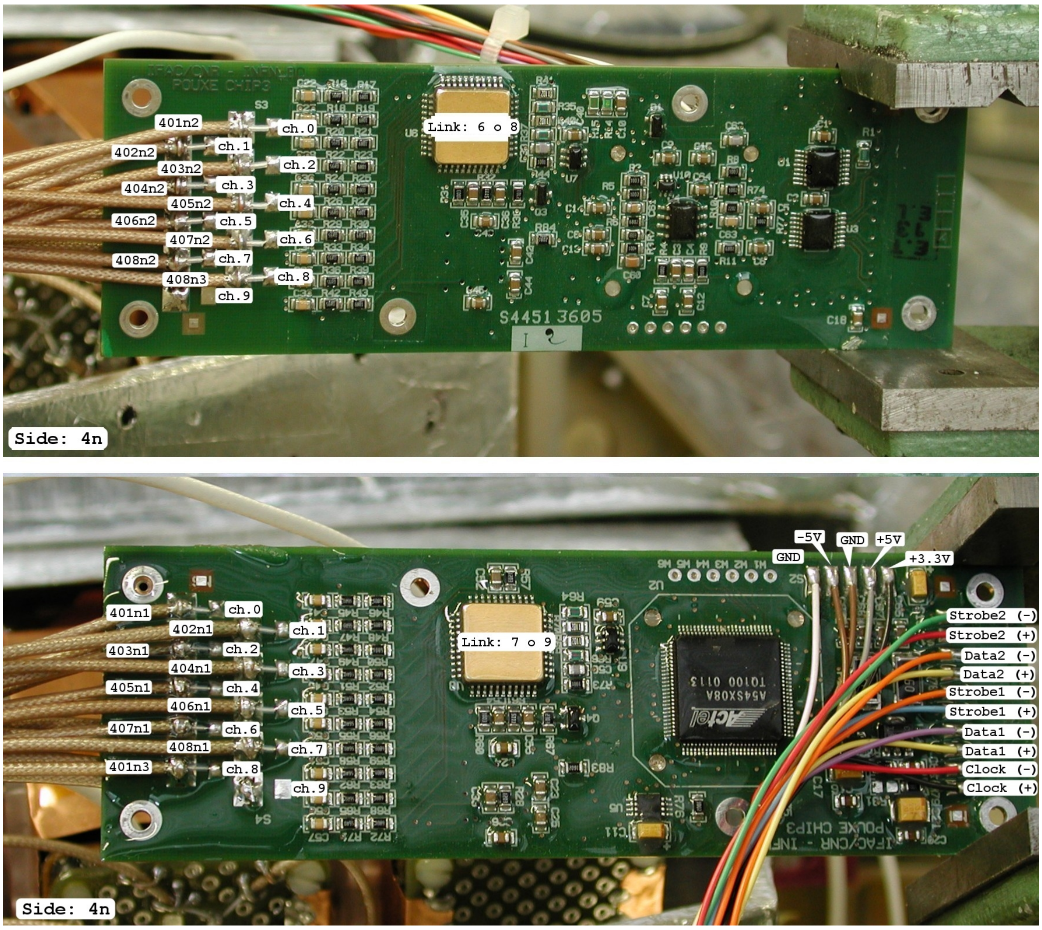

Figure 4.4: The flight model of the SFEC card.

same software used by the current monitor, in order to have a detailed check of the LTOF temperatures.

During the TVT the test of the heater circuits present in the LTOF (see paragraph 3.2) was performed. The heaters must be switched on automatically by suitable thermostatic switches when the temperature of the PMTs will go below -35^{o}C.

The data acquisition was checked by an on line monitor software, that allowed to plot the charge spectra of the PMTs. An accurate off line data analysis was performed in order to check the performances of the detector. To have a good statistics for the analysis, more than 50000 events for each run were acquired. For all the functional tests 120 runs were executed, for about 3 GB of data.

The first functional test of the LTOF was performed in May 2006 in the Bologna laboratories, just before the LTOF transport to the SERMS for the space qualification tests. This test was necessary to monitor the status of the detector after its assembly.

At SERMS other functional tests were performed just before, during and after the thermal vacuum test and after the vibration tests.

4.2 The LTOF thermal vacuum test

The thermal vacuum test (TVT) consisted of two parts, a thermal vacuum cycling and a thermal balance (see fig. 4.5): four cycles in vacuum chamber were performed to demonstrate the ability of the LTOF to operate when exposed to extreme operational temperatures, after being exposed to non-operational in vacuum environment. The tolerance on maximum and minimum temperatures were 3^{o}C and the temperatures were measured with a maximum uncertainty of 1.5^{o}C. During the operating phases, in the first characterizing cycle, the temperature reference point (TRP) was increased/decreased by steps of 2^{o}C until the temperature sensors on the PMTs measured a temperature equal to the limits shown in fig. 4.5. During the first cycle, at the minimum temperature (-35^{o}C) the heaters and thermostats operating tests were performed. In the last cycle the thermal balance part (TB) was performed, during which the temperatures were stabilized for 5 hours at the maximum (hot balance) and at the minimum (cold balance) operative temperatures. This part has been used for the thermal model correlation of the LTOF. The Hamamatsu specifications for the PMTs provided the reference for the maximum and minimum operating temperatures. The LTOF temperature was

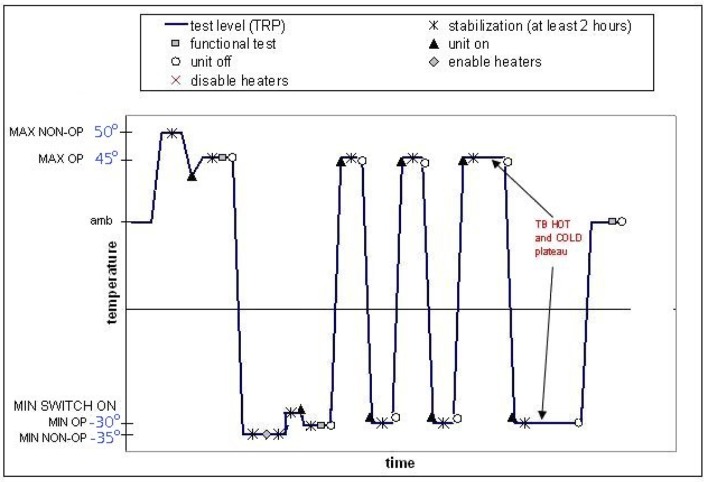

Figure 4.5: Thermal vacuum test: temperature profile.

monitored internally through 32 flight sensors (on PMTs and SFEC cards) and externally through 44 sensors. The heat exchange was mainly via radiation.

A delicate phase was the trasport of the LTOF at the SERMS laboratories in TERNI. The detector was fixed into a wooden box, wrapped up and brought to Terni with a truck. In order to avoid dangerous vibrations due to the transport, four pneumatic tyres under the box (see fig. 4.6) were used.

At SERMS the LTOF was unpacked and prepared for the TVT in a clean room (class 100,000), with controlled temperature and humidity. Into the clean room one had to wear gloves, shoe covers, hoods, caps and gowns. Before the LTOF insertion into the vacuum chamber, the Gavazzi engineers provided to locate the 44 thermal sensors (PT100), externally on all the LTOF. These sensors together with the flight Dallas sensors give the status of the temperature of the detector. Another delicate phase was the LTOF insertion in the vacuum chamber (see fig. 4.7): a dedicated structure was designed to support the detector on the chamber baseplate. Then we provided to connenct the electronic cables and to prepare the acquisition setup for the functional tests. When the detector was into the vacuum chamber a functional test was performed, before starting the TVT, in order to verify that the transport had not damaged the detector.

The vacuum chamber of the SERMS laboratories is equipped with an inner cylindrical radiator (shroud) with diameter 2.1 m and length 2.1 m. It allows to reach a minimum pressure (nominal value) of $5 \cdot 10^{-5}$ mbar and a temperature ranging from -70^{o}C to 125^{o}C.

The pressure profile during the test is shown in fig. 4.8.

The PMTs and the electronic cards were switched on, for all the cycles, during the phases of maximum (45^{o}C) and minimum (-30^{o}C) operative temperature (see fig. 4.5), to perform the functional tests. The DALLAS temperature sensors were constantly acquired in order to check the effective temperatures of the PMTs and SFEC cards. In fig. 4.9 are shown the temperatures read from the flight sensors, and the PMT currents for all the phases of the functional tests. The values of the current depend on the voltage setted and on the number of PMTs supplied by each HV channel.

4.2.1 Analysis of the functional tests during the TVT

The offline analysis was performed selecting the data above a certain threshold on the charge spectra of the anodes sum, in order to remove the pedestal signal. This cut allows also to distinguish the dynode signal from its pedestal (see fig 4.10). Moreover only events of cosmic rays with multiplicity equal to 1 (only one

Figure 4.6: The Lower TOF trasport at Terni for the thermal vacuum and vibration tests.

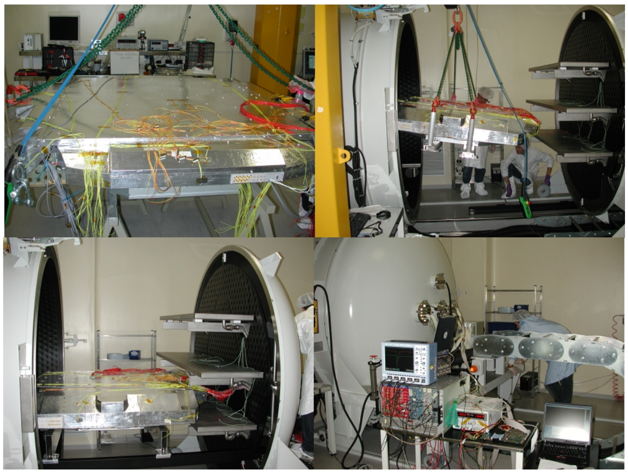

Figure 4.7: The LTOF prepared for the test and inserted into the vacuum chamber.

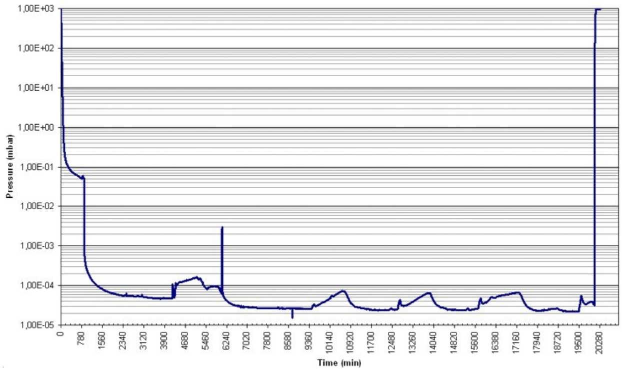

Figure 4.8: Thermal vacuum test: pressure profile.

counter hit) were considered, in order to have a cleaner sample of data. The trigger with the central counters (305 or 405) allowed to select cosmic rays crossing the center of the analysed counters.

The response of each counter at various temperature is plotted in fig. 4.11 and in fig. 4.12, for plane 3 and 4 respectively. The fitted peak values of the charge spectra from the anode signals are shown. Except for the counter 309 side N that showed a strange behaviour at -30^{o}C, all the counters show a peak decreasing

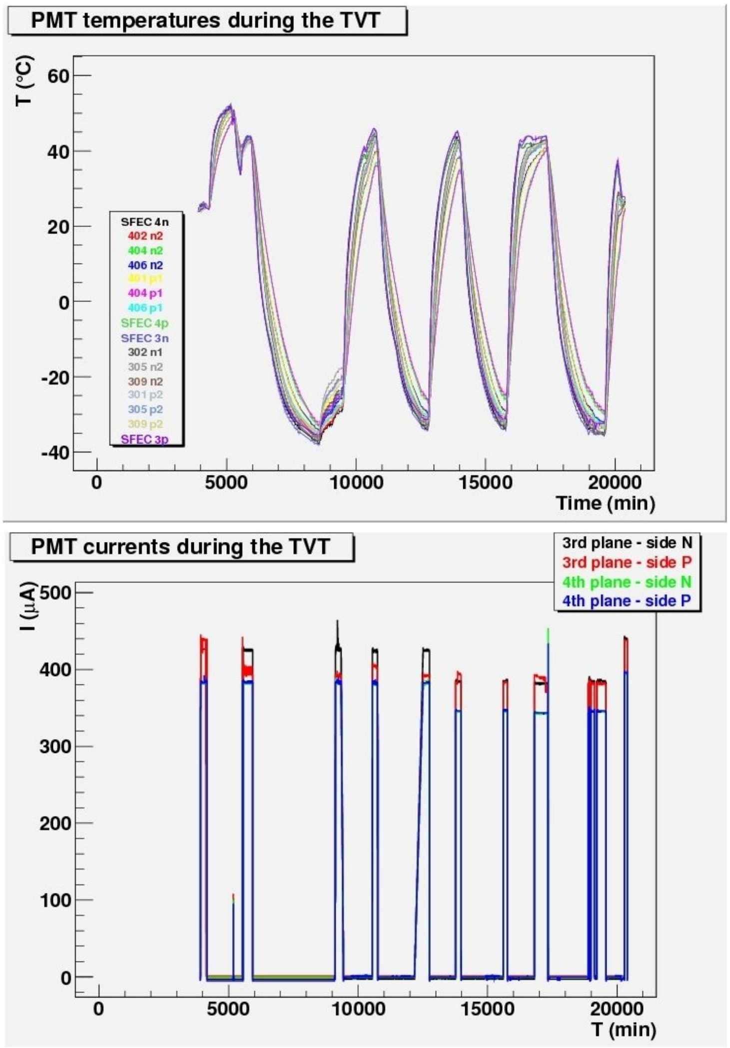

Figure 4.9: Thermal vacuum test: temperatures read out by the Dallas flight sensors (above). PMTs currents monitored through the power supply channels (below).

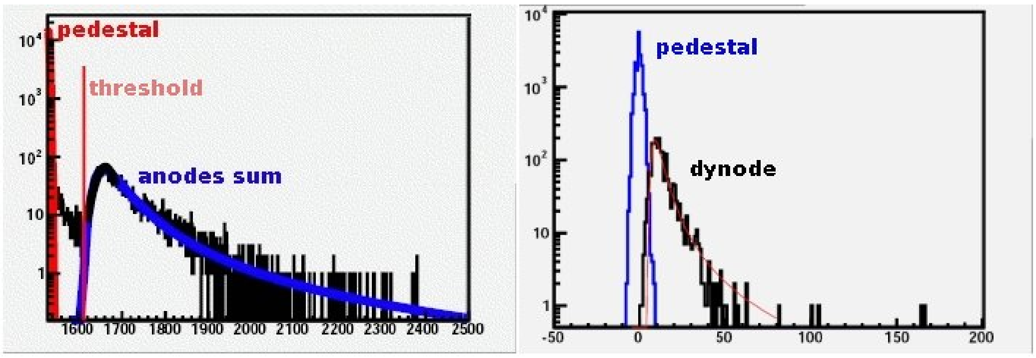

Figure 4.10: To select the data it was used a threshold in the spectrum of the anodes sum (left). This cut allowed to separate the pedestal from the dynode signal (right).

with the temperature, as expected. One can't compare the peaks of two different counters, because for practical reasons the PMTs voltages were fixed (having only 4 channels of power supply), and did not correspond to the equalization voltages.

In fig. 4.13 the mean values of the charge peaks of the same side of the counters are shown, as a function of the temperature. The trend seems to confirm a previous measure performed in the Bologna space simulator for a test counter. The variation of the response of the PMT anodes as a function of the temperature shows a reduction of about $0.4\%/^{o}C$.

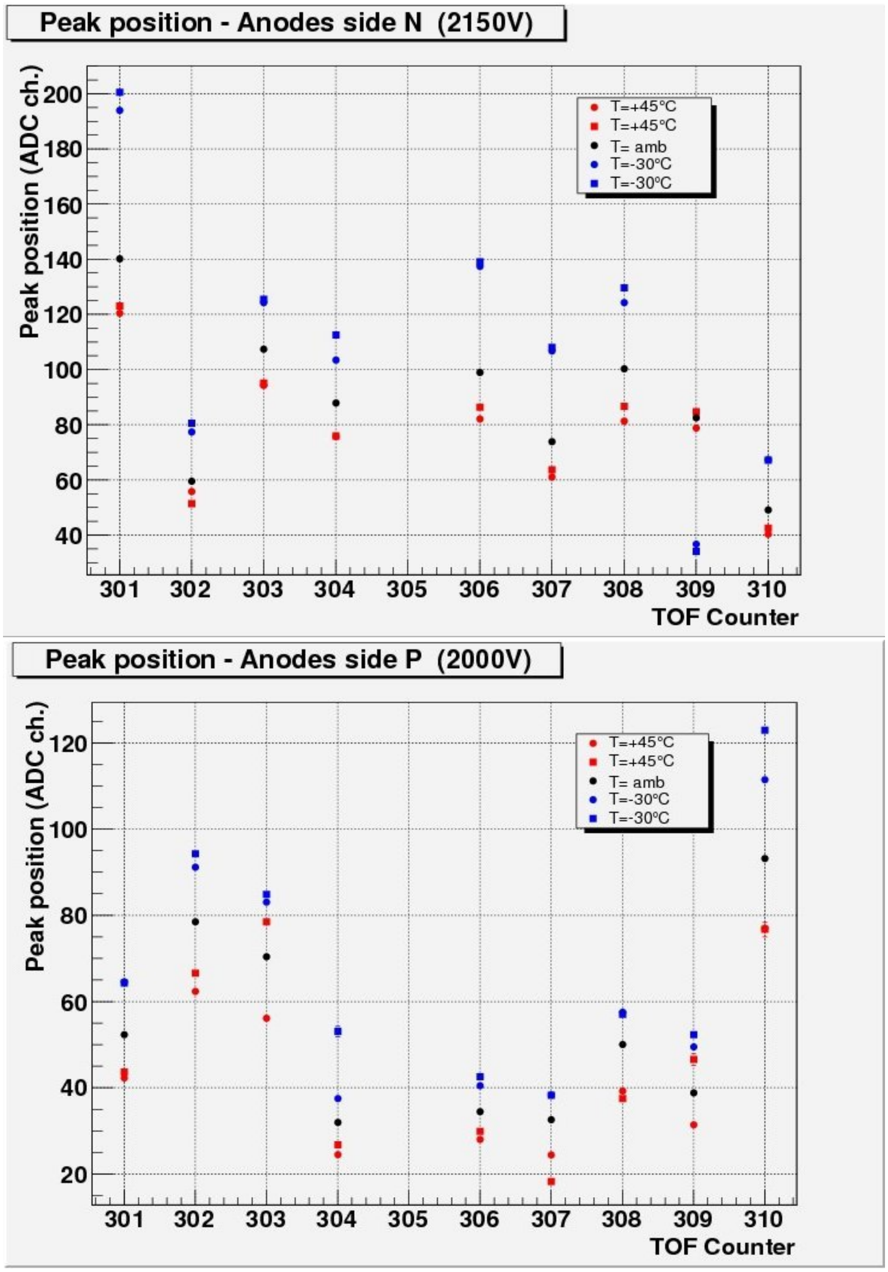

Figure 4.11: Peaks of the anodes charge spectra at various temperatures (plane 3, side N and P).

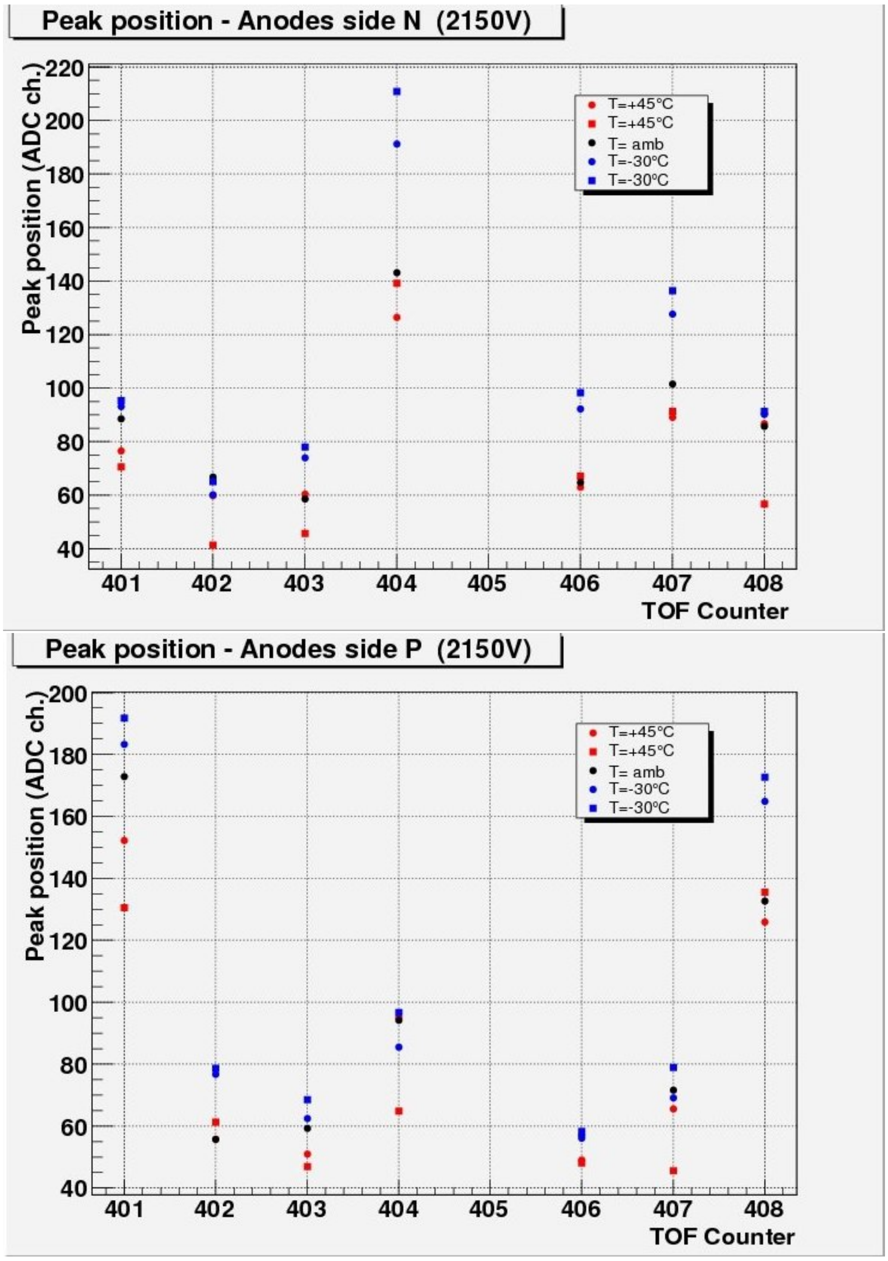

Figure 4.12: Peaks of the anodes charge spectra at various temperatures (plane 4, side N and P).

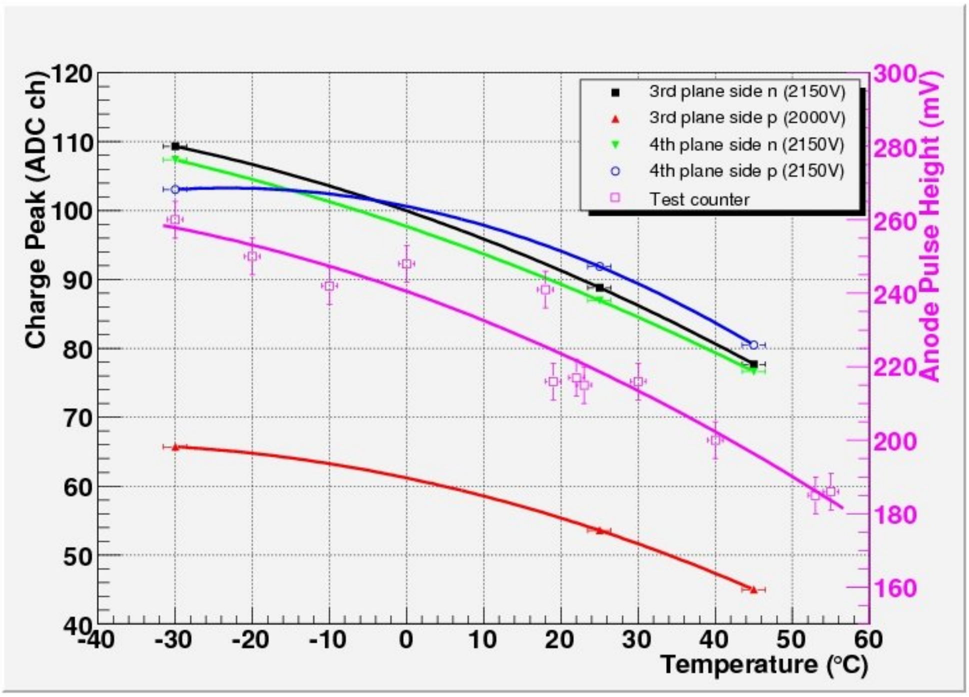

Figure 4.13: Means of the charge peaks of the anodes spectra as a function of the temperature. It is possible to compare the variation of the anode response for the LTOF counters with a measure performed on a test counter in the Bologna space simulator.

4.3 The LTOF vibration test

A vibration test of the flight model of the LTOF was performed[28], in October 2006, at the SERMS facility, in order to verify that:

- the LTOF first mode frequency was higher than 50Hz;
- the LTOF performances were not degraded by the Maximum Expected Flight Level vibration environment.

The vibration test was executed on the LTOF together with a RICH Aerogel container, installed under the LTOF. The test was performed along the three axes

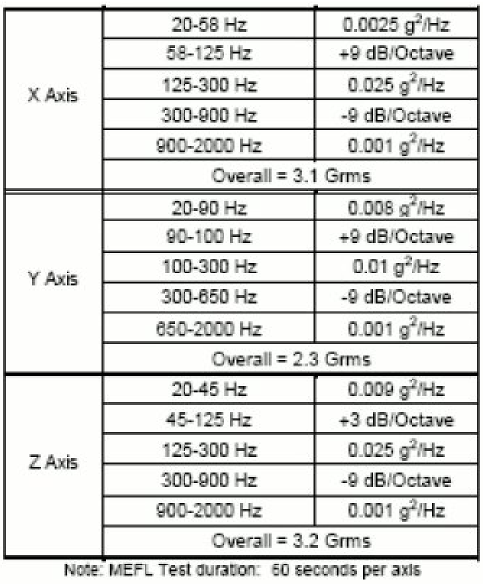

X Axis	20-58 Hz	0.0025 g^2/Hz
	58-125 Hz	+9 dB/Octave
	125-300 Hz	0.025 g^2/Hz
	300-900 Hz	-9 dB/Octave
	900-2000 Hz	0.001 g^2/Hz
	Overall = 3.1 Grms	
Y Axis	20-90 Hz	0.008 g^2/Hz
	90-100 Hz	+9 dB/Octave
	100-300 Hz	0.01 g^2/Hz
	300-650 Hz	-9 dB/Octave
	650-2000 Hz	0.001 g^2/Hz
	Overall = 2.3 Grms	
Z Axis	20-45 Hz	0.009 g^2/Hz
	45-125 Hz	+3 dB/Octave
	125-300 Hz	0.025 g^2/Hz
	300-900 Hz	-9 dB/Octave
	900-2000 Hz	0.001 g^2/Hz
	Overall = 3.2 Grms	

Note: MEFL Test duration: 60 seconds per axis

Figure 4.14: Maximum Expected Flight Level for AMS-02.

(X, Y and Z), executed with the Maximum Expected Flight Level (MEFL) specifications as expected by the document JSC 28792 - August, 2003 Rev.C "Alpha Magnetic Spectrometer - 02 Structural Verification Plan for the Space Transportation System and the International Space Station" (see table in fig. 4.14).

The test was executed with a shaker, a sliding table and two dedicated fixtures, different for the Z axis and for the X,Y directions (see fig. 4.15, 4.16 and 4.17). The LTOF was installed on the fixture through the supporting rods, which length was adjusted to optimize the alignement. The rods were tensioned to the design values and instrumented with strain gauges, to measure their deformations.

To monitor the test, accelerometers type KS94.100/KS95.100 were used for control and KS94/KS95 for measure. These sensors are able to guarantee an accurate measurement in the range 5-2000 Hz. The accelerometers were positioned: 8 externally on the interface of the LTOF with the fixture, 7 internally on the PMTs, and 21 externally on the LTOF structure, walls and Aerogel container.

First a search of the resonance frequencies of the fixture was performed, using the following level (sine input):

- linear frequency scan band: 5-2000 Hz;
- scan speed: 2oct/min (sweep up only);

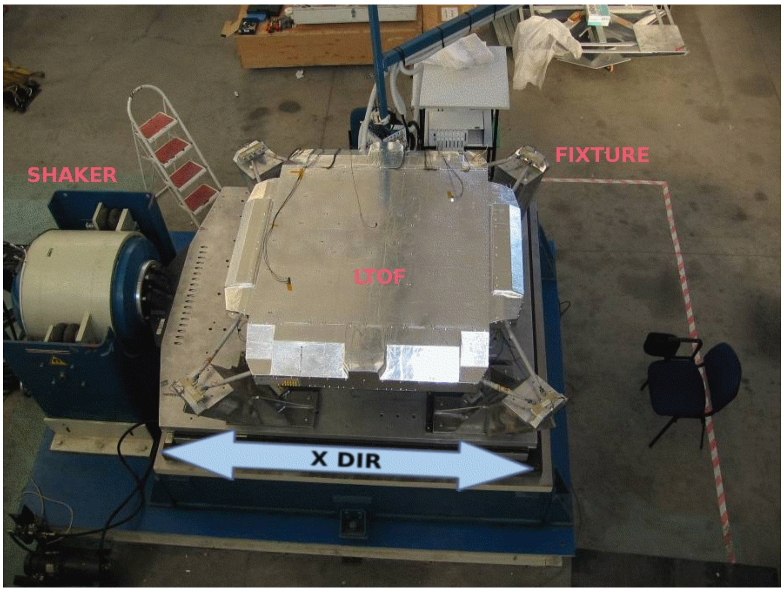

Figure 4.15: Setup for the vibration test along the X axis.

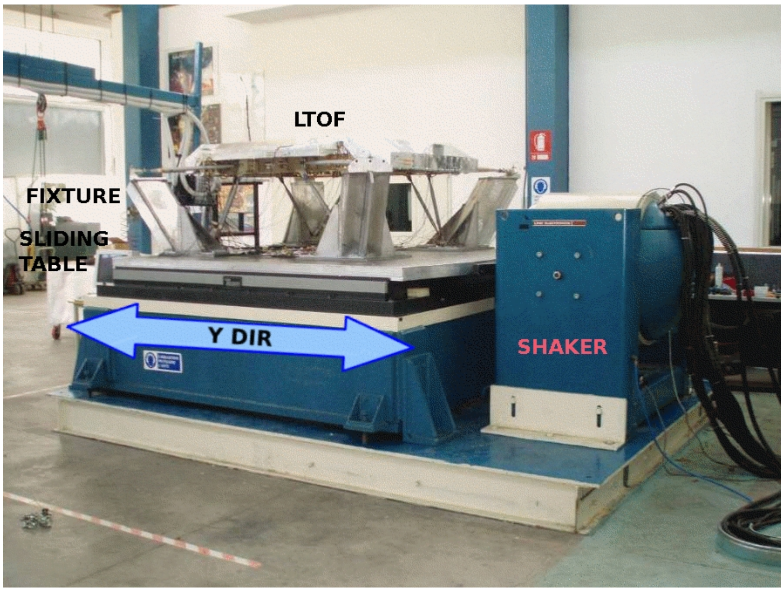

Figure 4.16: Setup for the vibration test along the Y axis.

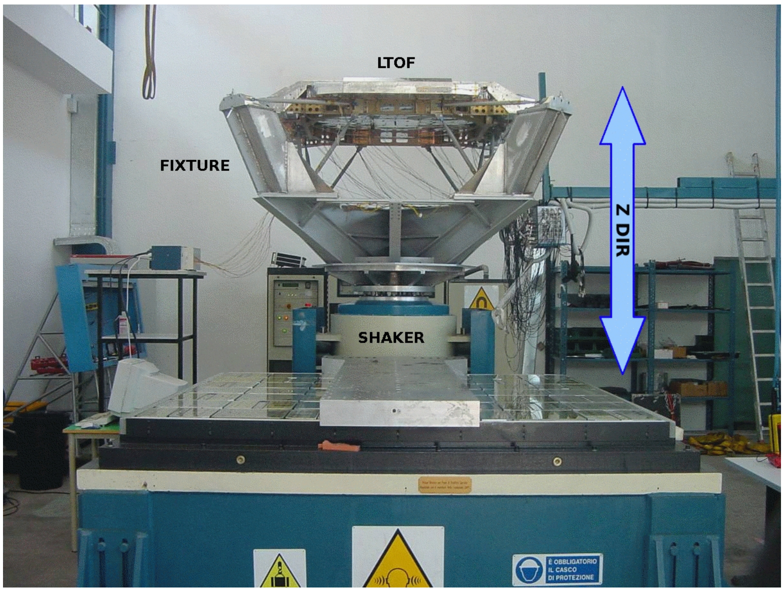

Figure 4.17: Setup for the vibration test along the Z axis.

- level: 0.3 g (peak);
- control: multipoint input control.

The test of the LTOF was performed following the MEFL random spectrum, verifying from the plot the absence of structure degradation and the mechanical stability of small components. The random vibration was performed starting with a low level (-9 dB) and approaching gradually (-6dB, -3dB) the full level (0 dB). Before and after the vibrations a resonance search was executed, verifying from the plots that no frequency shifts occurred. For Z direction also a resonance search with random noise was executed to investigate the behaviour in the complete frequency range (20-2000 Hz).

4.3.1 Vibration test results

The results of the LTOF vibration test allowed to successfully verify all the test objectives, in fact:

- the LTOF first mode is F1=70 Hz for X direction;

- the LTOF first mode is F1=70 Hz for Y direction;
- the LTOF first mode is F1=65 Hz for Z direction;
- the test was succesfully performed using MEFL specifications with no discrepancy between resonance search before and after the random vibration, no deformation, damage or loose parts detected during visual inspections.

The maximum recorded level on the structure was 2.2 gRMS (Z direction), on the PMTs was 5.4 gRMS (Z direction), and the overall level measured on test was 12 gRMS (Z directionon) on NaF tiles of the RICH.

In the fig. 4.18, 4.19 and 4.20 the plots show the mode frequency identification at the applied random level and the comparison of resonances before and after the full levels random vibrations.

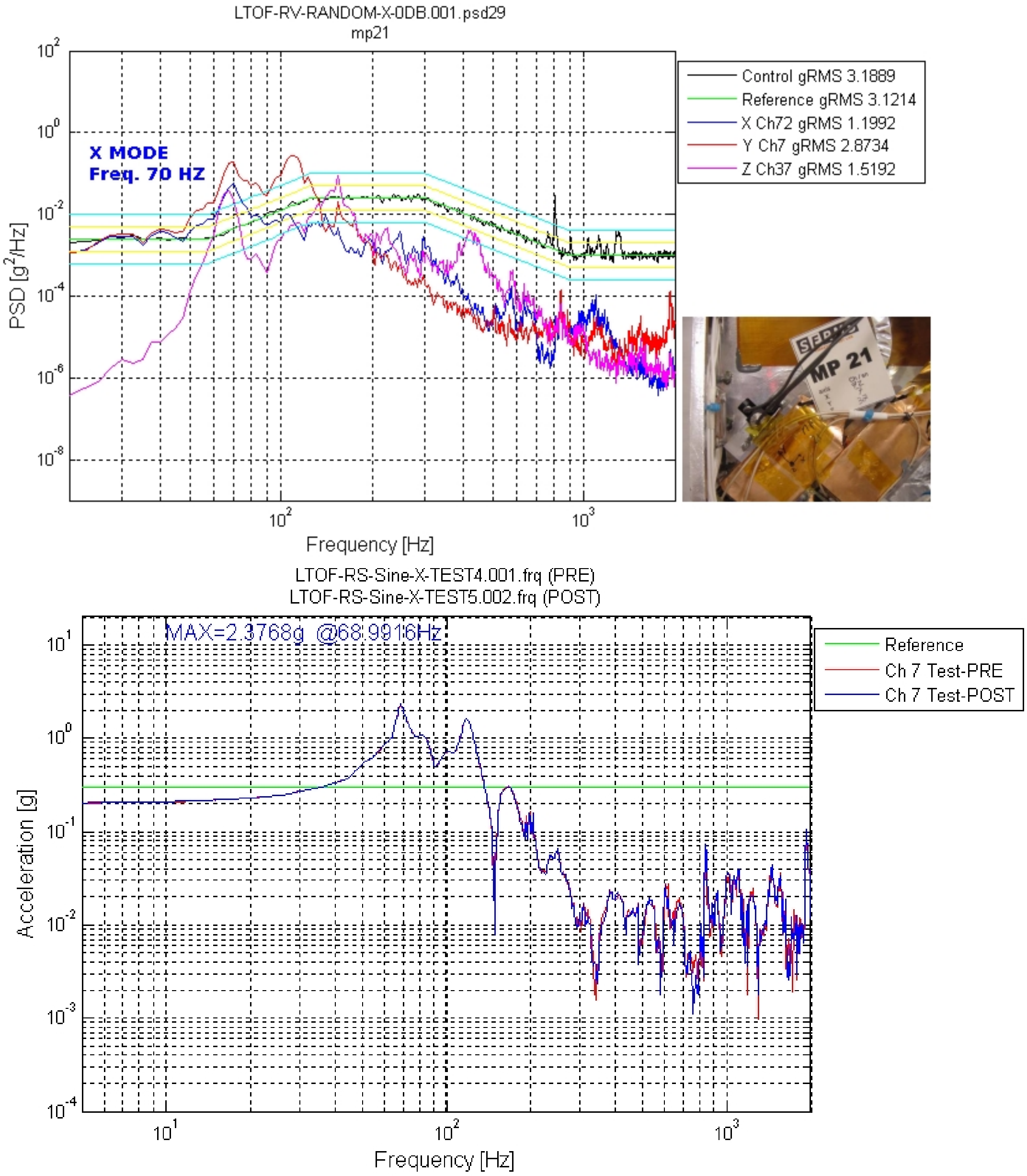

Figure 4.18: Results of the vibration test along the X axis: the first mode is at 70 Hz (above) and no discrepancy is shown in the plots before and after the test (below).

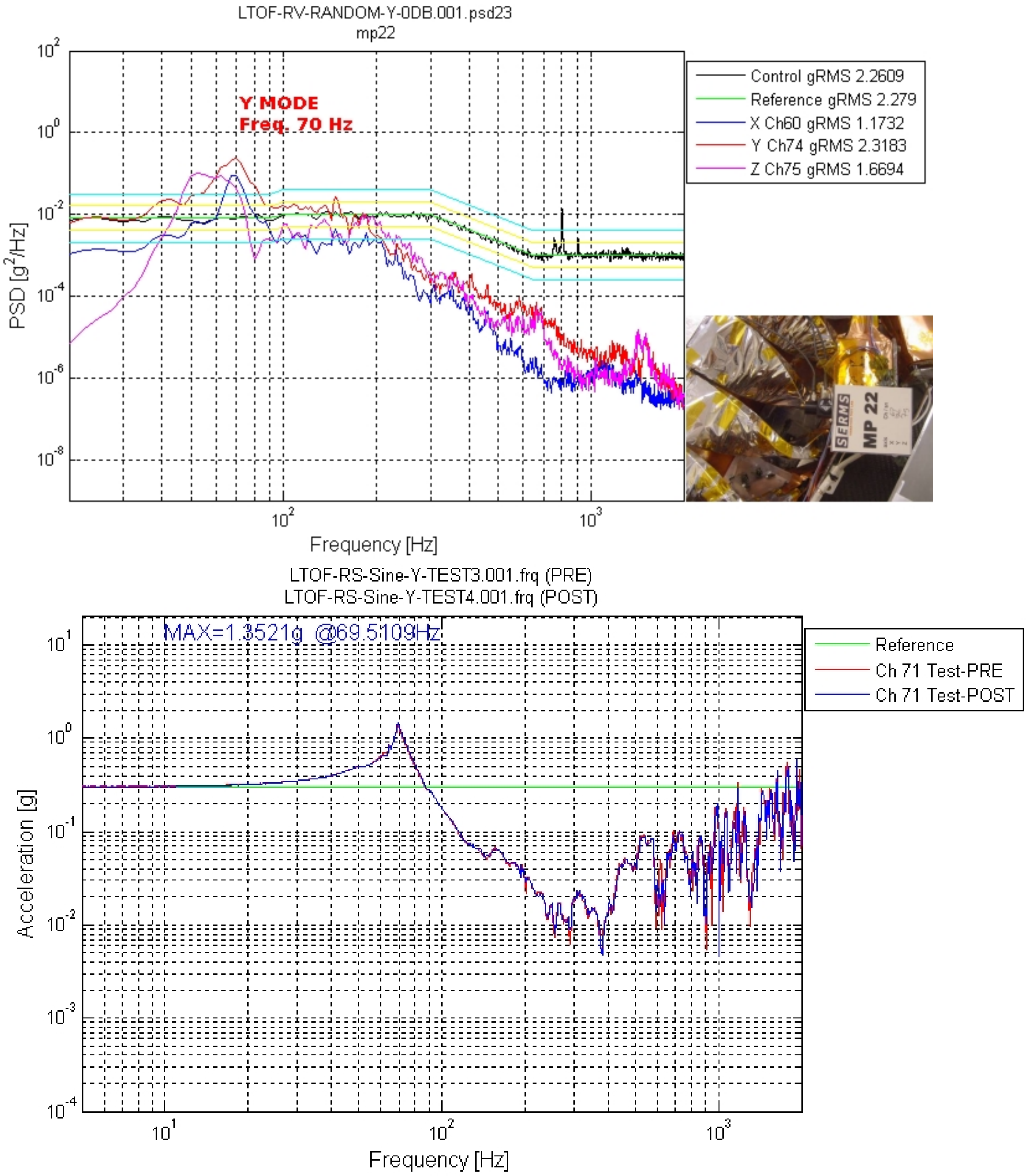

Figure 4.19: Results of the vibration test along the Y axis: the first mode is at 70 Hz (above) and no discrepancy is shown in the plots before and after the test (below).

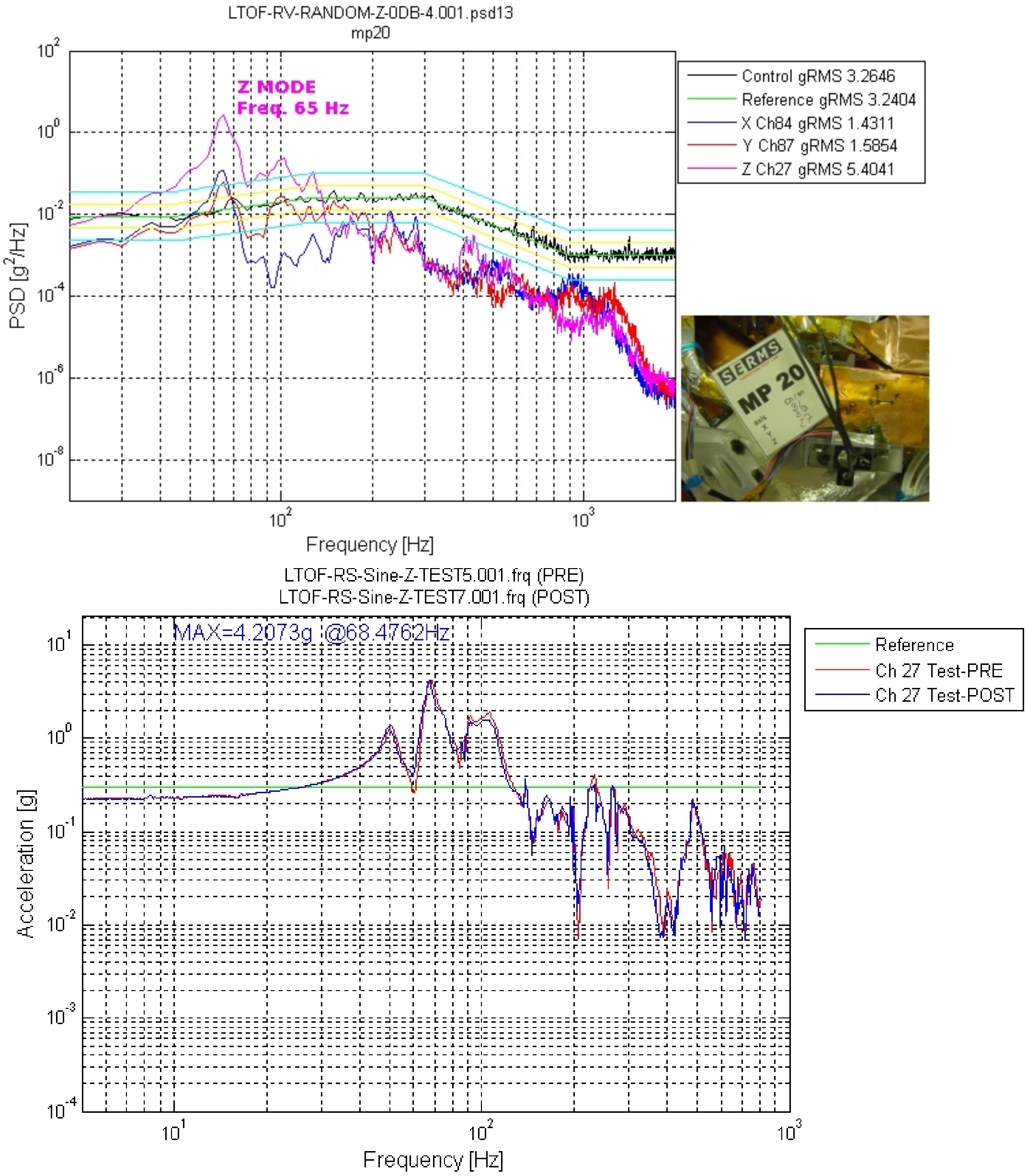

Figure 4.20: Results of the vibration test along the Z axis: the first mode is at 65 Hz (above) and no discrepancy is shown in the plots before and after the test (below).

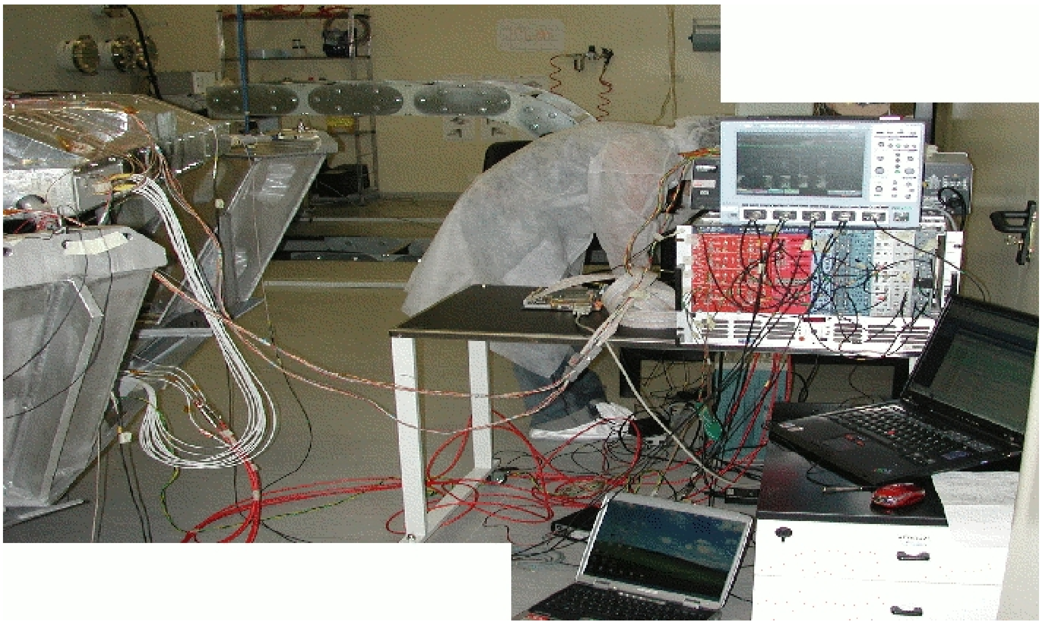

Figure 4.21: Functional test after the random vibration.

4.3.2 Analysis of the functional tests after the vibration test

The functional tests have been performed, one after the random vibration along the Z axis and one after the random vibration along the X,Y axes (see fig. 4.21). The voltages were fixed at 2150V for all the PMTs of the Lower TOF.

The functional tests were executed in the clean room during the preparation of the vibrating table. The comparison between the different functional tests performed before, during and after the space qualification tests, at ambient temperature, is summarized in fig. 4.22 and fig. 4.23.

The plots show that the responses of the PMTs are greater in the functional test performed after the TVT. This is due to a setting of the PMTs voltages greater than 2150V. The peak of the counter 310 side P is greater during all the TVT, while the 307 side P has a lower peak during the TVT in vacuum at ambient temperature. The PMTs of the counters 402 and 408 side N, 401 and 404 side P shows lower peaks after the vibration tests. Gain variations were known by previous vibration tests performed on single PMTs[29].

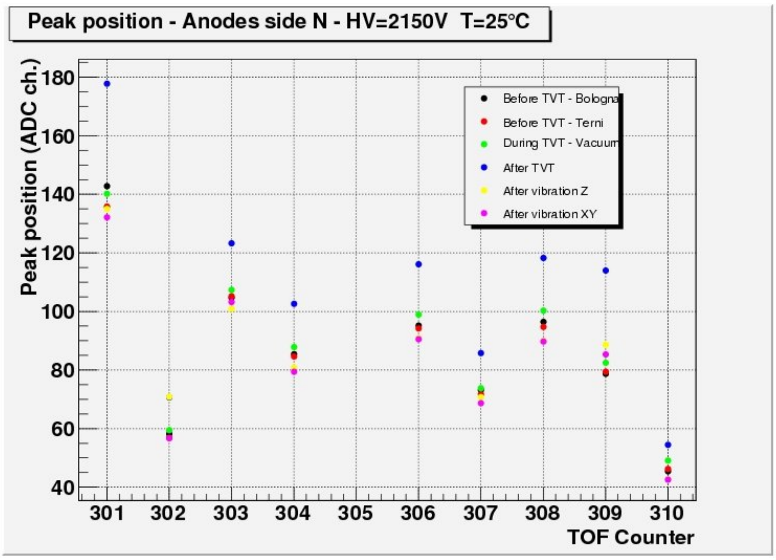

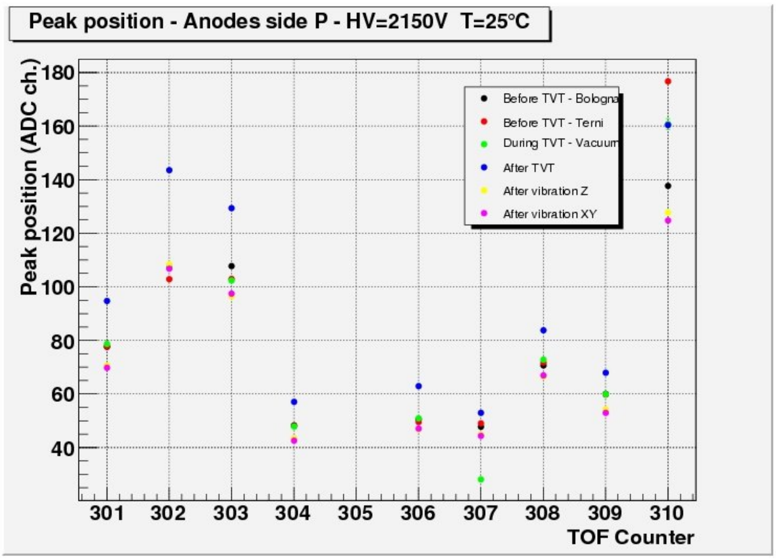

Figure 4.22: Comparison between all the functional tests performed at ambient temperature for plane 3.

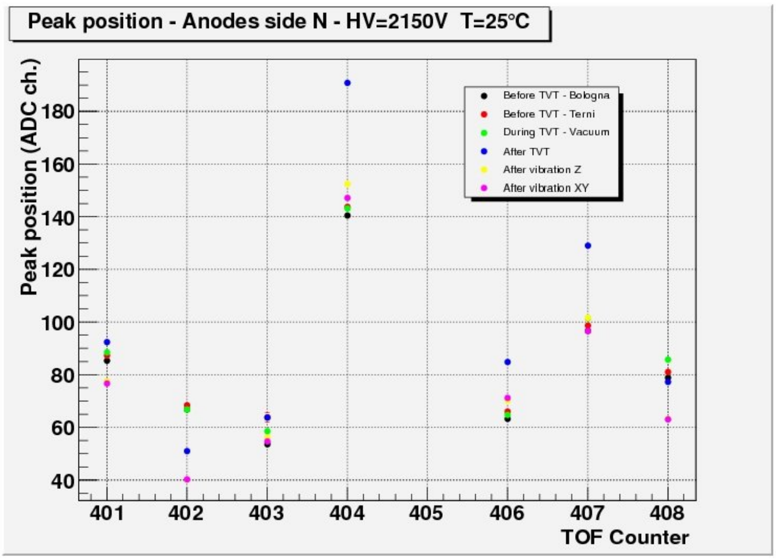

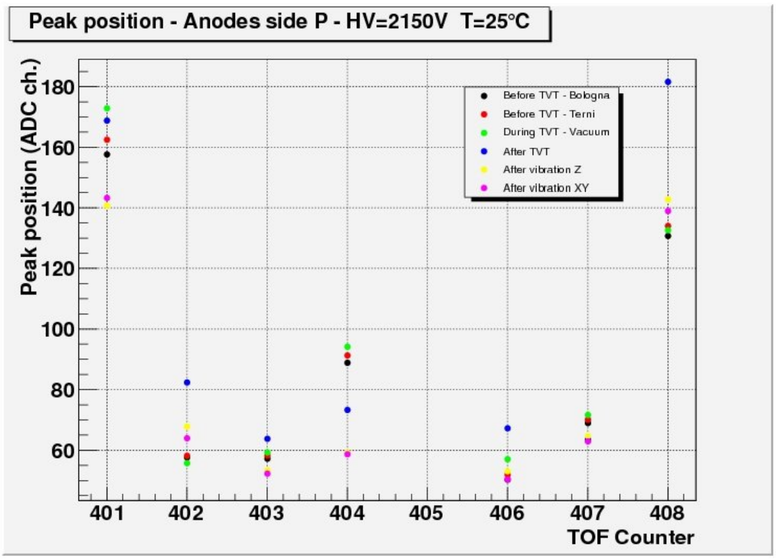

Figure 4.23: Comparison between all the functional tests performed at ambient temperature for plane 4.

Chapter 5

The Silicon Photomultipliers

The new photodetector Silicon Photomultiplier (SiPM) promises to meet the needs of a space particle physics experiment like AMS: low weight, low consumption, constant performance for a long time, insensitivity to magnetic fields and gain up to 10^6. I studied this detector in laboratory, by means of the same characterization methods adopted to calibrate the PMTs of the TOF. Moreover I programmed a software[1] which allows to simulate the response of the SiPM to light [30]. I am a member of the DASiPM collaboration[2] which wants to study the use of the SiPM detector for Medical Physics and Space applications.

5.1 Characteristics of a SiPM

A SiPM [31][32][33] is an array of Avalanche Photodiodes (APD) joined together on common substrate and working on common load. The operational bias voltage is 10-15% higher then the breakdown voltage, so each APD pixel operates in Geiger mode, limited by individual resitor with a gain (about 10^6) determined by the charge accumulated in its capacitance. The pixel works as digital device, but SiPM in whole is an analogue detector which can measure light intensity. The number of pixels is about 10^3 mm^{-2} and determines the SiPM dynamic range. Due to a small depletion region ($\sim 2\mu$m) and high operating electric field ($3 \cdot 10^5$ V cm^{-1}), with high carrier velocity (10^7 cm s^{-1}) the Geiger discharge is extremely short and the SiPM signal is very fast. Such interesting features suggest that this photodetector can be a possible substitute for the usual photomultiplier.

---

[1] In Appendix A the SiPM simulation code.

[2] Development and Application of Silicon PhotoMultipliers - http://sipm.itc.it

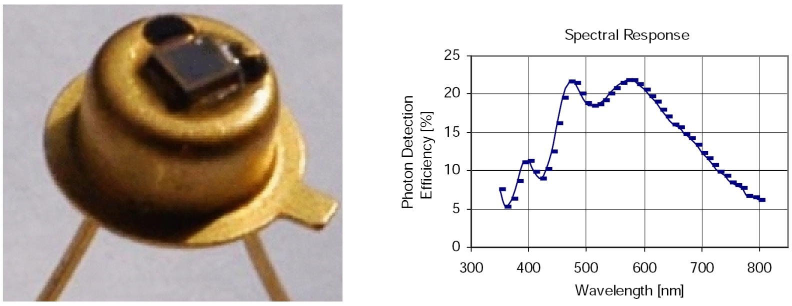

Figure 5.1: The Silicon Photomultiplier (left) and its spectral response (right).

I tested a sample of SiPMs (see fig. 5.1) by the Photonique company[3], with an operating voltage of about 60V and a peak sensitivity wavelength at 470 nm, where the single photon detection efficiency is about 20%. The signal rise time is less then 2 ns and the operating temperature range is between -40^{o}C and 40^{o}C[4]. This devices are not very suitable to be coupled with the AMS plastic scintillators whose wavelength of maximum emission is 425 nm, so the DaSIPM collaboration developed a new device with characteristics more suitables to our purposes.

5.2 A model for the simulation

The SiPM can be modeled as an array of on/off pixel detectors, each one, when fired by a photon, responds with a certain efficiency ε, and produces a signal whose charge depends on the gain. In the MonteCarlo simulation I used a square matrix of 25 x 25 pixels each one producing a charge Gaussian distribution with mean and standard deviation calibrated by the data distribution.

The number of light photons, impinging on the SiPM active area, is extracted by a Poisson law whose mean is in agreement with the light flux one wishes to simulate. Adjusting this mean value it is possible to simulate the SiPM response to the single and many photoelectrons regime. The response of the SiPM to the light is the sum of the responses of each single pixel.

In the simulation it is considered also the optical cross-talk: each pixel hit by a photon can produce a cross-talk signal in a contiguous pixel with a certain probability. This effect is due to the production of photons when a breakdown

---

[3] www.photonique.ch

[4] Characteristics from the Photonique datasheet.

avalanche occurs[34]. The number of pixels and the probability of the cross-talk effect can be obtained by the dark counts spectra (see fig. 5.11). For this effect I consider also a saturation: an emitted photon arriving on a pixel already hit will not induce cross-talk, so the cross-talk probability $P_{j,N}$ on j pixels, decreases with the number of hit pixels N, according to the relation [35]:

$$P_{j,N} = \sum_{i \geq j} \binom{i}{j} P_{i,0} \left(1 - \frac{N-1}{N_{max}-1}\right) \left(\frac{N-1}{N_{max}-1}\right)^{i-j} \tag{5.1}$$

where N_{max}=625 is the total number of SiPM pixels. In fig. 5.2 is shown the cross-talk probability as a function of the hit pixels.

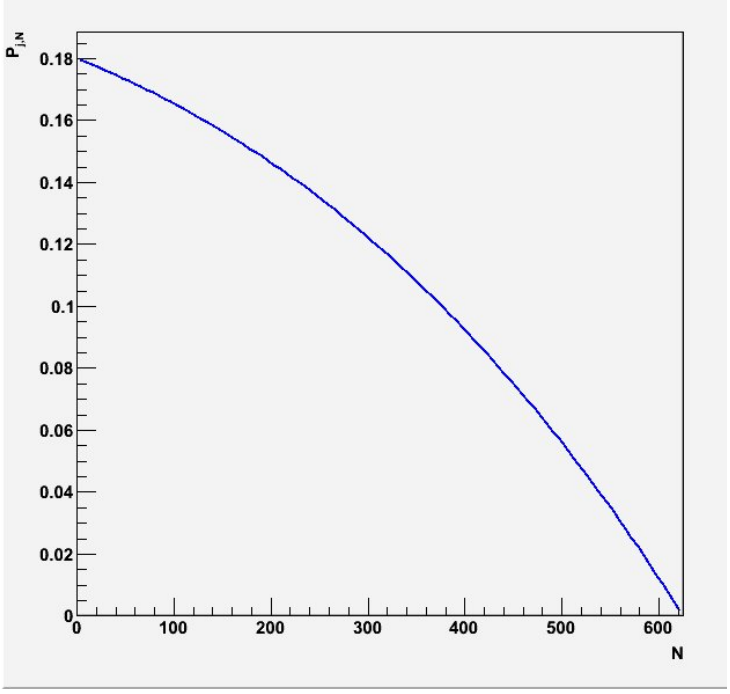

Figure 5.2: Cross-talk probability depending on the number of hit pixels.

I also simulate the SiPM dark counts with a certain probability that one pixel can produce a signal, indipendently from the light impinging on the SiPM active area. This probability is taken from the data distribution. In figure 5.3 it is shown a screenshot of the oscilloscope where one can see the dark count signals: it is possible to distinguish the number of hit pixels; the smallest pulses represent

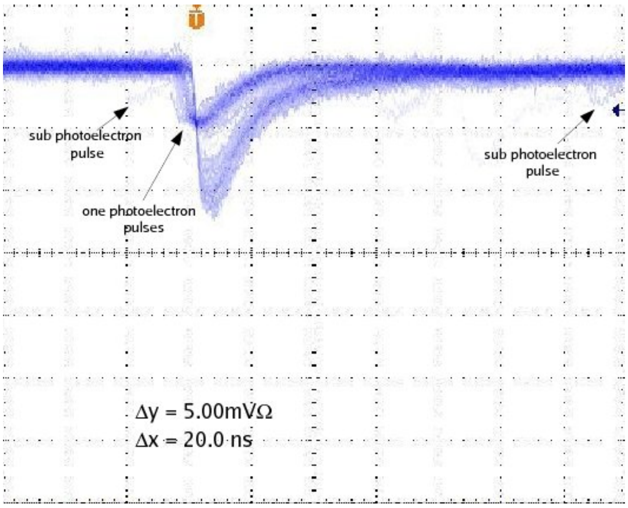

Figure 5.3: SiPM dark pulses from the oscilloscope. The smallest ones correspond to the sub-photoelectron signals.

pixels which respond with a gain lower than the main gain due to a photon (sub-photoelctron pulses). In the simulation, a probability for these sub-photoelectron pulses with a lower gain is implemented. These pulses add some counts between the pedestal and the first peak, influencing also the width of the other peaks.

5.3 The SiPM calibration

For the SiPM calibration it is used the electronic setup of the Bologna laboratory designed for the PMTs of the Time Of Flight, consisting of a dark box with a light emitting diode (LED) inside (see fig 5.4). The SiPM, placed inside the box, was read out by an electronic board furnished by the Photonique company, which inverts and amplifies the signal by a factor of ∼20 (see fig. 5.5). The LED driver module allows to adjust the light intensity, in order to have few or many photons. The frequency of the LED pulses was controlled by two time units. The SiPM signal (amplified) was integrated by a Charge Integrating ADC controlled by the STATUS A module. This setup allows to have the response of the SiPM to few photons (single photoelectron spectrum) and the response to many photons, to be able to measure the SiPM gain with two different tecniques. Moreover, it is also possible to have the SiPM dark counts spectrum.

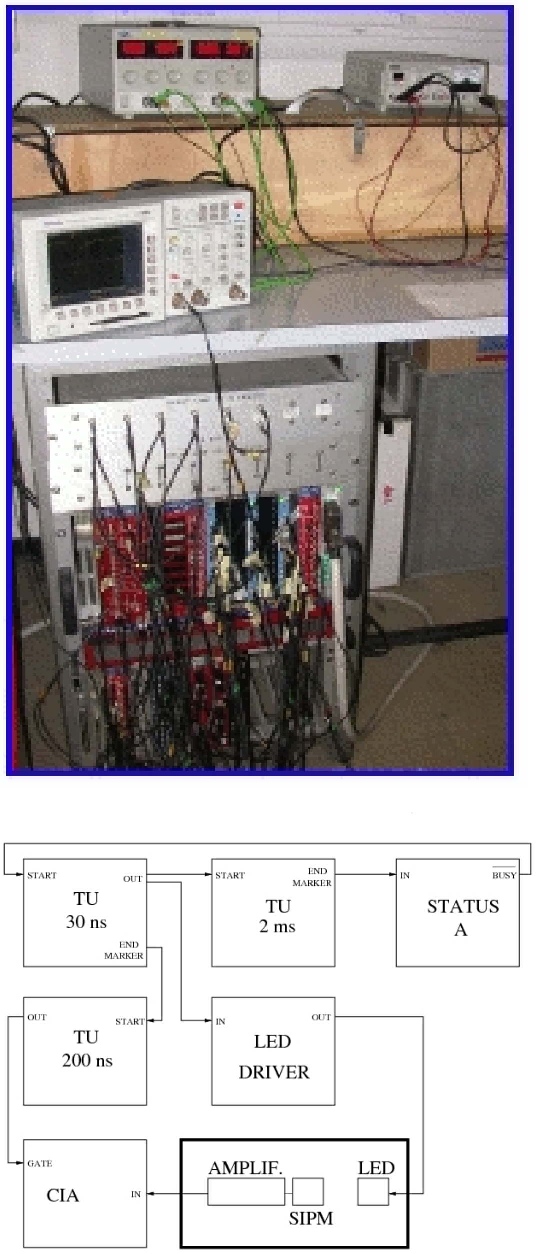

Figure 5.4: Electronic setup used for the SiPM calibration.

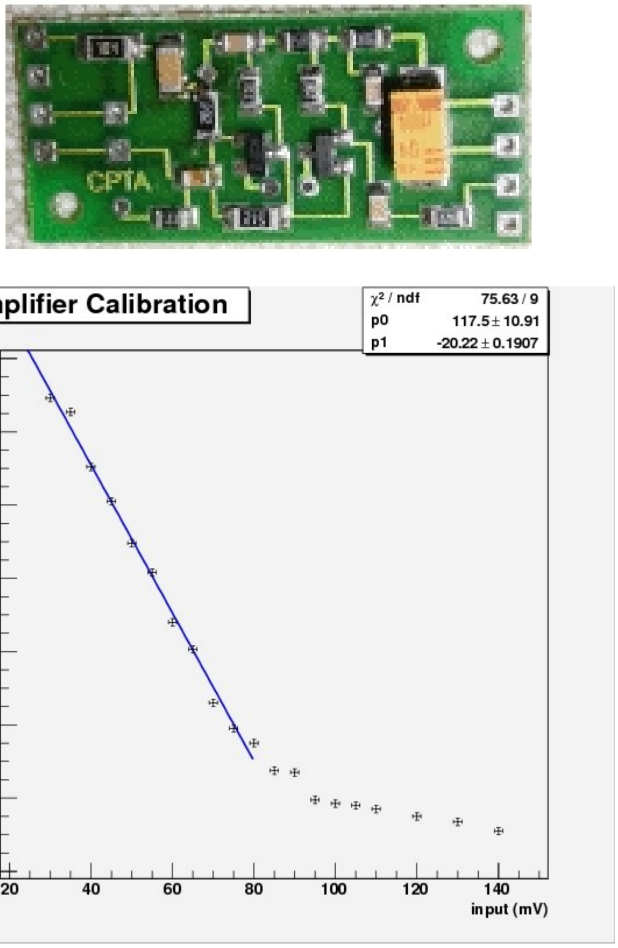

Figure 5.5: Electronic board used to read-out and to amplify the SiPM sigmal (above). Amplifier calibration: the gain factor is about 20; for input pulses with heigth greater then 80 mV it is shown a saturation (below).

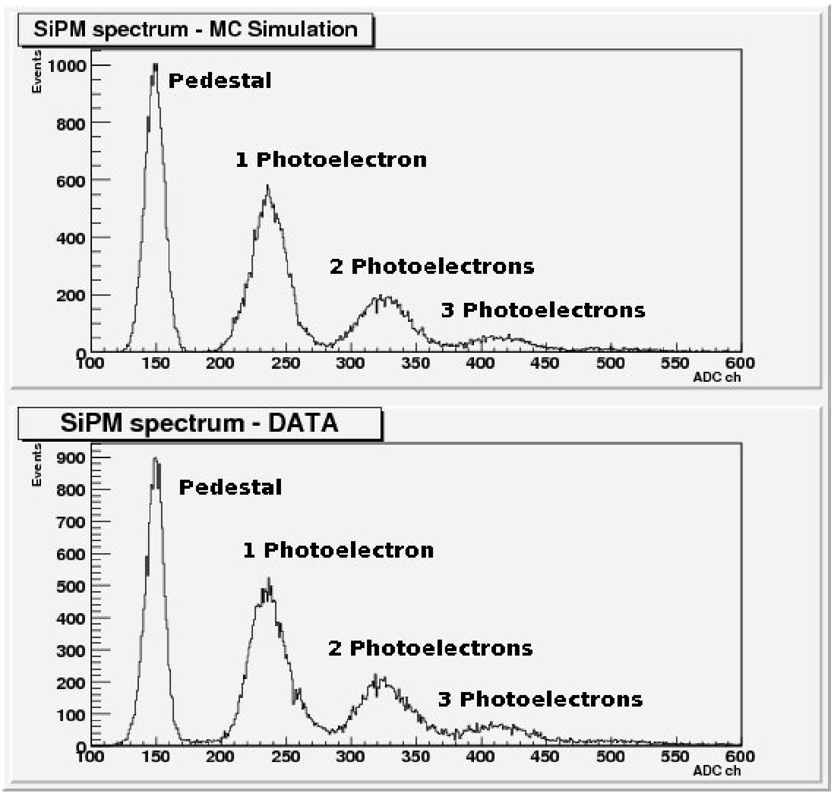

Figure 5.6: SiPM single photoelectron spectra obtained from the simulation (above) and from the data (below). The good single photoelectron resolution allows to distinguish the peaks corresponding to each photoelectron.

5.3.1 Single photoelectron response

The single photoelectron spectrum is obtained illuminating the SiPM with a faint LED light intensity, in order to have only few photons impinging on the active area of the photodetector. In figure 5.6 are shown the two spectra obtained from the data and from the MC simulation. The first peak corresponds to the pedestal and the other peaks to each photon. It is possible to distinguish the peaks, because the SiPM has a good single photoelectron resolution, defined by [24]:

$$\delta = \frac{\sigma}{A}. \tag{5.2}$$

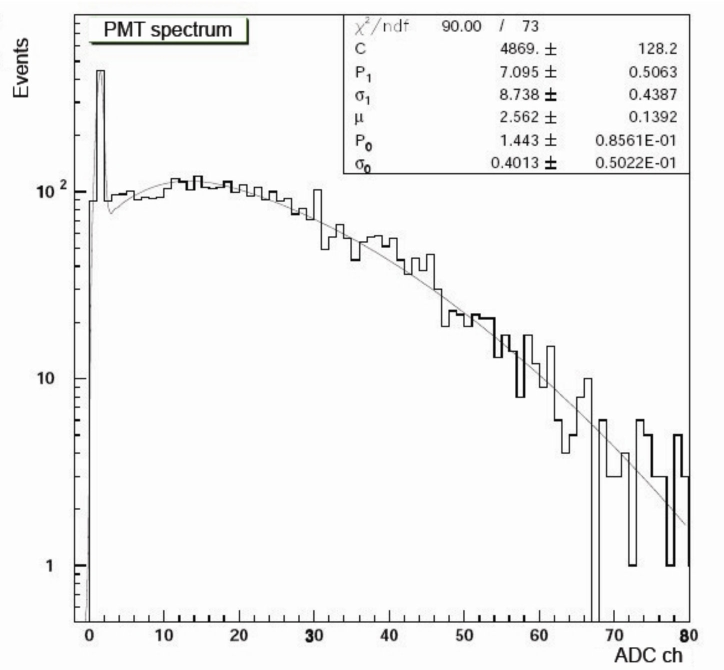

Figure 5.7: Single photoelectron spectrum of a TOF photomultiplier. The fit function is a proper convolution of Gaussian distributions.

where A represents the distance between the second peak (1 photoelectron) and the first peak (pedestal), while σ represents the standard deviation of the peak corresponding to 1 photoelectron. In fig. 5.7 is shown the single photoelectron spectrum of a TOF photomultiplier. Due to the worse single photoelectron resolution, it is not possible to distinguish the various peaks of the spectrum and it has to be used a fit function obtained by a convolution of Gaussian distributions[36].

The SiPM gain can be directly determined by the distance of two adjacent peaks of the spectrum:

$$G = \frac{A \cdot s}{G_{el} \cdot e} \tag{5.3}$$

where G is the gain, A the distance of two contiguous peaks, s the scale factor of the ADC (s = 0.033 pC/channel for the high resolution scale and s = 0.25 pC/channel for the low resolution scale), G_{el} the amplifier gain and e the electron charge. The high resolution scale of the ADC is used for the single photoelectron spectra, while the low resolution scale for the many photoelectron spectra.

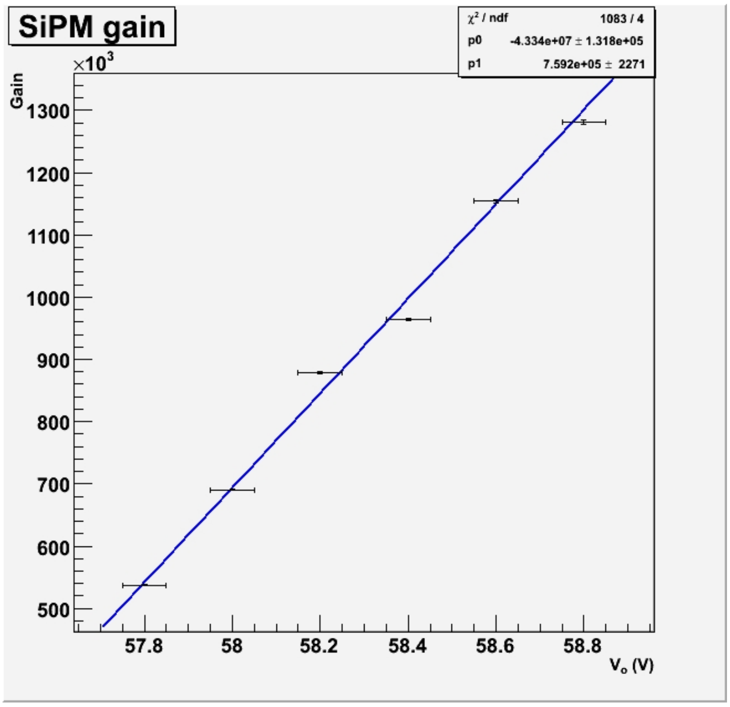

Figure 5.8: Linearity of the SiPM gain as a function of the operating voltage.

In fig. 5.8 is shown the gain of the SiPM measured at various operating voltages. The plot shows the linearity of the gain as a function of the voltage; from the parameters of the linear fit one can obtain the capacitance of the single pixel and the breakdown voltage of the SiPM. In fact, the single pixel signal is determined by the total charge Q_p collected during the Geiger discharge of the single pixel capacitor C_p:

$$G = \frac{Q_p}{e} = C_p \cdot \frac{V_o - V_{break}}{e} \tag{5.4}$$

where G is the gain, V_o the operating voltage, V_{break} the breakdown voltage and e the electron charge. From the fit it results that C_p is about 120 fF and the breakdown voltage is V_{break} = 57.0 V.

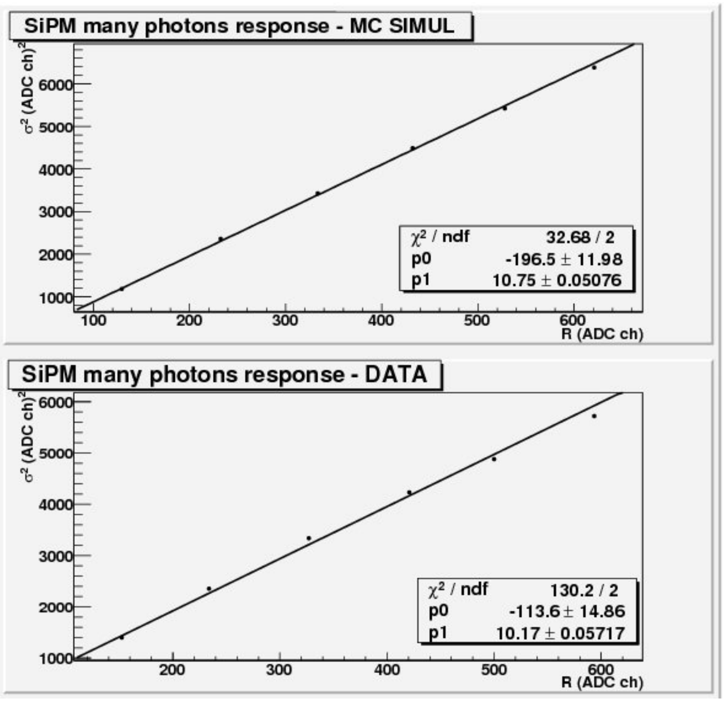

Figure 5.9: SiPM response line to many photons for different light intensities, at fixed voltage, obtained with the MonteCarlo simulation (above) and the data (below).

5.3.2 The many photons response

The response of the SiPM to many photons provides a second way to measure the photodetector gain. The integrated charge spectrum gives a Gaussian distribuition whose mean and σ^2 are correlated with the gain, like for a standard photomultiplier, according to the relation[24]:

$$R = G \cdot N_{phe} + P \tag{5.5}$$

where R is the measured average signal, P the pedestal, G the gain and N_{phe} the number of photoelectrons. The observed variance is:

$$\sigma_R^2 = G^2 \cdot N_{phe} + G^2 \cdot N_{phe} \cdot \delta^2 + \sigma_{el}^2 \tag{5.6}$$

where the first term is given by the statistical fluctuation of the light signal, the second term is given by the single photoelectron response and the last term is the

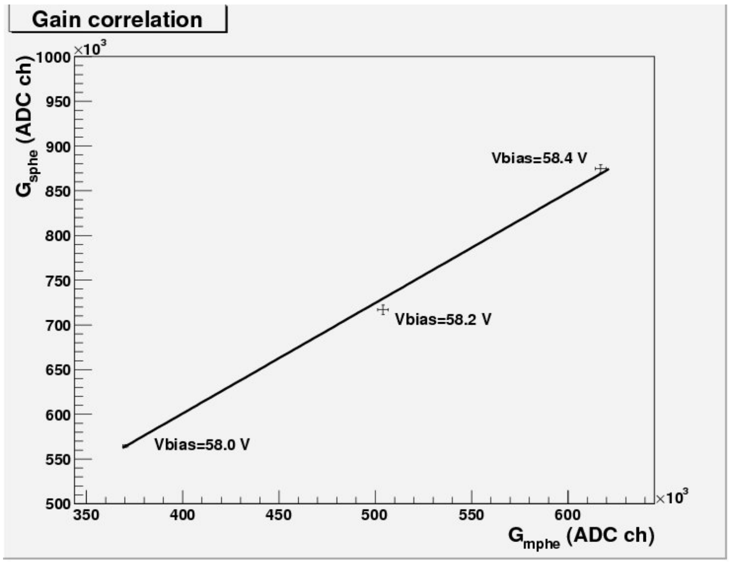

Figure 5.10: Comparison of the two methods used to obtain the SiPM gain.

combination of the detector, amplifier and ADC electronic noise.

In figure 5.9 are shown the plots of the response line (from the data and the MonteCarlo simulation), i.e. the σ^2 as a function of the mean R of the SiPM response in charge at various LDE light intensities, for a fixed operating voltage. The slope of the linear fit of the response line is proportional to the gain:

$$S = G(1 + \delta^2). \tag{5.7}$$

Also with this method it is possible to measure the mean gain of the photodetector. This tecnique was used to calibrate the TOF photomultipliers that have a bad single photoelectron resolution.

In fig. 5.10 is shown the comparison of the gain measured with the two methods: from the single photoelectron spectrum (G_{sphe}) and from the many photons response (G_{mphe}). From the plot it is evident that the gain values are correlated with a constant ratio equal to 1.5.

The technique of the many photoelectrons will be used in AMS-02 to calibrate the PMTs in flight, considering different cosmic rays that lose energy crossing the scintillator counters and producing different light intensity on the photodetector[23]. This is very important, because a PMTs recalibration could be necessary for a long duration experiment, and the gain variations could be controlled through the re-

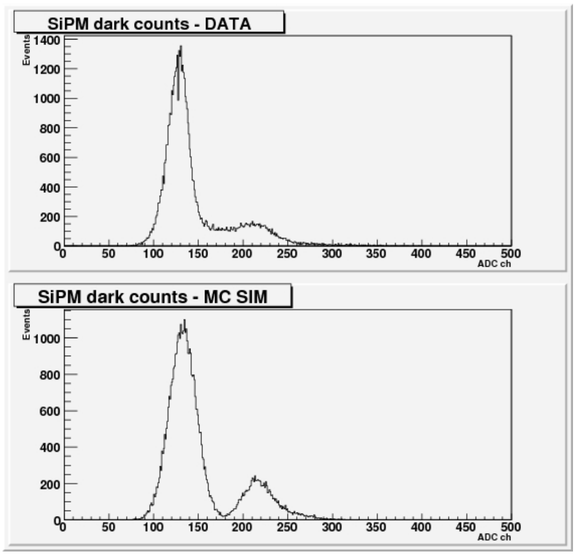

Figure 5.11: SiPM dark counts spectra at room temperature, from the data (above) and the MC simulation (below).

sponse line.

5.4 Dark rate

The dark rate represents the main contribution of the SiPM noise. The dark pulses are generated by the photodetector in absence of light (see fig. 5.11), due to the effects of high electric fields[37] and to the thermal creation of carriers. If these generated carriers reach the multiplication, they can cause an avalanche. The dark rate is proportional to the temperature, and limits the SiPM performance only in detection of very small light intensities.

I measured the dark rate of the SiPM for different operating voltages at room temperature (see fig. 5.12). The maximum frequency is 30 MHz, for higher voltages. The shape of the curves shows the transit between the various photoelectrons. Even if the frequency is very high, the dark pulses can easily be rejected with a threshold at 3 photoelectrons for high photon flux applications, like AMS. Moreover, evidence of little sub-photoelectron pulses was found (see fig. 5.3).

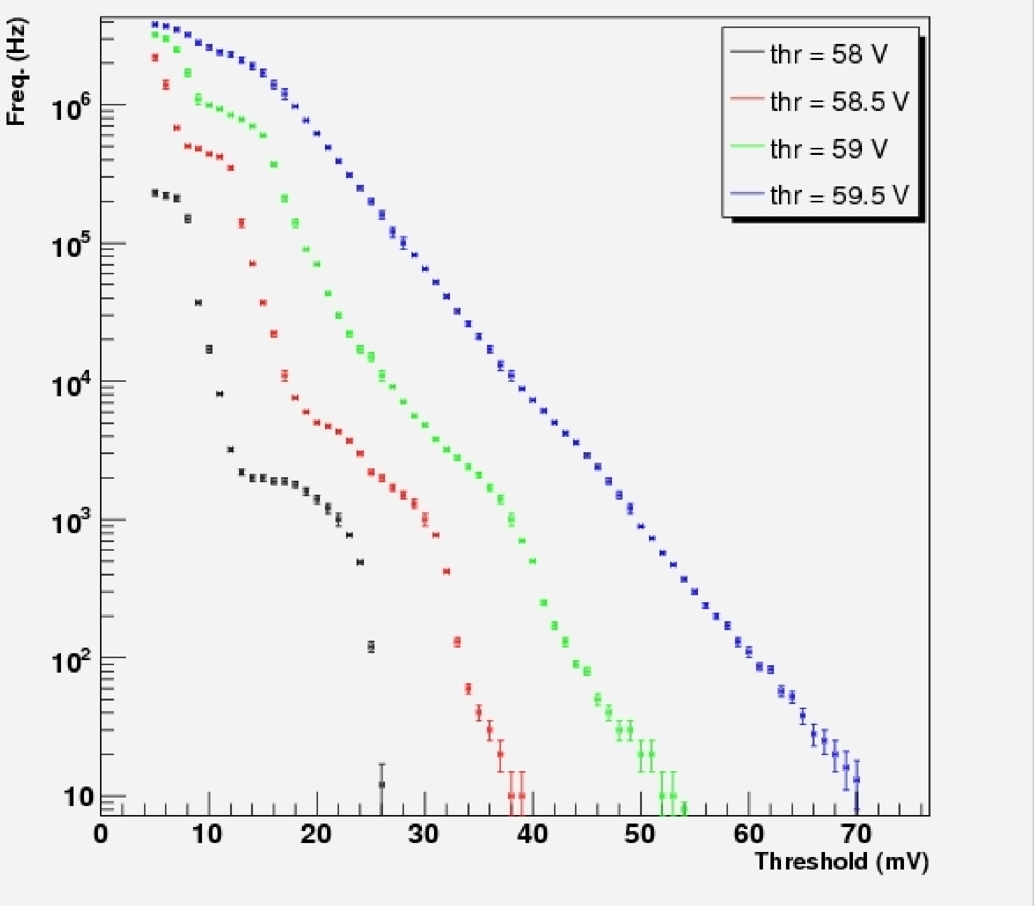

Figure 5.12: SiPM dark rate as a funtion of the threshold, for different operating voltages.

Conclusions

Following the success of the previous AMS-01 mission in 1998 and in particular of the Time Of Flight system, a new AMS-02 experiment was developed in order to improve the study of the primary cosmic rays outside the Earth atmosphere. AMS-02 is a large acceptance spectrometer with a superconducting magnet which can detect the fluxes of the cosmic rays up to 1 TeV energy. The presence of a more intense magnetic field and the longer duration of the mission (at least three years) in the extreme conditions of the International Space Station, forced the developement of a new Time Of Flight system, more complicated and delicate.

During my Laurea thesis I deepened the study of the components of the new AMS-02 Time Of Flight. Now, the conclusion of my PhD studies coincides with the completion of the new TOF detector. The spectrometer AMS-02 is scheduled to flight to the ISS with one of the last Shuttle flights in late 2009.

As responsible in Bologna of the space qualification tests of the TOF detector, I can confirm that the mechanical and electronic design, developed in three years of hard work, proved to be correct.

The main task of the detector is to provide the fast trigger and to define the acceptance for the AMS-02 spectrometer. The weight and power limitations imposed to the detector, forced to oversimplify the design. However, all tests performed on the LTOF (the UTOF has similar characteristics) proved that the apparatus is sufficiently robust to withstand the severe space environment and has enough redundant equipement to mantain full efficiency even in the unfortunate case of accidental malfunctioning of PMTs, HV power channels or cable connections.

In the last years a new solid-state photodetector (silicon photomultiplier) was developed. This device has interesting characteristics and could be a possible substitute for the usual photomultipliers, especially in future space experiments. For this reason I have started to study the performaces of the silicon photomultipliers. I present some preliminary results of this study and a MonteCarlo simulation developed to understand the aspects of the behaviour of this interesting new device.

Appendix A

The SiPM simulation code

sipmsim.cpp is the C++ code for the MonteCarlo simulation of the Silicon Photomultiplier response to light. This code make use of the Cern ROOT classes and need to read the SiPM parameters from a text file.

```
#include <TApplication.h>
#include <TGClient.h>
#include <TCanvas.h>
#include <TFile.h>
#include <TTree.h>
#include <TH1F.h>
#include <TGraphErrors.h>
#include <TF1.h>
#include <TRandom3.h>
#include <TGButton.h>
#include <TRootEmbeddedCanvas.h>
#include <TStyle.h>
#include <time.h>
#include "sipm.h"

SiPMMainFrame::SiPMMainFrame(const TGWindow *p,UInt_t w,UInt_t h) {}
SiPMMainFrame::~SiPMMainFrame() {}

 // SiPM (Assuming a square SiPM active area)
const int row_pixels = 25; // SiPM row pixels
```

```
const int col_pixels = 25; // SiPM col pixels
const int tot_pixels = row_pixels*col_pixels;
const int maxpixct=3; // maximum pixel crosstalk

// Pixel structure
struct Pixel {
  Int_t content; // Pixel status (0 = not hit; 1 = hit)
  Float_t mean;  // Pixel gaussian mean
  Float_t sigma; // pixel gaussian sigma (controllare sigma/rms)
};

Pixel sipm[row_pixels][col_pixels]; // SiPM array (as many pixels)
Int_t pixel_fired; // counter of pixels fired
Int_t nsignal,npede; // number of events for signal and for pedestal
Int_t row,col; // SiPM row,col
Float_t rnd0,rnd1,rnd2; // random varaibles
Float_t mm=0,ss=0; // temporary mean and sigma values

// ------------------  crosstalk function  ---------------------------------
void crosstalk(Float_t k, Float_t kmax, Float_t *p) {
  Double_t ct=0;
  Double_t disp;

  for (Int_t j=1; j<=maxpixct; j++) {
    for (Int_t i=j;i<=maxpixct;i++) {
      disp=TMath::Factorial(i)/(TMath::Factorial(i-j)*TMath::Factorial(j));
      ct += disp*(p[i-1]*(1-(k-1)/(kmax-1))*pow(((k-1)/(kmax-1)),i-j));
    }
    rnd2=float(gRandom->Rndm());  // cross-talk probability
    if (rnd2<ct) {
Int_t row1 = int(gRandom->Rndm()*3)-1;
Int_t col1 = int(gRandom->Rndm()*3)-1;
row1 += row;
col1 += col;
if ((row1>-1)&&(row1<row_pixels)&&(col1>-1)&&(col1<col_pixels)) {
  if (sipm[row1][col1].content==0) {
    sipm[row1][col1].content=1;
```

```
    mm+=sipm[row1][col1].mean;
    ss+=sipm[row1][col1].sigma;
    pixel_fired++;
    nsignal++;
  }
}
    }
    ct = 0;
  }
}

// ----------------------- SIPM simulation program ------------------------------
void sipmsim() {
  gStyle->SetOptStat(10);
  gStyle->SetOptFit(111);
  gStyle->SetLabelSize(0.02,"x");
  gStyle->SetLabelSize(0.02,"y");

  gRandom = new TRandom3(0); // time depending seed
  time_t t_start,t_end;

  t_start = time (NULL);

  // EXTERNAL VARIABLES
  const int n=1; // number of points
  const Float_t light=1; // light intensity
  Int_t events=50000; // number of events
  Float_t scale=1; // ADC scale factore (LowRes -> 7.57 ; HighRes -> 1)

  // ------------------------  SiPM PARAMETERS  --------------------------------
  Float_t eff=0.2; // SiPM efficiency to the light
  Float_t dc_prob=0.2;  // SiPM dark current probability
  Float_t sphep=0.15; // SiPM percentage of sub photoelectron pixels
  Float_t subgain=0.5; // subphotoelectron gain
  Float_t pede;  // pedestal
  Float_t m0,s0; // pedestal mean and sigma
  Float_t m,s;  // phe mean and sigma
```

```
Float_t p[maxpixct] = {0.18, 0.05, 0.01};  // Crosstalk probability

Float_t q; //Sipm charge
Int_t ph; // Photons generated
Int_t pfmean; // Mean of pixels fired
Int_t pfsigma; // Sigma of pixels fired

Float_t peak[n];
Float_t epeak[n];
Float_t sigma2[n];
Float_t esigma2[n];
Float_t gain[10];
Float_t peak0[10];
Float_t peak1[10];
Float_t sigma0[10];
Float_t sigma1[10];
Float_t vbias[10];

Int_t evt=0;
Float_t np[tot_pixels];
Float_t poismean; // Poisson mean
Int_t nph;        // number of photons

Int_t min,max,nbins;
Int_t idata=0,resp;
Double_t pars[2];
Double_t parg[3];
char *c = new char[1];
char temp[50];
char sipmname[2];

// -------------     read external SiPM parameters  -------------------------
printf ("Insert the SiPM name: ");
scanf ("%s",sipmname);

FILE *sipmpar = fopen(strcat(sipmname,"_par.txt"),"r"); // contains SiPM parame
```

```
  // reading SiPM parameters from external file
  while ( fgets(temp, sizeof(temp), sipmpar) !=NULL ) {
    sscanf (temp, "%f %f %f %f %f %f",&vbias[idata],&peak0[idata],&sigma0[idata],
    &peak1[idata],&sigma1[idata],&gain[idata]);
    printf ("%d - Vbias = %f V\n",idata,vbias[idata]);
    idata++;
  }

  // SiPM Vbias request
  printf ("Insert the SiPM Vbias: ");
  scanf ("%d",&resp);

  pede = peak0[resp]/scale;
  m0 = 0;
  s0 = sigma0[resp]/scale;
  m = gain[resp]/scale;
  s = sigma1[resp]/scale;

  printf ("\n********* SiPM PARAMETERS ***********\n");
  printf ("Vbias = %f V\n",vbias[resp]);
  printf ("PEDE = %f Adc ch\n",pede);
  printf ("SIGMA_PEDE = %f ADC ch\n",s0);
  printf ("GAIN = %f ADC ch\n",m);
  printf ("SIGMA PEAK 1 = %f ADC ch\n",s);
  printf ("SUB PHOTOELECTRON PIXELS = %d\%\n\n",sphep*100);

  // -------------------  SiPM array initializattion --------------------------
  for (int i=0; i<row_pixels; i++) {
    for (int j=0; j<col_pixels; j++) {
      sipm[i][j].content=0;
      if (gRandom->Rndm()<sphep) {
sipm[i][j].mean=(gRandom->Gaus(m,s))*subgain; // sub photoelectron pixel gain
      }
      else {
sipm[i][j].mean=gRandom->Gaus(m,s);   // photoelectron pixel gain
      }
      sipm[i][j].sigma=0.01; // photoelectron pixel sigma
```

```
  }
}


printf ("********** EXTERNAL PARAMETERS ***********\n");
printf ("NUMBER OF POINTS = %d \n",n);
printf ("LIGHT = %f \n",light);
printf ("EVENTS = %d \n",events);
printf ("SCALE FACTOR = %f \n",scale);
printf ("CROSS TALK PROB: p1=%f, p2=%f, p3=%f \n\n",p[0],p[1],p[2]);

for (int k=0; k<tot_pixels; k++) {
  pixels[k]=0;
  pixeff[k]=0;
}

// Histogram range
min=0;
if (light > 2) {
  max=int(light*5000*n/scale);
  nbins=int(light*100*n/scale);
}
else {
  max=1000;  // sphe limit
  nbins=1000; // sphe binning
}

TCanvas *c1 = new TCanvas("c1","c1",700,700);

// --------------------   LOOP on number of points  --------------------------
for (int l=0;l<n;l++){
  TH1F *h = new TH1F("h","",nbins,min,max);
  poismean=(l+1)*light;     // Possonian mean for the photons distribution
  pixel_fired=0;
  q=0;
  nsignal=0;
```

```
    // LOOP on events
    for (evt=0;evt<events;evt++) {
      // ------------  NUMBER OF PHOTONS (Poissonian law: ph>1)  ----------------
      if (light==0) {
ph=0;}
      else {
ph = 1+int(gRandom->Poisson(poismean));
      }
      // ------------  DARK COUNTS  ---------------------------------------------
      rnd0 = gRandom->Rndm();
      if ( rnd0 < dc_prob) {
Int_t rowdc=gRandom->Rndm()*row_pixels;
Int_t coldc=gRandom->Rndm()*col_pixels;
if ((rowdc>-1)&&(rowdc<row_pixels)&&(coldc>-1)&&(coldc<col_pixels)) {
  pixels[rowdc+row_pixels*coldc]++;
  if (sipm[rowdc][coldc].content==0) {
    sipm[rowdc][coldc].content=1;
    mm+=sipm[rowdc][coldc].mean;
    ss+=sipm[rowdc][coldc].sigma;
    pixel_fired++;
    nsignal++;
    pixeff[rowdc+row_pixels*coldc]++;
  }
}
      }

      // -------------------  LOOP on photons  ----------------------------------
      for (nph=1; nph<=ph; nph++) {
// SiPM efficiency condition
rnd1 = gRandom->Rndm();
if (rnd1 < eff) {
  // PIXEL FIRED
  row=gRandom->Rndm()*row_pixels;
  col=gRandom->Rndm()*col_pixels;
  if ((row>-1)&&(row<row_pixels)&&(col>-1)&&(col<col_pixels)) {
    pixels[row+row_pixels*col]++;
    if (sipm[row][col].content==0) {
```

```
      sipm[row][col].content=1;
      mm += sipm[row][col].mean;
      ss += sipm[row][col].sigma;
      pixel_fired++;
      nsignal++;
      pixeff[row+row_pixels*col]++;
      crosstalk(pixel_fired,tot_pixels,p);     // 2th pixel crosstalk
    }
  }
}  // end efficiency loop
      } // end photon loop (event = i)

      // ----------------------  SiPM CHARGE  ---------------------------------------
      if (mm>0) q = pede+gRandom->Gaus(mm,ss);
      for (int i=0; i<tot_pixels; i++) {
np[i]=i;
      }

      // -----------------------  PEDESTAL  -----------------------------------------
      if (q==0) {
q = pede+gRandom->Gaus(m0,s0);
npede++;
      }

      h->Fill(q);

      if ((evt!=0)&&(fmod(evt,events/5)==0)){
printf("n=%d/%d  ev=%d/%d\n",l+1,n,evt,events);
      }

      // -----------------  SiPM REINITIALIZATION  --------------------------
      mm=0;
      ss=0;
      q=0;
      pixel_fired=0;

      for (int i=0; i<row_pixels; i++) {
```

```
for (int j=0; j<col_pixels; j++) {
  sipm[i][j].content=0;
  if (gRandom->Rndm()<sphep) {
    sipm[i][j].mean=(gRandom->Gaus(m,s))*subgain; // sub photoelectron pixel gain
  }
  else {
    sipm[i][j].mean=gRandom->Gaus(m,s);   // photoelectron pixel gain
  }
  sipm[i][j].sigma=0.01; // photoelectron pixel sigma
}
      }
      for (int i=0; i<tot_pixels; i++) {
pixels[i]=0;
pixeff[i]=0;
      }

    } // end events loop


    // -------------------  OUTPUT PLOTS  ---------------------------------------
    printf ("Mean=%f\n",h->GetMean());
    printf ("Sigma=%f\n",h->GetRMS());

    h->Draw();

    h->SetTitle("SiPM spectrum");
    h->GetYaxis()->SetTitle("Events");
    h->GetXaxis()->SetTitle("ADC ch");

    if (light > 5) {
      int ming = h->GetMean()-10*(h->GetRMS());
      int maxg = h->GetMean()+10*(h->GetRMS());

      TF1 *fitg = new TF1("fitg","gaus",ming,maxg);
      h->Fit("fitg","R");

      peak[l]=fitg->GetParameter(1);
```

```
      epeak[l]=fitg->GetParError(1);
      sigma2[l] = fitg->GetParameter(2);
      esigma2[l] = fitg->GetParError(2);
      printf("Mean[%d] = %f +/- %f \n",l,peak[l],epeak[l]);
      printf("Sigma[%d] = %f +/- %f \n",l,sigma2[l],esigma2[l]);
      esigma2[l] = 2*esigma2[l]*sigma2[l];
      sigma2[l] *= sigma2[l];
    }
    c1->Update();

  }  // end N points loop

  if (n>3) {

    TCanvas *c2 = new TCanvas("c2","c2",750,750);
    c2->SetGrid();

    TGraphErrors *gr = new TGraphErrors(n,peak,sigma2,epeak,esigma2); // Plot of
    gr->Draw("AP");
    gr->SetTitle("SiPM #sigma^{2} vs peak - MC SIMUL");
    gr->GetXaxis()->SetTitle("Peak (ADC ch)");
    gr->GetYaxis()->SetTitle("#sigma^{2} (ADC ch)^{2}");

    TF1 *fitl =new TF1 ("fitl","pol1",min,max);
    gr->Fit("fitl","R");  // linear fit

    c2->Update();
  }

  t_end = time (NULL);

  printf("Esecution time = %d s\n",t_end-t_start);
}

// ------------------------ main program ----------------------------------------

int main (int argc, char **argv) {
```

```
  TApplication theApp("App",&argc,argv);
  sipmsim();
  theApp.Run();
  return 0;
}
```

Bibliography

[1] A.D. Dolgov, *Non-GUT baryogenesis*. Physics Reports 222 (1992) 309

[2] G. Jungman et al., *Supersymmetric dark matter*. Physics Reports 267 (1996) 195

[3] T. Moroi and L. Randall, *Wino cold dark matter from anomaly mediated SUSY breaking*. Nuclear Physics B570 (2000) 455

[4] M. Aguilar et al., *The Alpha Magnetic Spectrometer (AMS) on the International Space Station: Part I - results from the test flight on the space shuttle*. Physics Reports 366 (2002) 331

[5] B. Blau et al, *The superconducting magnet of AMS-02* Nuclear Physics B - Proc. Suppl. Volume 113 (2002) 125-132

[6] A. Nakano, D. Petrac, C. Paine, *He II liquid/vapour phase separator for large dynamic range operation*. Cryogenics 36 (10) (1996) 823

[7] D. Casadei et al., *The AMS-02 Time of Flight System. Final Design*. Proceedings of the 28^{th} International Cosmic Ray Conference (2003) 2169

[8] V. Bindi et al., *Performance of AMS-02 Time of Flight*. Proceedings of the 29^{th} International Cosmic Ray Conference Pune (2005) 9,41

[9] S. Fopp et al., *The Anticoincidence Counter System of the AMS-02 Experiment. A status Report*. AMS Internal Note, 2002

[10] C. Lechanoine-Leluc, *The AMS-02 Tracker*. Proceedings of the 29^{th} International Cosmic Ray Conference Pune (2005) 9,299

[11] P. Zuccon, *The AMS Tracker Performance*. Proceedings of the 29^{th} International Cosmic Ray Conference Pune (2005) 9,291

[12] Kirn et Siedenburg, *The AMS-02 transition radiation detector*. NIM A535 (2004) 165

[13] M. Aguilar Benitez et al., *The Ring Imaging Cherenkov detector (RICH) of the AMS experiment*. Proceedings of the 29^{th} International Cosmic Ray Conference Pune (2005) 3,349

[14] P. Aguayo et al., *Prototype study of the Cherenkov imager of the AMS experiment*. Nuclear Instruments and Methods in Physics Research A 560 (2006) 291

[15] F. Cervelli et al., *A reduced scale e.m. calorimeter prototype for the AMS-02 experiment*. Nuclear Instruments and Methods in Physics Research A 490 (2002) 132

[16] F. Cadoux et al., *The AMS-02 electromagnetic calorimeter*. Nuclear Physics B (Proceedings Supplements) 113 (2002) 159

[17] E. Iarocci, *Plastic Streamer Tubes and their Applications in High Energy Physics*. NIM A217, 30-42.

[18] L. Quadrani et al., *Optimization of Time Of Flight of the AMS-02 experiment*. Proceedings of the 29^{th} International Cosmic Ray Conference Pune (2005) 9,45

[19] N. Carota, *Studi per la calibrazione e l'ottimizzazione dei fotomoltiplicatori per i contatori a scintillazione dello spettrometro spaziale AMS-02*. AMS Bologna Laurea thesis (13/12/2002).

[20] T. Baeck, *Evolutionary Algorithms in Theory and Practice*. Oxford University Press (1996)

[21] J. Clarke et al., *The Application of Metaheuristic Search Techniques to Problems in Software Engineering*. SEMINAL-TR-01-2000: August 30, 2000.

[22] S. Kirkpatrick et al., *Optimization by Simulated Annealing*. Science (1983) Vol 220, Number 4598, pages 671-680.

[23] L. Quadrani, *Studio del comportamento nello spazio dei fotomoltiplicatori "fine mesh" dello spettrometro AMS-02*. AMS Bologna Laurea thesis (13/03/2003).

[24] B. Bencheikh et al., *A simple light detector gain measurement technique*. NIM A315 (1992) 349.

[25] L. Brocco et al., *Behavior in strong magnetic field of the photomultipliers for the TOF system of the AMS-02 space experiment*. Proc. of the 27th ICRC (2001)

[26] G. Levi et al., *The mesh PM for the AMS Time Of Flight, comparison between simulation and measurements*. NIM A530/3 (2004) 419.

[27] V. Bindi, *Development and performances of the SFEC card for the TOF apparatus*. AMS Bologna PhD thesis (15/03/2006).

[28] C. Guandalini, G. Laurenti, *L-TOF Vibration Test Report*. INFN Report, Dic 2006

[29] G. Levi et al., *Results of vibration test for PMs on telescope*. AMS Bologna Internal Notes Dec. 20,2002.

[30] C.Sbarra et al., *Preliminary study of silicon photomultipliers for space missions*. NIM A572 (2007) 662-667.

[31] B. Dolgoshein et al., *An Advanced Study of Silicon Potomultiplier*. ICFA Instrumentation Bulletin, 2000.

[32] B. Dolgoshein et al., *Silicon photomultiplier and its possible applications*. NIMA 504 (2003) 48-52

[33] V. Golovin, V. Savaliev, *Novel type of avalanche photodetector with Geiger mode operation*. NIMA 518 (2004) 560-564

[34] A.G. Chynoweth, K.G. McKay, *Photon Emission from Avalanche Breakdown in Silicon*. Phys. Rev. 102, 369 - 376 (1956)

[35] J. Barral *Study of Silicon Photomultipliers*. Promotion X2001, Ecole Polytechnique, France

[36] R. Martelli, *Studio e simulazione delle caratteristiche dei fotomoltiplicatori Fine Mesh per l esperimento AMS-02*. AMS Laurea thesis (18/10/2002)

[37] G. Vincent et al., J. Appl. Phys. 50 (1979) 5984